Investigations of the effective dose rate from UF_6-cylinders by Monte-Carlo simulations in respect of radiation protection

by Andreas Meyering

Master thesis

presented to the

Department of Physics

University of Münster

Münster

March 2012

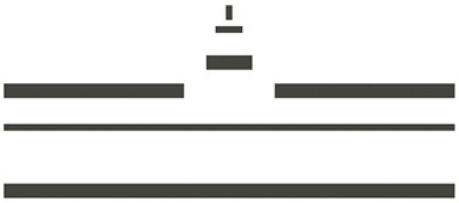

Thesis advisor:
Prof. Dr. Alfons Khoukaz
Second Thesis advisor:
Prof. Dr. Dieter Frekers

Contents

Chapter 1

Introduction

Radioactive radiation can not even taste, smell, hear, see and feel and is thus not noticeable with the human senses. Only by a fortunate contingency, the radioactivity was discovered by the french physicist Antoine Henri Becquerel in 1896, who tried to explain the nigrification of photoplates through uranium salts by fluorescence. Since the photoplates were also blackend without prior irradiation of the uranium salt, he has assigned the observed radiation to the uranium salt itself. From this time, the study of radioactive elements began and thus the discovery of the benefits of radioactive elements for energy generation, nuclear medicine etc. and coinstantaneous the dangers which can be caused by radioactive radiation. Ionizing radiation which is produced by a radioactive decay, can be divided into three types of radiation (α, β- and γ-radiation), where each of these three different types of radiation have harmful biological effects on the human body and which may lead to serious affections. In order to minimize consequential damage to human health and the environment by radioactive elements, various regulations and laws were set up such as the Atomic Energy Law and the Radiation Protection Ordinance.
Nuclear facilities, as the uranium enrichment facility Urenco Germany GmbH is, must adhere the Atomic Energy Law and the Radiation Protection Ordinance and are therefore obliged to minimize exposure radiation of the employees and the surrounding human population. In order to comply these regulations and licensing requirements, periodic measurements of the dose rate must be performed and the exact radiation exposure, wich come from the production medium uranium hexafluoride (UF_6), must be known. With the aid of computer-based Monte-Carlo simulations, the required dose rate of UF_6 cylinders, in which the UF_6 is stored, can be calculated from UF_6 cylinders and complex cylinder storages. Thus, the dose rate can be calculated at

any distance each time and a measure of the total dose can be estimated on the employee, provided the retention time and distance to the respective cylinder or storage is known. This has relevant advantages for radiation protection and radiation safety of employees and the human population.

The aim of this master thesis is, to calculate the effective dose rate of UF_6 cylinders at various distances with the aid of the computer-based simulation program Monte Carlo N-Particle (MCNP) in respect of radiation protection and radiation safety to estimate the dose of employees and human population as good as possible.
Chapter 2 explains worth knowing information about URENCO Germany GmbH itself and the production prozess with the medium uranium hexafluoride (UF_6) and the typical physical nature of UF_6.
In chapter 3 the theoretical basics are explained for dosimetry and the development of the different kinds of radiation which are important for this work. Adjacent, a brief introduction in the issue of radioactive equilibrium is given.
The different radiation components which are produced by physical processes in a UF_6 cylinder are very important for this work and are described in chapter 4.
Chapter 5 is the main part of this work, where the MCNP investigations of the different types of UF_6 cylinders are and the theoretical calculation of the ambient dose rate of a Product-store at different reveiving points. Prior to this, the theoretical MCNP-calculations are verified by real measurements at a 48Y-Feed UF_6 cylinder and a brief introduction of the simulation program MCNP is given.
Finally, the results are abstracted and a outlook is given in chapter 6 in english and chapter 7 in german.

Chapter 2

Worth knowing

2.1 History of URENCO Deutschland GmbH

URENCO Deutschland GmbH is a uranium enrichment facility that belongs to the URENCO-Group and produces enriched uranium for the fuel supply for nuclear power plants. Companies from the UK and the Netherlands also belongs to the Urenco-Group. The Urenco centrifuge are developed and qualified at the Development Centre Jülich. It is extremely important to develop centrifuges to increase safety and improve efficiency.
The first units to enrich uranium were taken into operation in August 1985. Since then, the facility was continuous expanded and had an enrichment capacity of 1800 t SWU/a (SWU/a: Separative Work Unit per year) in August 2005. In 1981, it was already known that the location Gronau is projected for a capacity of 5000 t SWU/a. Today (2012), the uranium enrichment facility Gronau (UAG) has a enrichment capacity of 4250 t SWU/a [1].

2.2 Separation Work Unit "SWU"

To operate a light water reactor a percentage of up to 5% U-235 is required (depending on the type of reactor) to initiate and maintain a chain reaction. But in natural uranium only a fraction of about 0.711% U-235 is available, so that the natural uranium must be enriched with special proceedings like centrifuge or diffusion processes. An alternative method to enrich natural uranium is the laser process, but this method never got beyond the basic research. The UAG uses the centrifuge process to enrich the natural uranium, so that the other processes will not go furthermore

into detail.

A separation element like a centrifuge, seperates the incoming UF_6-flux (*Feed*) into two streams. First the depleted uranium (*Tails*) and second the enriched uranium (*Product*). The depleted and enriched uranium is still in a hexafluorine enviroment. A scheme of a seperation element and the streams of Feed, Product and Tails are shown in figure 2.1.

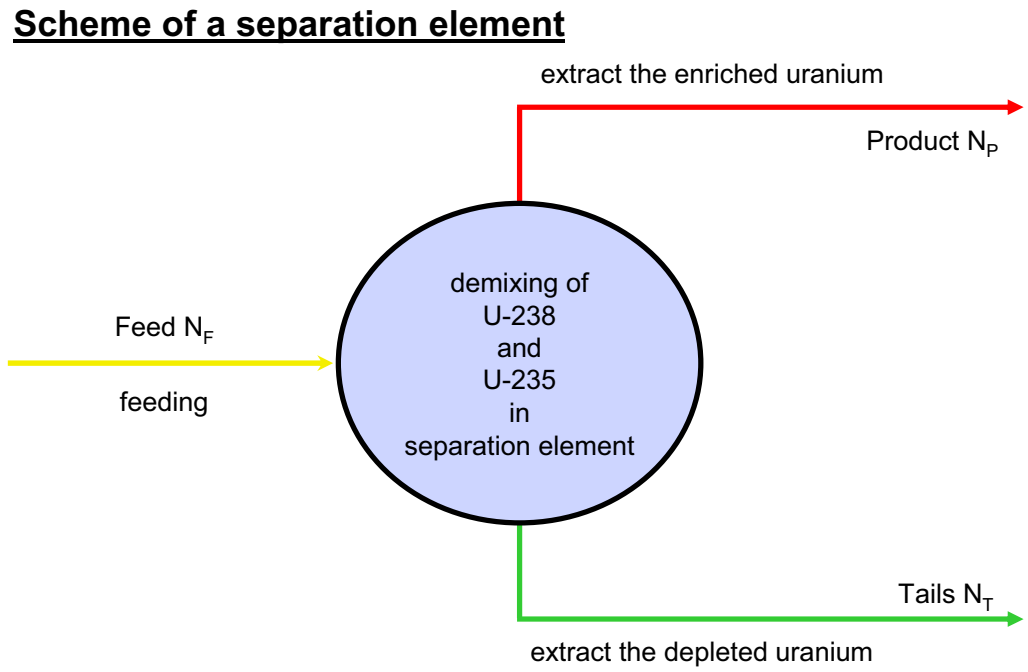

Figure 2.1: Scheme of a separation element with the streams of Feed, Product and Tails (adapted from [2]).

The concentration of Feed, Product and Tails refer to the percentage of U-235 of the uranium isotope mixing. For example, 0.32% depleted UF_6 is called Tails and owns 0.32% U-235 of the whole uranium contributions. In contrast, 5% enriched UF_6 is called Product and has a concentration of 5% U-235.

To determine the size of the concentration shift of U-235 in a separation element, three factors are essential. Once the *depletion factor* β, then the *enrichment factor* α and finally the total separation factor $\alpha \cdot \beta$ which is the product of the enrichment factor and the depletion factor. These are defined as follows [2]:

$$\alpha = \frac{N_P(1-N_F)}{N_F(1-N_P)} \tag{2.1}$$

$$\beta = \frac{N_F(1-N_T)}{N_T(1-N_F)} \tag{2.2}$$

$$\alpha \cdot \beta = \frac{N_P(1-N_T)}{N_T(1-N_P)} \tag{2.3}$$

$$\tag{2.4}$$

in which N_i with i=F,P,T (F=Feed, P=Product, T=Tails) are the U-235 concentrations of the Feed, Product and Tails. The factors can be described as a ratio of concentrations which describes the enrichment or depletion of U-235. However, it can not be determined the effort of a separation element.
To describe the required effort of a separation element which commute the Feed into the desired product and byproduct tails, the concept of "separation work" (often called: seperation work unit, short "SWU") has been inserted. The separation work is not a physically measurable quantity, so that a proportionality between the Product and the Feed must be set, by using the concentrations N_F, N_P and N_T as the proportionality constant. The Ansatz for this proportionality delivers the mass and isotope balances of a separation element.

$$0 = m_P + m_T - m_F \qquad \text{(mass balance)} \tag{2.5}$$

$$0 = m_P \cdot N_P + m_T \cdot N_T - m_F \cdot N_F \qquad \text{(isotope balance)} \tag{2.6}$$

in which m_i with i=F,P,T is the amount of Feed, Product and Tails. By solving these equations to m_F, it gives the separation work to produce a given amount of Feed to a certain amount of Product (equation 2.7) [2].

$$m_F = \left(\frac{N_P - N_T}{N_F - N_T}\right) m_P \tag{2.7}$$

The unit of the separartion work is kg. The separation performance of a separation element can now be determined by multiplying a value function $V(N_i)$ (with i= F,P,T) to the amount of Feed, Product and Tails and depends only on the respective concentrations (see equation 2.8) [2].

$$\delta U = m_P \cdot V(N_P) + m_T \cdot V(N_T) - m_F \cdot V(N_F) \tag{2.8}$$

The value function is mathematically so chosen, that it is time-independent. It is a second order differential equation and has after integration twice time and chosen

the two free selectable integration constants, the following shape (equation 2.9) [2]. The unit of the value function is dimensionless.

$$V(N_i) = (2N_i - 1)\, ln\left(\frac{N_i}{1 - N_i}\right) \tag{2.9}$$

Using these relationships, it can be now determined the uranium concentration after the passage of a separation element. By series- and parallel-connection of several separation elements (cascadw), the U-235 concentration can be enriched in the Product, or depleted in the Tails. The final streams after sufficiently depleting or enriching are bottled into UF_6 cylinders and are primarily stored at the Urenco storage facilities before they will be deliver to the nuclear power plants. The effective dose rate of the cylinders is measured and calculated later to ensure the safety of workers at the Urenco terrain and the people in the surrounding environment. For these calculations it is especially important to know the exact concentration of U-238, U-235, U-234 and U-232 which are present in the cylinders. Only by this a relatively accurate reflection of the radioactive radiation can occur.

2.3 The medium uranium hexafluoride UF_6

Urenco uses uranium hexafluoride UF_6 as process medium which is fed as a gas into the centrifuges. UF_6 is produced in conversion facilities, where the source material (uranates) is converted to UF_6 by chemical reactions. The use of UF_6 is particularly suitable for industrial processing because it has good physical material properties at room temperature and at atmospheric pressure, as it is clearly seen from the phase diagram of UF_6 (figure 2.2).

At room temperature and at atmospheric pressure, UF_6 is as a white crystalline solid available. Lowering the vapour pressure to about 100 mbar, but still at room temperature, UF_6 directly goes into the gaseous state; it sublimates. This high vapour pressure is important for the feeding of UF_6 from the cylinders into the centrifuges because this can only occur in the gaseous state of UF_6. The sublimation point at atmospheric pressure is 56°C. The triple point is at a temperature of 64°C and an associated vapour pressure of 1516 mbar. Finally, the critical point and the end of the phase diagram is at a temperature of 230°C and a pressure of 45.6 bar [2]. These physical criteria show the technical benefits of UF_6. It can be stored at atmospheric pressure and room temperature because it is present in the solid state and by heating the UF_6 or lowering the vapor pressure, it can quickly goes into the gaseous state.

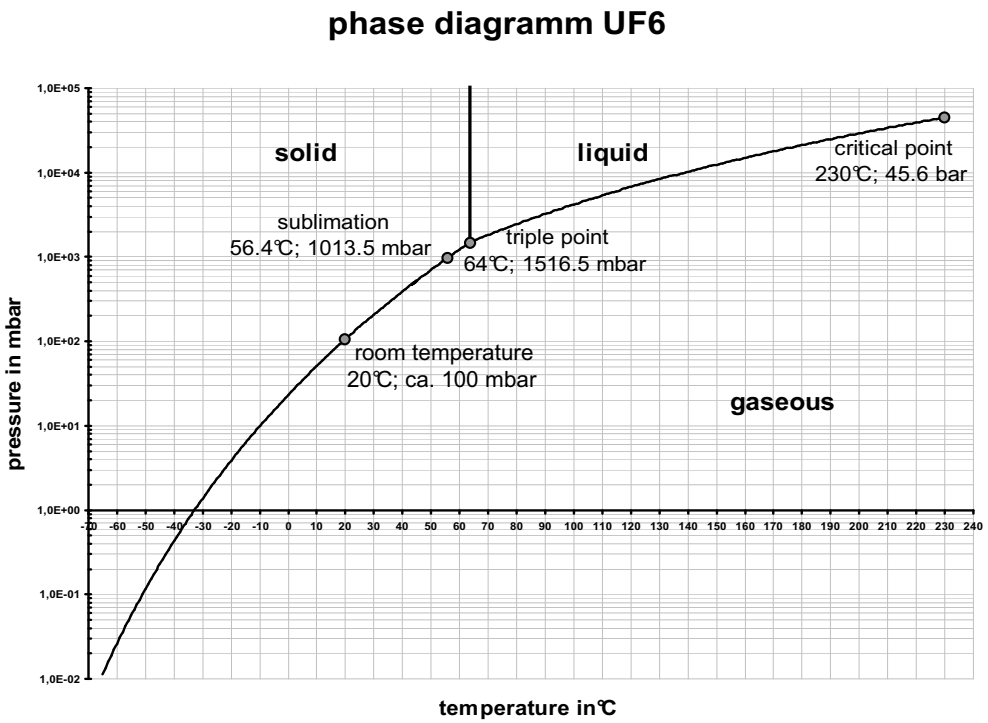

Figure 2.2: Phase diagramm of UF_6. The pressure in *mbar* is plotted against the temperature in K. Also the most important points like triple point, critical point, sublimation point and the point at room temperature are illustrated in the phase diagram [2].

UF_6 has in solid state and at room temperature a density of $5.1\frac{g}{cm^3}$. In the liquid state of UF_6 the density erratic drops to about $3.7\frac{g}{cm^3}$ (see figure 2.3) which increase simultaneous the volume of the UF_6. Therefore, the UF_6cylinders are filled only up to two thirds to avoid external mechanical stresses on the cylinders. This property must be considered in the geometry of MCNP-calculations later.

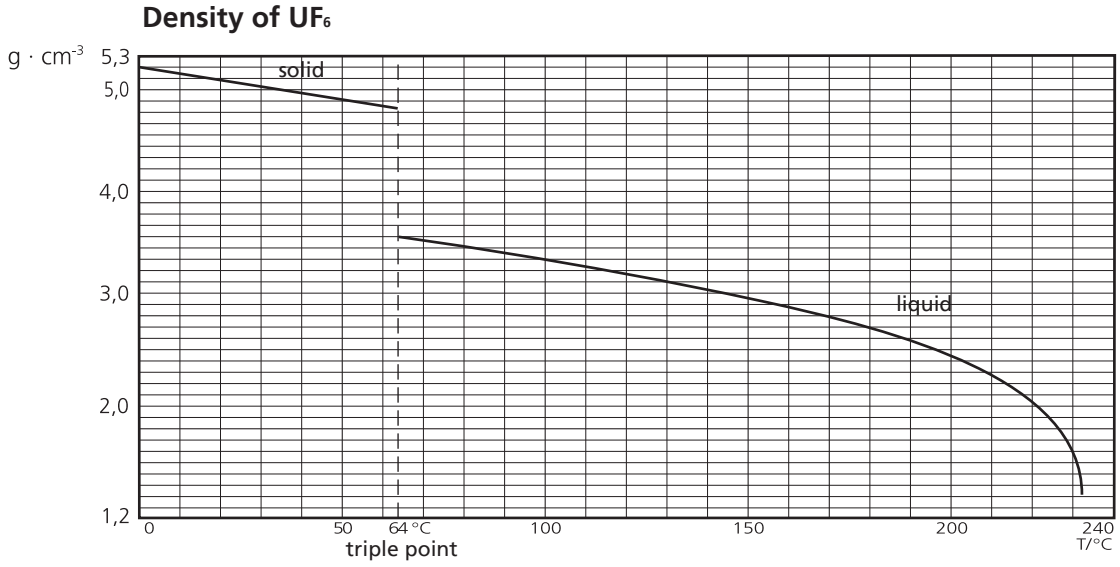

Figure 2.3: Density-temperature diagram of UF_6. The density of UF_6 erratic drops at a temperature of 64° C and a pressure of 1516 mbar from ca. 5 $\frac{g}{cm^3}$ in the solid state to ca. 3.5 $\frac{g}{cm^3}$ in the liquid state [2].

2.4 Types of UF_6-cylinders

In this section two types of UF_6 cylinders are presented, which are used for the storage and transportation of UF_6 according to *American National Standards* (ANSI) for nuclear materials. The first is the *48Y* cylinder type and the second the *30B* cylinder type. Furthermore, the geometries of these cylinders will be used in later MCNP-calculations. To represent satisfactory results, it is important to know the geometry of the UF_6 cylinders, even if they are slightly simplified in the calculations due to the complexity of the UF_6 cylinder types.

2.4.1 48Y cylinder

The 48Y cylinder is used for storage of natural uranium (Feed) and transportation and to store enriched uranium (Product), in order to fill them later on different 30B cylinders. In addition to this, the 48Y cylinder stores depleted uranium (Tails). According to ANSI specifications, the wall of the 48Y cylinder exist of steel and has a thickness of exactly 1.5875 cm. A technical drawing of the 48Y cylinder is shown in figure 2.4.

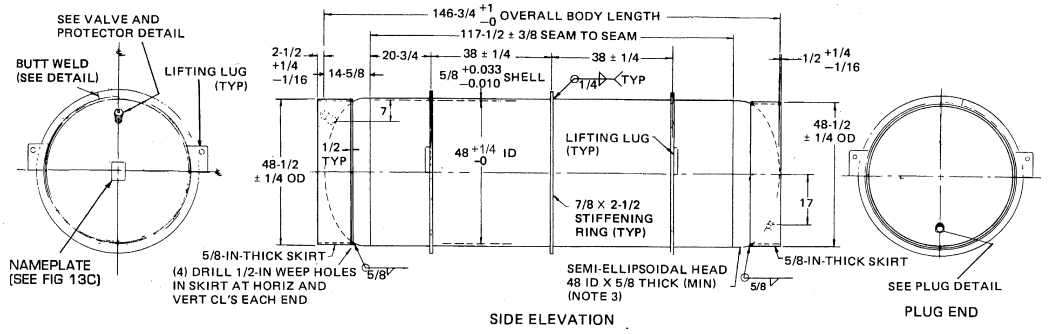

Figure 2.4: Technical drawing of a 48Y cylinder from side and end. All measure of length and errors of these are given in inches [3].

2.4.2 30B cylinder

In contrast to the 48Y cylinder, the 30B cylinder has significantly smaller dimensions and the thickness of the cylinder wall is with 1.27 cm also lower than the wall of the 48Y cylinder. The 30B-cylinder is only used for delivery of enriched uranium to nuclear power plants. Just as the 48Y-cylinder, the 30B cylinder is in compliance with the ANSI specifications. The technical drawing of the real 30B cylinder is shown in figure 2.5.

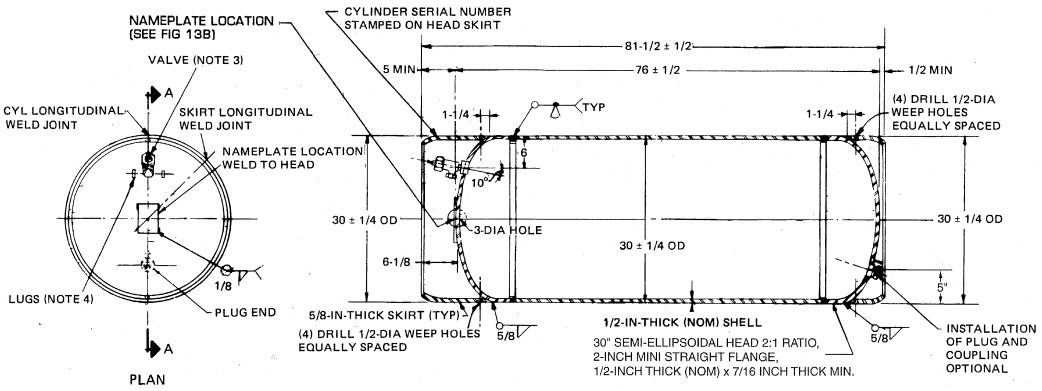

Figure 2.5: Technical drawing of a 30B cylinder from side and end. All measure of length and errors of these are given in inches [3].

Chapter 3

Theoretical basics

3.1 Dosimetry

Dosimetry is generally understood as the measurement of ionizing radiation and determination of the effective dose rate of a person or an object in the division of radiation protection. In personal dosimetrie it is differed between external and internal radiation exposure. By external exposure it bargain of external radiation effects and by internal radiation exposure by uptake of radionuclides and their effect on the human body from the inside out. The determination of the dose is extremely important for a person to do not exceed certain limits from the effects of radiation and it will not result in a permanent damage to human organs. Therefore, this section is explained in detail because the effective dose rate (from external exposure) is determined in the following measurements and theoretical calculations, so that the reader should understand the terms and definitions noticed in this sections.

3.1.1 Decay law and activity

To determine the decay of a radioactive element, the *decay law* is used. This is a differential equation of first order and states that the temporal change of the number of particles is proportional to the number of the particles itself (see equation 3.1).

$$\frac{dN}{dt} = -\lambda N \tag{3.1}$$

with N as the number of particles and λ as the proportional constant, named *disintegration constant*. By integration and resolving equation 3.1 to N, the number of particles at time t is defined (see equation 3.2).

$$N(t) = N_0 \cdot e^{-\lambda \cdot t} \tag{3.2}$$

with N_0 as the integration constant which reveal the number of particles at the time $t = 0$. The number of particles also decrease exponentially with time. The *half-life* $t_{1/2}$, where the half of the radioactive nuclides N_0 are decayed from time $t = 0$ has a characteristic value for each radionuclide and can be calculated with the aid of the decay law (equation 3.3).

$$\frac{N_0}{2} = N_0 \cdot e^{-\lambda t_{1/2}} \Rightarrow t_{1/2} = \frac{ln(2)}{\lambda} \tag{3.3}$$

It is often useful to know the number of radioactive nuclides which decay in a given time instead to know the number of nuclides which are transformed. This issue is called *activity* or *decay rate* and is defined by the multiplication of the decay law with the disintegration constant (equation 3.4).

$$A(t) = N(t) \cdot \lambda = A_0 \cdot e^{-\lambda \cdot t} \tag{3.4}$$

with $A_0 = \lambda \cdot N_0$ as the activity at time $t = 0$. The activity indicates the nuclear disintegrations per unit time, so that the measurement unit is $Bq = s^{-1}$ (Becquerel). Analogous to the decay law a source has only half of the primary activity at the time of $t_{1/2}$.
It should be noted that many radionuclides form by it decays daughter nuclides which are radioactive, too. The activity refers only to the original nuclide and not to the daughter nuclide. In addition to the activity, there are other kinds of activities which differ only by an additional unit in the denominator.

- specific activity (Bq/kg)
- activity concentration (Bq/m^3, Bq/l)
- surface activity (Bq/m^2)

3.1.2 Absorbed dose rate and dose equivalent rate

For radiation protection it is particularly important to make statements about the radiation which involves damage on human body. Due to this the stored energy of ionizing radiation can be used as a measure of physical effects of radiation. The energy of ionizing radiation consists essentially of three components. First the irradiated energy W_i, then the emitted energy W_e and finally the energy which is released by conversion processes W_c. In summary a total energy W is given by:

$$W = W_i + W_c - W_e \tag{3.5}$$

The *absorbed dose* of an ionizing radiation is defined by the absorbed energy of an irradiated material per mass (see equation 3.6).

$$D = \frac{dW}{dm} \tag{3.6}$$

with the measurement unit $Gy = J/kg$ (Gray). Of course, the expression of the mass can be expressed in an expression of the volume by the relation $dm = \rho \cdot dV$ [4]. The absorbed dose is independent on the radiation because it is not considered the type of radiation, but only the energy of the incoming radiation. Due to this, it should be known for the absorbed dose which amount of energy the types of radiation exhibit.
The time derivative of the absorbed dose is the *absorbed dose rate* and provides information on the energy dose experienced by a person or material in a defined time interval (equation 3.7).

$$\dot{D} = \frac{D}{dt} \tag{3.7}$$

It has the measurement unit $Gy/s = J/kg/s$. The absorbed dose rate of a γ-point source is proportional to the activity of the radionuclide and vice versa proprtional to the square of the distance r from the radiation source. The proportionality constant is k_γ and is named *exposure rate coefficient* for γ-radiation. For a β-point source it is not so easy to calculate the absorbed dose rate because the β-radiation has a limited range in air of a few meters depending on the strength of energy. But there can be made a similar calculation except for the proportionality constant which must be replaced by a function $k_\beta(r)$ and is strongly dependent on the distance [5].
It should be noticed that the calculations in this work are done with an extended radiation source and not with a point source, so that the relation between the absorbed dose rate, distance and activity can not be used as described above.

Different types of radiation are absorbed differently by materials or human bodies. Therefore it makes sense to multiply the absorbed dose which is caused by different radiation types with a *radiation weighting factor* w_R and thus to define the *equivalent dose*. The radiation weighting factor comes from the division of radiation protection and depends on the type of radiation and the energy of the particles. It also includes the relative biological efficacy of the radiation, so that the equivalent dose is a better

size for the determination of the absorbed energy in human body than the absorbed dose. The equivalent dose is defined as follows (equation 3.8) then.

$$H = w_r \cdot D \tag{3.8}$$

The measurement unit of the equivalent dose is the same as the absorbed dose, but is named differently as $Sv = J/kg$ (Sievert) because of the occurrence of the radiation weighting factor in the equation of the equivalent dose.
If the radiation, absorbed by human body, consist of several types of radiation, the individual contributions of the radiation weighting factor and the absorbed dose will be added together to obtain the total equivalent dose.
The radiation weighting factor depends, as already mentioned, on the type of radiation and the energy of the ionizing radiation. So the radiation weighting factor has values between 1 for photons and 20 for α-radiation and neutron radiation with certain energies. Photons can be regarded as massless particles and can penetrate the matter and are atenuated. Therefore, photons have a low radiation weighting factor. Possible interactions of photons with matter are the *photoelectric effect*, *compton effect* and *pair production*. However, α-radiation interacts strongly with matter which is confirmed by its short range and simple shielding. α-cores ionize more atoms in a small area on their path through matter which can lead to permanent damage in cells and tissues at human body in a small area. The radiation weighting factor for radiation types and energy ranges is presented in table 3.1.

Type of radiation and energy field	Radiation weighting factor
Photons, electrons, myons all energies	1
Neutrons $<$ 10 keV 10 keV to 100 keV $>$ 100 keV to 2 MeV $>$ 2 MeV to 20 MeV $>$ 20 MeV	 5 10 20 10 5
Protons $>$ 2 MeV	5
α-particles	20

Table 3.1: Radiation weighting factor of the different types of radiation and their energy fields [6].

After the equivalent dose was described in detail, the *dose equivalent rate* is defined. It is the time derivation of the equivalent dose and express the equivalent dose that is absorbed within a certain time (equation 3.9).

$$\dot{H} = \frac{dH}{dt} = w_r \cdot \dot{D} \tag{3.9}$$

The measurement unit is $Sv/s = J/kg/s$.

3.1.3 Effective dose and effective dose rate

The human body consists of bone marrow, tissues and different organs. Each of these individual components have in some extent greatly different radiation sensitivities. Therefore it makes sense to weight the equivalent dose for the individual tissues and organs with their own *tissue weighting factor* w_T. The tissue weighting factor was defined by the *International Comission on Radiological Protection (ICRP)* [7]. The important tissue weighting factors are listed up in table 3.2.

Tissue or organ	Tissue weighting factor w_T
Gonads	0.20
Bone marrow (red)	0.12
Colon	0.12
Lung	0.12
Stomach	0.12
Bladder	0.05
Breast	0.05
Liver	0.05
Oesophagus	0.05
Thyroid	0.05
Skin	0.01
Bone surface	0.01
Remainder	0.05

Table 3.2: Tissue weighting factors for different tissues and organs[7].

After the equivalent dose was weighted with the tissue weighting factor, the *effective dose* E can be determined now in an organ or tissue (see equation 3.10).

$$E = w_T \cdot H \tag{3.10}$$

with the measurement unit Sv because the tissue weighting factor is dimensionless. The total effective dose in a human body is the sum over effective doses of the individual tissues and organs. The time derivation of the effective dose is the *effective dose rate* (see equation 3.11).

$$\dot{E} = \frac{dE}{dt} = w_t \cdot \dot{H} \tag{3.11}$$

with the measurement unit Sv/s. The time specification can be named in hours h or years a, too.

3.2 γ-radiation after α- and β-decay

γ-photons will be produced by nuclear physical processes, if the core of a nuclide goes from an excited state to a less excited state or in the ground state. The nuclide can emit the energy difference between two states in form of γ-photons. The energies of the γ-photons are monoenergetic because the energy difference between two states of a special nucleus is always the same. Slight differences in energy of the γ-photons and the energy difference between two states can be explained by recoil effects (Mössbauer effect [8]). These recoil effects will be neglected, if the nuclide is in a crystalline structure. The recoil is then compensated by the remaining lattice atoms.

If the nucleus of a radioiactive nuclide decays by an α- or β-decay, the daughter nuclide will not necessarily go in its ground state, but can be still in an excited state, when the whole decay energy is not delivered to the α- or β-particle. Since all cores prefer a state of lowest energy, the energy difference of the core will be resolved by emitting γ-photons with the amount of the energy difference.
A simple and very illustrative example for this process can be explained with the aid of cobalt-60 (Co-60) (see figure 3.1). Cobalt is a β^--emitter, goes with a probability of 99.88% in the first excited state of nickel-60 (Ni-60) and emits a β-particle with the energy of 0.31 MeV. With a probability of 0.12% Co-60 goes into the second excited state of Ni-60 and emits a β^--particle with the energy of 1.48 MeV. As the nickel atom is still in the excited state after both possibility decays, this excitation is emitted in form of γ-photons. When the nickel is in the second excited state, then it emits one γ-photon with an energy of 1.3325 MeV. In the first excited state it passes through the emission of a γ-photon (1.732 MeV) in the second excited state and by further emitting of a γ-photon (1.3325 MeV) it goes ultimately to the stable ground state of Ni-60.
By such a simple decay scheme the complete radiation, the associated energies and probabilities are given for the decay of a nuclide.

In addition to the above explained process a few radioactive nuclides can be arranged in a *meta-stable* state which can be calmed down by a radioactive decay or isomeric transformation. By emitting a γ-photon, the meta-stable state can go in

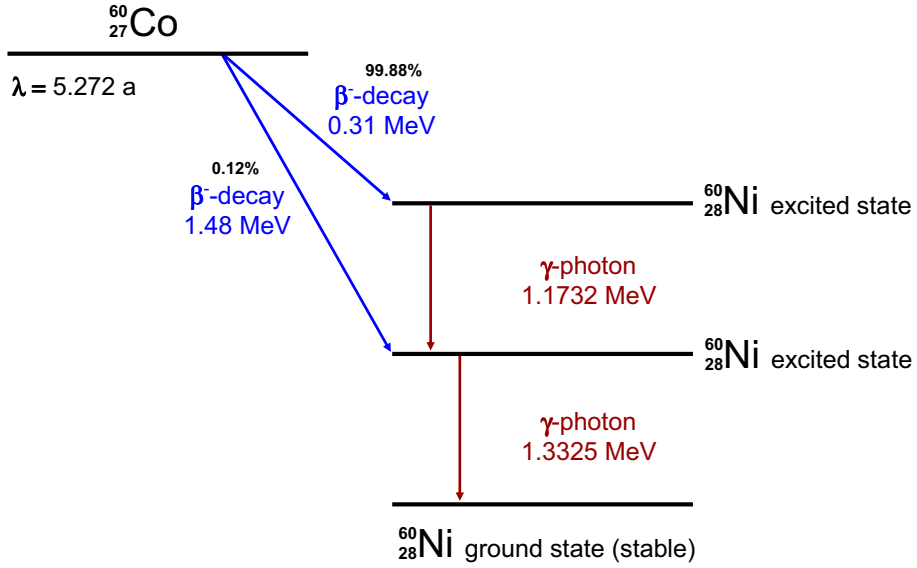

Figure 3.1: Decay scheme of Co-60. After decaying into nickel, the nickel is already not in the stable ground state, but in an excited state. The excitation will be lost, if the nickel emits one or two γ-photons depending on the kind of excitation state.

the ground state. The meta-stable states differ from the excited states because its half-life is a lot of higher then the half-lifes of the excited states. Meta-stable states are characterized by a m in the mass number: ${}^{xxxm}X$. A famous example is the meta-stable state Pa-234m [9], which is needed in later MCNP-calculations as well.

3.3 Bremsstrahlung

The exact explanation of *bremsstrahlung* is, when a charged particle (usually an electron) interacts with matter and then electromagnetic radiation is emitted. The electromagnetic radiation can occur in form of one or more photons. At energies up to 200 keV the radiatation appears as X-rays and over 200 keV as γ-radiation.

The origin of bremsstrahlung can be explained on the basis of figure 3.2. An accelerated electron which has a kinetic energy E_{kin} after the acceleration, interacts with the Coulomb field of an atom. Here, the electron is deflected and accelerated in a different direction. It loses a kind of its kinetic energy that is emitted in form of bremsstrahlung. This process can happen several times until the electron do not longer offer kinetic energy. By these processes several photons are emitted and a

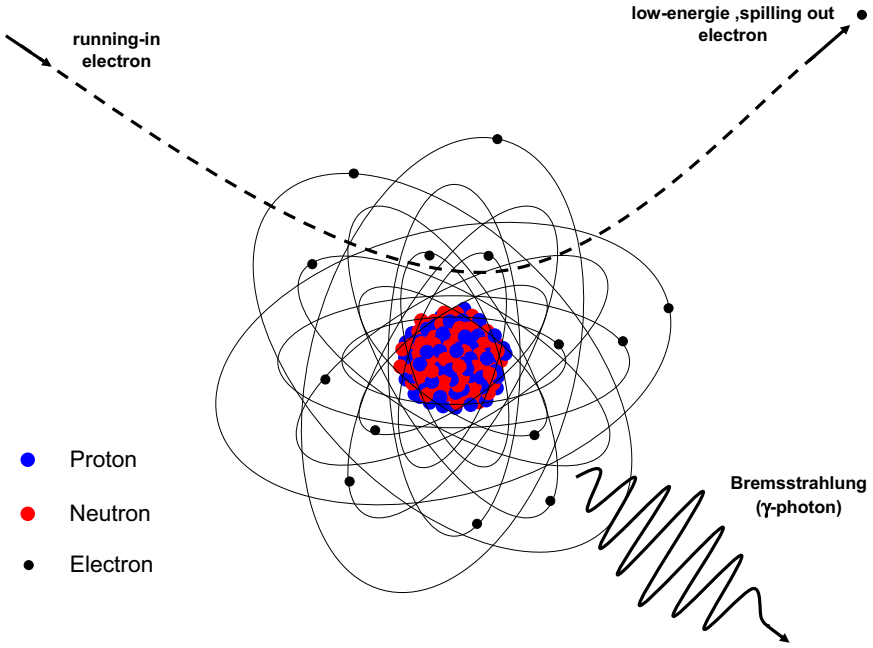

Figure 3.2: Scheme of the producing bremsstrahlung by scattering an electron in the Coulomb field of a nuclide.

continuous bremsstrahlung spectrum occurs.
If an electron emits in the initial interaction with an atom already its complete kinetic energy in form of a photon, a *critical wavelength* λ_{min} will occurs in the bremsstrahlung spektrum. Photons with shorter wavelengths are prohibited. The critical wavelength can be defined by the simple equation 3.12 (Duane-Hunt law [10])

$$\lambda_{min} = \frac{h \cdot c}{E_{kin}} \tag{3.12}$$

in which $E_{kin} = E_{photon}$, c the velocity of light and h the Planck constant. The critical wavelength of the bremsstrahlung is therefore only dependent on the kinetic energy of the electron. The higher the kinetic energy is, the shorter is the wavelength. Beside the continuous bremsstrahlung spectrum, characteristic X-rays occurs which are presented as discrete peaks with a larger intensity than the continous bremsstrahlung in the radiation spectrum and depends on the interacting material. The emergence of the characteristic X-rays can be described by the Bohr model [11, 12, 13]. A free, high-energy electron hits from the absorbent material a bound electron from an inner shell of its atom. The kinetic energy of the free electron must be at least as large that the jolt electron is excited to an unoccupied shell or completely ejected from the atomic shell. The atom is then in an ionized state. The created hole in the inner shell must be filled by an electron from an outer shell. Since the electron in the

outer shells have a lower binding energy than the electrons in inner shells, this energy difference must be compensated by emitting electromagnetic radiation. The typical energy difference between the electron shells is 1-100 keV, so that the electromagnetic radiation occurs as X-rays. This energy difference is element specific and depends on the absorbent material, so that the type of X-rays are called: *characteristic X-rays*. The characteristic X-rays are not produced by the acceleration or deflection of the electrons through the absorbent material, but by electron transitions in the electron shells. Completely, the characteristic radiation was still mentioned briefly in order to describe all the *external* effects of the interaction of electrons with a absorbent material. *Internal* bremsstrahlung are described a few lines below.

Bremsstrahlung can be caused by a variety of ways, but the physical principle remains always the same. For one, bremsstrahlung can be produced in a X-ray tube. The electrons which are developed at a cathode are accelerated with an acceleration voltage and are shot on a anode material. The interaction of electrons with the anode material produce bremsstrahlung. The maximum energy of bremsstrahlung, according to equation 3.12, depends on the accelerating voltage.
Another method for the production of bremsstrahlung is the interaction of β^--particles with the surrounding matter. This process will be still relevant in this work later. Here, the electrons (β^--particles) which are released through a β^--decay (see reaction equation 3.13) have a kinetic energy that can be transformed in bremsstrahlung by interaction with surrounding matter.

$$ {}^{A}_{Z}X \rightarrow {}^{A}_{Z+1}Y + e^- + \bar{\nu}_e \tag{3.13} $$

where X is the decaying nuclide, Y the daughter nuclide and $\bar{\nu_e}$ the electron antineutrino. Since the electrons in β^--decay have different energies because the decay-energy is differently splitted on the electron and daughter nuclide, a continuous bremsstrahlung spectrum is created.
Beside the above described effects of the external bremsstrahlung, also *internal* bremsstrahlung occurs by sudden change of the nuclear charge in an atom. The easiest way to describe this effect is using the example of a β-decay. The β-particles leaves the atom completely and a sudden change in the nuclear charge occurs which has to be compensated in form of bremsstrahlung. In addition to these continuous bremsstrahlung spectrum *internal ionization* arise and leads to *internal characteristic* electromagnetic radiation.

3.3.1 Thin target bremsstrahlung

By irradiating a thin target with monoenergetic electrons, bremsstrahlung is produced. The examined target is so thin, that the electrons lose no appreciable energy by ionization with the target atoms and suffer no significant elastic deflection, but lose only energy by the interaction with the Coulomb field of the target atoms and the energy lose is compensated by irradiating bremsstrahlung. These are very simple assumptions to describe the bremsstrahlung of electrons which pass through a thin target. Normally these assumptions practically do not occur under laboratory conditions because the targets are normally thick (e.g. X-ray tube). Since the later MCNP-calculations of bremsstrahlung are calculated in thick targets, this consideration of bremsstrahlung in thin targets must be understood because the thick target bremsstrahlung is the sum of the contributions from a number of thin target cases of various electron energies (see section 3.3.2). A target is called thin, when the thickness of the target is smaller than the range of the electron in the target.

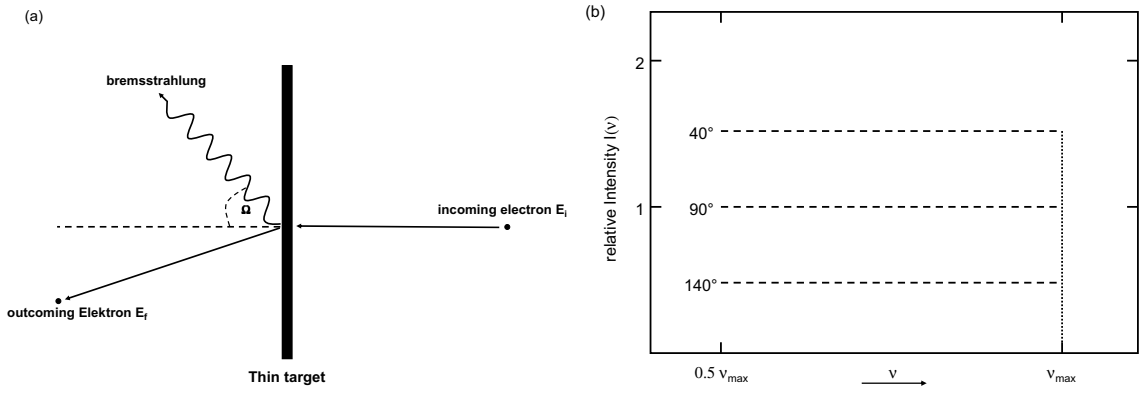

Figure 3.3: (a) Scheme of thin target bremsstrahlung. The incoming electron with the inital kinetic energy E_i interacts with the Coulomb field of the atoms in the thin target and bremsstrahlung occurs. After interaction the electron has the lower final kinetic energy E_f. (b) The relative intensiy of bremsstrahlung is independent of the frequency (adopted from [14]).

In figure 3.3(a) a scheme of generating bremsstrahlung in a thin target is shown. The incoming electron with the inital kinetic energy E_i interacts with the Coulomb field of the atoms in the thin target, however do not lose the whole kinetic energy but passes through the target and has a final kinetic energy E_f which is smaller than the inital kinetic energy.
Figure 3.3(b) clearly shows that the bremsstrahlung from electrons of a given energy $E_i = const.$, in any particular direction Ω, has a relative intensity (energy per photon $\cdot$ number of photons) which is constant for all bremsstrahlung photon energies

and cuts off abruptly at a maximum energy of $h\nu_{max}$. This means that the intensity $I(\nu)$ is independent on the frequency of the bremsstrahlung photons.
Furthermore, it is clear that the radiation intensity (relative number of photons) of bremsstrahlung, in a perticular direction Ω from various nonrelativistic energies varies as $1/E_i$. Due to this the radiation intensity of bremsstrahlung decreases with increasing electron energy.
Another important property of thin target bremsstrahlung is, that at low electron energies the radiation intensity has a maximum at right angles to the incoming direction of the electron. The more the electron energy increases, the more the radiation intensity shifts to the forward direction (180° to the incoming direction of the electron).

3.3.2 Thick target bremsstrahlung

The thin target bremsstrahlung is a highly idealized case, rarely met in practise. Therefore, the thick target bremsstrahlung is none the less the usual laboratory situation for electrons which interact with matter. In the case of a thick target still monoenergetic electrons are assumed with a certain initial kinetic energy to produce bremsstrahlung.
The spectral distribution of thick target bremsstrahlung can be assumed as the sum of the contributions from a number of thin target cases of various electron energies (see figure 3.4(b)). The electron energy varies because the incoming electron is slowing down by ionizing collisions and interactions with the Coulomb field of the atoms in the upper layers of the thick target so that the superpposition of thin targets curves have diminishing values of $h\nu_{max}$. Figure 3.4(a) shows the ionizing collisions of a electron in the upper layers of the thick target and the associated energy loss. At a certain range, the electron loses the whole kinetic energy and can not penetrate another thin target.

Figure 3.4(b) also provides information about the fact, that each electron with a particular energy (also electrons from β-decay which energies varies from 0 MeV to a maximum energy E_{max}) generates its own bremsstrahlung spectrum. This statement is important for the later calculations of bremsstrahlung with MCNP because an alternative *equivalent continous bremsstrahlung spectrum* is used to calculate the effective dose rate of bremsstrahlung photons. This alternative bremsstrahlung spectrum is explained in section 4.2.

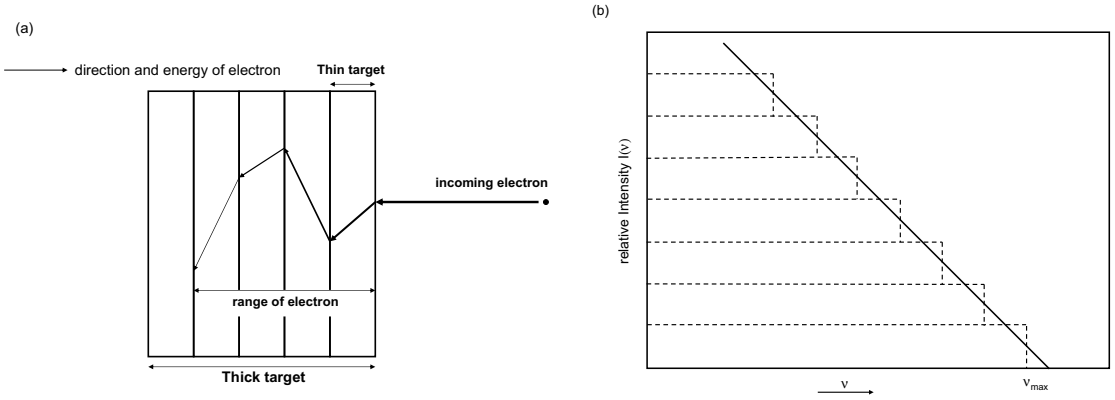

Figure 3.4: (a) Scheme of thick target bremsstrahlung. The electron loses in every thin target a part of the kinetic energy (illustrated by the thickness of the arrows) till the electron has no more kinetic energy. (b) The relative bremsstrahlung intensity of a thick target can be regarded as the sum of a number of thin target curves with diminishing values of $h\nu_{max}$ because of ionizing collisions in the layers (adopted from [15]).

3.4 Neutron radiation

In this section, two models are presented which act by nuclear physical processes as a neutron source. This is first of all the spontaneous fission and secondly the (α, n)-reaction. The neutrons emitted in these processes have a continuous energy distribution and due to this, multiple interaction processes with matter occur simultaneously. This leads to the decision that neutron radiation supplies a non-negligible contribution to dosimetry. Besides the above mentioned neutron sources, there is the (γ, n)-reaction which can act as a neutron source, too. This is conditioned by a mixture of a γ-emitter and a material which has a high cross section with respect to the (γ, n)-reaction. Since this type of neutron source is not relevant for this work, it is not discussed further more.

3.4.1 Spontaneous fission

Spontaneous fission is a nuclear reaction that occurs as a radioactive decay. Due to this, a heavy nucleus with a very high proton number divides from its ground state or an excited state without any excitation into two medium-heavy nuclei. It usually occurs at a much lower probability next to the prevailing α-decay of the respective nucleus. The reaction equation of a spontenues fission is given as:

$$X \rightarrow Y_1 + Y_2 + \nu \cdot n$$

with X as the splitting nucleus and Y_1 as the first fission fragment and Y_2 as the

second fission fragment which has often not the same mass number. In addition to the two resulting fission fragments a certain number of neutrons $\nu \cdot n$ are emitted and shows, that the spontaneous fission is a strong neutron source. The number of neutrons depend on the kind of splitting nucleus. The declaration of a spontaneous fission is, that the nucleus must override or tunnel through a Coulomb barrier. The Coulomb barrier of the spontaneous fission has however a more complicated form than the Coulomb barrier of an α-decay [16]. And by these facts, the quantum-mechanical description of spontaneous fission is more difficult than that of the α-decay. In the following a demonstrative description of spontaneous fission is described and can be compared with figure 3.5.

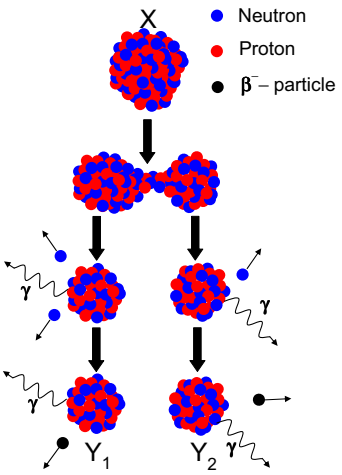

Figure 3.5: Scheme of a spontaneous fission. The nucleus goes into oscillation and breaks into two fission fragments which are in an excited state and loses the excited energy by emitting neutrons or γ-photons. The remaining excess of neutrons in the fragments are transformed by β^--decay (adapted from [5]).

To understand the process of spontaneous fission, the nucleus X is taken as a drop of incompressible fluid, that can accept various deformations. First, the nucleus with mass number A and atomic number Z goes into 'oscillation' and laced together in one spot. Subsequently, the nucleus divides into two fission fragments Y_1 and Y_2. Depending on the point of constriction, the fission fragments get more different masses and excitation energies to each other (*asymmetric fission*). However, the fission fragments can also have the same mass and excitation energy (*symmetric fission*). From experiments it is known, that the asymmetric fission is much more probable than the symmetric fission [17]. After splitting, the Coulomb repulsion affects, so that the fission fragments removed with a high kinetic energy to each other. The excited fission fragments lose their excitation energies by emitting neutrons.

Remaining excitation energy is emitted in form of γ-photons. Fission fragments which have still a high neutron excess after this processes, convert it by a chain of successive β^--decays in order to achieve a stable state.
To explain the spontaneous fission, terms of the *liquid drop model* [18] are used. Due to this it should also be assumed that the nucleus can accept a ellipsoidal form. If the nucleus is deformed at the spontaneous fission, terms of the liquid drop model will be used which are dependent on the deformation of the nucleus. These are the Coulomb term E_c and the surface term E_s because both terms depend on the radius R of the fissioning nuclide. Taking into account, that the eccentricity ϵ (if $\epsilon = 0$, the nucleus will have the form of a sphere) of the ellipsoidal form and the relation $R = r_0 \cdot A^{1/3}$, with $r_0 = 1.4 \cdot 10^{-15}\ m$ as the radius of a nucleus, surface term and Coulomb term get following expressions:

$$E_s = a_s \cdot A^{2/3} \left(1 + \frac{2}{5}\epsilon^2 + ...\right) \qquad \text{Surface term} \qquad (3.14)$$

$$E_c = a_c \frac{Z(Z-1)}{A^{1/3}} \left(1 - \frac{1}{5}\epsilon^2 - ...\right) \qquad \text{Coulomb term} \qquad (3.15)$$

with $a_s \approx 17.23\ MeV$ and $a_c \approx 0,714\ MeV$ as the surface and Coulomb constants from the Bethe-Weizsäcker equation [19]. The Coulomb term has in the ellipsoidal form less distibutive Coulomb energy because the charges are father apart from the average. Contrariwise, the nucleus has in the ellipsodial form a greater surface area, so that the surface term involves some loss of binding energy.
Taking only the terms in ϵ^2, this leads to the statement

$$a_c \frac{Z^2}{A^{1/3}} \left(\frac{1}{5}\epsilon^2\right) \geq a_s \cdot A^{2/3} \left(\frac{2}{5}\epsilon^2\right) \qquad (3.16)$$

for $Z \gg 1$. By reducing this equation it gets the form

$$\frac{Z^2}{A} \geq 2\frac{a_s}{a_c} \approx 48 \qquad (3.17)$$

Equation 3.17 states, that nuclei with $\frac{Z^2}{A} < 48$ are stable against small deformations and carry no spontaneous fission. For nuclei with $\frac{Z^2}{A} \geq 48$ smallest deformations of the core can lead to spontaneous fission. Often the *fissility parameter* x is introduced instead of equation 3.17 which also makes a statement about the spontaneous fission of nuclei (see equation 3.18).

$$x = \frac{a_c}{a_f}\frac{Z^2}{2A} \qquad (3.18)$$

If $x < 1$ the nucleus will be stabil against smallest deformation, but if $x \geq 1$ spontaneuos fission will possibly occur. Nevertheless, nuclei with a fissility parameter $x < 1$ can absolve spontaneous fission, when the deformation is strong enough. The previously presented model describes a simplified model of spontaneous fission. To make more accurate values for overcoming the energy barrier for heavy nuclei to perform spontaneous fission, the *shell model* [20] has been added in addition to the liquid drop model. Particularly good values are provided by the *hybrid model* [21] of Strutinsky.
For medium-heavy nuclei, the probability of an α-decay is much higher than the probability for spontaneous fission. This can be good illustrated by the example of uranium-238 which indicate a partial half-life of $4.47 \cdot 10^9$ a for the α-decay and for spontaneous fission $9 \cdot 10^{15}$ a. For heavy nuclei, the probability increase for spontaneous fission. For very heavy nuclei with a high number of neutrons, spontaneous fission outweighs that of the α-decay. The half-lives of spontaneous fission of some nuclei are illustrated in table A1 in the appendix.

3.4.2 (α,n)-reaction

Another nuclear reaction which produces neutrons is the so called (α,n)-reaction which can be described by the following reaction equation

$$ {}^{A}_{Z}X + {}^{4}_{2}He \rightarrow {}^{A+3}_{Z+2}Y + n + Q \tag{3.19} $$

with ${}^{A}_{Z}X$ as the target nucleus, ${}^{4}_{2}He$ the α-particle, ${}^{A+3}_{Z+2}Y$ the final nucleus, n the neutron and Q the amount of energy released by the reaction. A positive Q-value describes an *exothermic* reaction, while a reaction with a negative Q-value is *endothermic*.
Here an α-particle with a kinetic energy hits a target nucleus, while overcoming the Coulomb barrier. The result of this reaction is a free neutron and a final nucleus which has in contrast to the target nucleus additionally two protons and one neutron. By the excess of protons, the final nucleus is in an instabil system and has a weak bond, so that it is usually radioactive [22]. This is usually a disadvantage because the high excitation energie of the nucleus produces in addition to the neutron radiation still hard γ-radiation.
The excitation of the target nucleus is defined by the binding energy and the kinetic energy of the α-particle. If the excitation energy of the target nucleus is larger than the binding energy of the "last neutron", it will be very likely that a neutron leaves the nucleus. The remaining excitation energy is distributed as kinetic energy between the

neutron and the target nucleus [23]. The binding energy, i.e. the separation energy of the last neutron in some selected light nuclei is shown in table 3.3.

Nucleus	Binding Energy in MeV	Nucleus	Binding Energy in MeV
H^2	2.225	C^{12}	18.720
H^3	6.258	C^{13}	4.937
He^3	7.719	C^{14}	8.176
He^4	20.577	N^{14}	10.553
Li^6	5.663	N^{15}	10.834
Li^7	7.253	O^{15}	13.222
Be^8	18.896	O^{17}	4.142
Be^9	1.665	O^{18}	8.047
B^9	18.575	F^{18}	9.141
B^{10}	8.440	F^{19}	10.442
C^{11}	13.092	F^{20}	6.599

Table 3.3: Binding energy in MeV of the "last neutron" of some selected nuclei (adopted from [24]).

The last neutron which is important for the $^{19}F(\alpha,n)^{22}Na$-reaction in later MCNP-calculations occurs from the fluorine-19 nucleus and has a binding energy of 10.442 MeV. Hence, the sum of the binding energy and the kinetic energy of the α-particle must have a minimum value of 10.442 MeV, so that a neutron is emitted. The neutron yield of the (α,n)-reaction is defined by the penetrability of the Coulomb barrier. The penetrability of the Coulomb barrier of α-particles is very high for light nuclides. For heavy nuclei, the penetrability is very low due to the high Coulomb barrier. Therefore, the α-particle require energies in the order of 5-10 MeV. To generate a lot of neutrons by the (α,n)-reaction, light nuclides are in advantage. If none or only a few neutrons should be produced by this reaction, it will be convenient to use heavy nuclei.

3.5 Radioactive equilibrium

Unstable radionuclides decay not necessarily to a stable nuclide, but can decay into an unstable radionuclide again. This can go over several times, till a stable nuclide is finally reached. This phenomenon is particularly common in the natural radioactive series and thus for the uranium isotopes.

$$\text{Nuclide 1} \rightarrow \text{Nuclide 2} \rightarrow \cdots \rightarrow \text{Nuclide k}$$

To determine the activities of the nuclides, the number N_k of the unstable nuclides are investigated. The temporal change of the number of particles N_k of a nuclide is given by equation 3.20:

$$\frac{dN_k}{dt} = \lambda_{k-1} N_{k-1} - \lambda_k N_k \tag{3.20}$$

with $\lambda_{k-1} N_{k-1}$ as the *accession rate* of nuclide k which is equal to the decay rate of nuclide $k-1$ and $-\lambda_k N_k$ as the decay rate of nuclide k. The temporal change for the mother nuclide is:

$$\frac{dN_1}{dt} = -\lambda_1 N_1. \tag{3.21}$$

By determining this set of differential equations with the initial conditions $t = 0$, that

$$N_1 = N_1^0 \text{ and } N_2^0 = N_3^0 = N_k^0 \cdots = 0$$

the number of particles $N_k(t)$ for the nuclide k at the time t is defined by equation 3.22

$$N_k(t) = c_1 e^{-\lambda_1 t} + c_2 e^{-\lambda_2 t} + \cdots + c_k e^{-\lambda_k t}, \tag{3.22}$$

with the constant coeffecients:

$$\begin{aligned}
c_1 &= \frac{\lambda_1 \lambda_2 \ldots \lambda_{k-1}}{(\lambda_2 - \lambda_1)(\lambda_3 - \lambda_1) \ldots (\lambda_k - \lambda_1)} N_1^0 \\
c_2 &= \frac{\lambda_1 \lambda_2 \ldots \lambda_{k-1}}{(\lambda_1 - \lambda_2)(\lambda_3 - \lambda_2) \ldots (\lambda_k - \lambda_2)} N_1^0 \\
&\ldots\ldots \\
c_k &= \frac{\lambda_1 \lambda_2 \ldots \lambda_{k-1}}{(\lambda_1 - \lambda_k)(\lambda_2 - \lambda_k) \ldots (\lambda_{k-1} - \lambda_k)} N_1^0.
\end{aligned}$$

By multiplying the number of particles $N_k(t)$ with the disintegration constant λ_k, the activity $A_k(t)$ of the unstable nuclide is determined. With the aid of equation 3.22, all activities at a given time t of the nuclides of a natural radioactive series can be calculated. It describes the approach of the radioactive equilibrium as a function of time with a quantitative abscission of the nuclide k from the mother nuclide [5]. The radioactive equilibrium from a nuclide k and the mother nuclide will be achieved, if the ratio of the activities A_k/A_1 is constant. In the following, two different kinds of a radioactive equilibrium are explained.

Secular equilibrium

If the half-life of the mother nuclide is much larger than the half-life of the daughter nuclide or $\lambda_1 \ll \lambda_2$, eqaution 3.22 is reduced to

$$N_2(t) = \frac{\lambda_1}{\lambda_2} N_1(t) \left(1 - e^{-\lambda_2 t}\right) \tag{3.23}$$

or in expression of the activity

$$A_2(t) = A_1(t) \left(1 - e^{-\lambda_2 t}\right) \tag{3.24}$$

Due to the fact that the disintegration constant of the mother nuclide is much smaller than the disintegration constant of the daughter nuclide, the activity of the mother nuclide is in effect constant, i.e. $A_1(0) = A_1(t)$. Hence, the disintegration constant of the daughter nuclide is magisterial relevant for the secular equilibrium of the daughter nuclide and the mother nuclide after a sufficiently long time. The mother and daughter nuclide are in a radioactive equilibrium, when the expression in the brackets is equal to 1. An example for a secular equilibrium is shown in figure 4.2a, where U-238 and Th-234 plus the daughter nuclides of Th-234 are in a secular equilibrium after about 180 days. The activities of U-238 and Th-234 are then constant after this time. U-235 and Pa-231 are in a secular equilibrium too, but it takes a long time till the activities of U-235 and Pa-231 are constant in the simplified decay scheme. Over a period of 100 years, the activity of Pa-231 is still smaller by three orders of magnitude, than the activity of U-235.

Transient equilibrium

A transient equilibrium occurs, when the decay of the mother nuclide can not be neglected, as it is the case for the secular equilibrium. Here, the disintergration constant is only a little bit smaller than that of the daughter nuclide. The setting of the radioactive equilibrium as a function of time is given for the activity of the daughter nuclide by equation 3.25

$$A_2(t) = \frac{\lambda_2}{\lambda_2 - \lambda_1} A_1(t) \left(1 - e^{-(\lambda_2 - \lambda_1)t}\right) \tag{3.25}$$

For the setting of radioactive equilibrium, not only the half-life of the daughter nuclide is responsible, but the difference of the disintegration constants of the mother and daughter nuclide itself. This is illustrated by the expression in front of the brackets in equation 3.25, which represents the decay of the mother nuclide. Radioactive

equilibrium will be set, if the expression in the brackets is equal to 1 and equation 3.25 is reduced to

$$A_2(t) = \frac{\lambda_2}{\lambda_2 - \lambda_1} A_1(t) \tag{3.26}$$

The activities in secular equilibrium between daughter and mother nuclide are equal. In the transient equilibrium, the activity of the mother nuclide is a little bit smaller than the activity of the daughter nuclide (see equation 3.27)

$$A_1(t) = \left(1 - \frac{\lambda_1}{\lambda_2}\right) A_2(t) \tag{3.27}$$

An example for a transient equilibrium is the activity of U-232 and the daughter nuclide Th-228 (see figure 4.10a). The activity of U-232 decreases exponentially with time. Unlike than U-232, the activity of Th-228 builds up and reached its maximum after about 10.2 years and decreases after that maximum. U-232 and Th-228 are then in a transient equilibrium.

Chapter 4

Radiation from UF_6 cylinders

To calculate the effective dose rate, the radiation must be well known which escapes from the UF_6 cylinders. Therefore, this chapter describes exactly which radiation is used in the following MCNP-calculations and which radiation contributions can be neglected on the basis of conservative assumptions. Conservative assumptions are particularly important because the calculated values are always slightly higher than the measured values, so that the calculted values can be good used for interpreting the effective dose rate from the UF_6 cylinders at radiation protection. Furthermore, the MCNP simulation can be simplified with conservative assuptions which decrease the runtime of the simulation. However, attention must be paid to the calculated values by using conservative assumptions, that these values do not aberrate to much from the real values.
The total radiation which escapes from the UF_6-cylinders comprises neutrons and γ-photons and can be explained with the aid of six nuclear-physical processes. Following enumeration gives an overview over the emitted radiation particles with the associated physical processes.

1. γ-photons by decay of U-238 radioactive series
2. Bremsstrahlung-photons by β-decay of Pa-234m
3. γ-photons by decay of U-235 radioactive series
4. γ-photons by decay of U-232 radioactive series
5. Neutrons from spontaneous fission of U-238
6. Neutrons from $^{19}F(\alpha,n)^{22}Na$-reactions

The first three components derived from the naturally occurring uranium. γ-photons from the U-232 dacay developes from reprocessed uranium. Reprocessed uranium is produced, when fuel rods from nuclear power plants are reprocessed. This reprocessed uranium contains still about 1% U-235 which is about 0.3% more U-235 than natural uranium and important for further using in uranium enrichment facilities, but it contains also traces of U-232 and U-236. Spontaneous fission of U-238 is also a normal process in natural uranium and the (α,n)-reaction developes from the interaction between the α-particles of the uranium isotopes and the fluorine cores in UF_6, in which U-234 provides the largest contribution to the (α,n)-reaction.
In feed, product and tails are even small amounts of U-234. The radiation contribution of U-234 is not included in the γ-ray emission from the UF_6-cylinders because the γ-photons of this uranium isotope has a low energy and a low γ-yield. For example, γ-photons by decay of U-234 have an energy of 0.121 MeV and a γ-yield of $4 \cdot 10^{-4}$ photons per decay. This leads to a very small contribution to the effective dose rate which can be neglected.
Both to the γ-radiation as well to the neutron radiation the U-236 contribution is not taken into account because the U-236 and its direct subsequent daughter nuclide Th-232 have a very large half-life ($2.3 \cdot 10^7$ a for U-236 and $1.405 \cdot 10^{10}$ a for Th-232) which leads to a very low activity of Th-232 and its daughter nuclides. Furthermore, U-236 and the daughter nuclides have no significant γ-lines, so that they have not an influential contribution to the effective dose rate.
By the $^{19}F(\alpha,n)^{22}Na$-reactions of the α-particles with fluorine in UF_6, Na-22 is produced. Na-22 is a radioactive nuclide and decays by a β^+-decay to the stable isotope Ne-22. After the decay of Na-22, γ-radiation is emitted with an energy of 1.27453 MeV. The energy of this γ-line is very high and is normally observed in radiation protection. But the specific activity of the (α,n)-reaction and by this the specific activity (about 0.05 γ/s/gU in natural Feed) of Na-22 is for γ-radiation with such an energy to small to achieve a appreciable contribution to the effective dose rate. Due to this, the decay of Na-22 is not observed in the following MCNP-calculations.

4.1 γ-photons by decay of U-238 radioactive series

As mentioned above, the γ-radiation from the decay of the U-238 radioactive series carries a significant contribution to the total radiation. It occurs when the decay of these nuclides are still in an excited state after an α- or β-decay because the whole decay energy is not given to the α- or β-particle, but leave an excitation energy to the nucleus of the nuclide. The ground state of the nucleus can be reached when

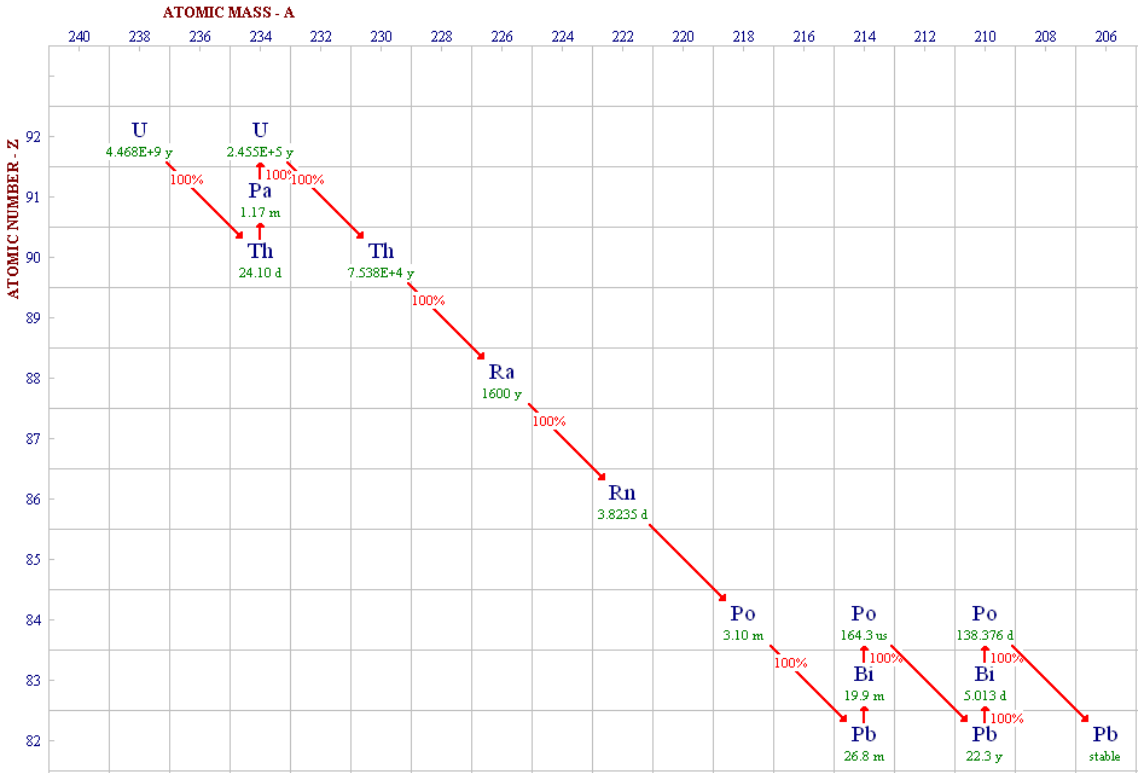

Figure 4.1: Radioactive series of U-238. The atomic number Z is plotted against the atomic mass A, so that the different types of decays can be illustrated. The radioactive half-life is given for each nuclide (green) (adopted from [25])

the excited nucleus emits the excitation energy in form of γ-radiation (see section 3.2). To determine the emergent γ-radiation, it is necessary to know the nuclides from this radioactive series which give a significant contribution to the γ-radiation. So it makes sense to consider the radioactive series of U-238 (see figure 4.1) and the behaviour of the activity of the daughter nuclides (see figure 4.2a).

By the decay of U-238 the daughter nuclide Th-234 (thorium) is produced with a radioactive half-life of 24.1 days. Pa-234 (protactinium) and Pa-234m is produced by the decay of Th-234. Pa234 has a radioctive half-life of 6.70 hours and Pa234m a radioactive half-life of 1.17 minutes. This is very short compared to material storage applications which has a period of 1 - 100 years. It can be assumed, that the decay of the daughter nuclides Pa-234 and Pa-234m occur nearly promptly after decay of Th-234. U-234 is produced after decay of Pa-234 and Pa-234m, but has a radioactive half-life of $2.455 \cdot 10^5$ years. U-234 has no significant γ-lines, so that the radioactive series can be broken at this point because no relevant γ-photons are produced which are important for the dose equivalent rate. So it emerges that with the decay of the

U-238 radiactive series U-238, Th-234, Pa-234 and Pa-234m deliver contributions to γ-radiation. Due to the fact, that Pa-234m and Pa-234 have a very short half-life the radioactive serie of U-238 can be simplified by a 3-level decay scheme (see figure 4.2b). The time behaviour of the ratios of U-238 and its daughter nuclides are presented in figure 4.2a. The ratio is plotted against the time t in days. The ingrowth times of Pa-234 and Pa-234 are the same as the ingrowth time of Th-234 due to the short half-life. Since the disintegration constant $\lambda_{Th-234} \gg \lambda_{U-238}$, the ratio of the activity of U-238 and Th-234 is defined as follows (see equation 4.1):

$$\frac{\lambda_{Th-234} N_{Th-234}(t)}{\lambda_{U-238} N_{U-238}(0)} = 1 - e^{-\lambda_{Th-234} \cdot t} \tag{4.1}$$

Th-234, Pa-234 and Pa-234m is in a secular equilibrium with U-238 and have the same activity like U-238 after a ingrowth time of about 150 days.

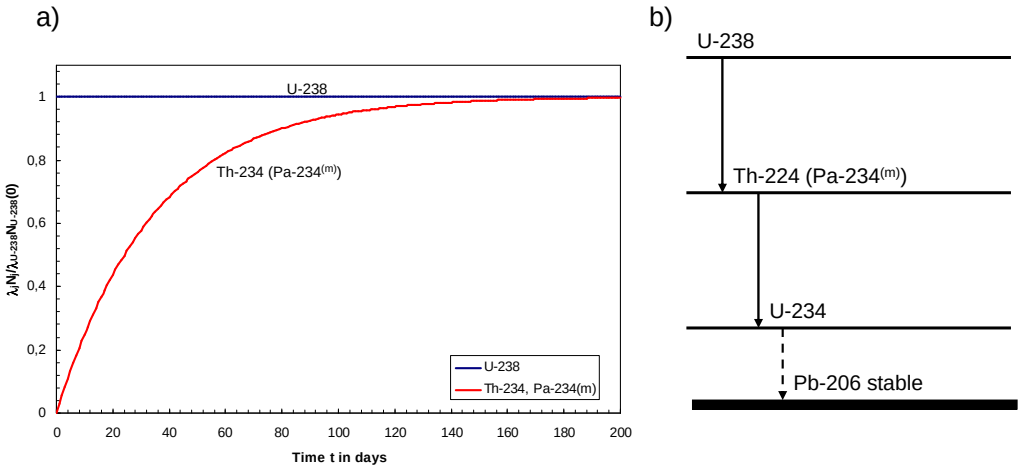

Figure 4.2: a) The ratios of the activities of U-238 and its daughter nuclides is plotted against the time t in days. b) Simplified 3-level decay scheme of the U-238 radioactive series.

With the aid of gamma-spectroscopy and theoretical calculations, γ-energies and corresponding intensities of a radionuclide can be determined. Today, these methods are used to get the γ-lines of radionuclides after decaying. The *Evaluated Nuclear Structure Data File* (ENSDF) [26] is a collection of various radionuclides and their properties. In this collection the energy levels of the individual γ-lines are listed up. Therefore, ENSDF also provides the γ-lines for the corresponding nuclides U-238, Th-234, Pa-234 and Pa-234m (see figure 4.3) which will be used in later numerical MCNP-calculations.

The photon yield which is a measure for the number of γ-photons per decay is plotted logarithmical against the energy of the γ-photons which has an energy range

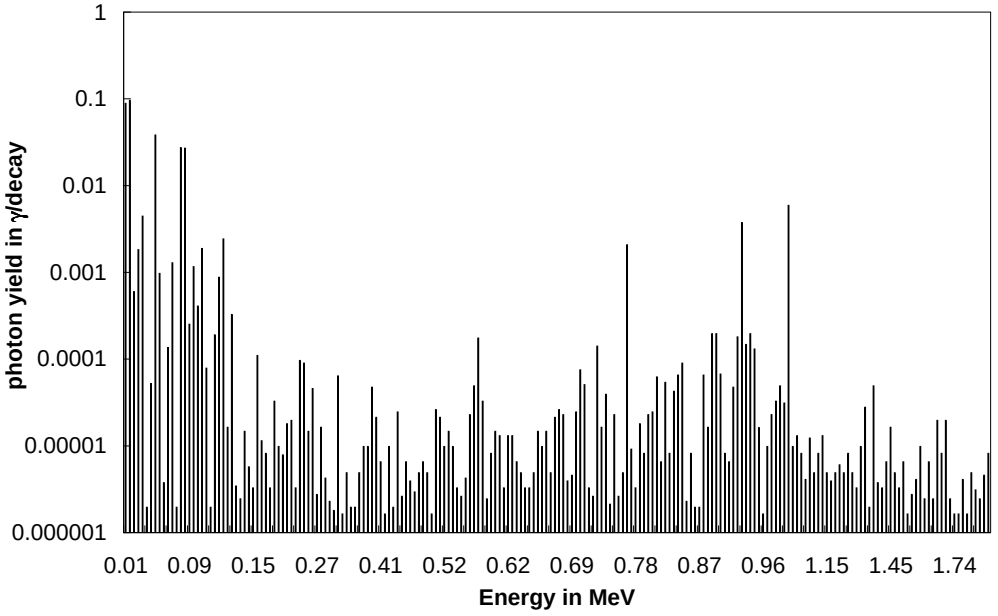

Figure 4.3: Discrete γ-energy spectrum of the radionuclides U-238, Th-234, Pa-234 and Pa-234m. The photon yield which is a measure for the number of γ-photons per decay is plotted logarithmical against the energy of the γ-photons.

from 0.013 MeV to 1.926 MeV. Each of these energy levels carries a more great or more less contribution to the effective dose rate. γ-photons with high energy and high photon yield are more important for the height of the effective dose rate than the γ-photons with lower energy, but with the same photon yield. This is the case because the γ-photons with lower energies are fatser attenuated in the surrounding matter of UF_6 and steel and therefore earlier absorbed than γ-photons with high energies.

4.2 Bremsstrahlung-photons by β-decay of Pa-234m

Bremsstrahlung which occurs by the interaction of electrons from the daughter nuclide of U-238 and the surrounding matter (cylinder wall, uranium and decay products) deliver a non-negligible contribution to the dose calculation. Therefore, the bremsstrahlung and the equivalent continous bremsstrahlung spectrum from the UF_6 cylinders is explained in the following.
The required electrons are from the β-decay of the daughter nuclide Pa-234m from the U-238 radioactive series. Other β-emitters from the radioactive series of U-238, U-235 and U-232 provide a negligible small contribution to the effective dose rate

because the electrons have very low kinetic energies and are therefore not included in the consideration of bremsstrahlung radiation. For this reason, only the electrons from Pa-234m are considered which have a maximum energy of $E_{max} = 2.29\ MeV$. The reaction equation of the β^--decay of Pa-234m is mentioned as follows:

$$^{234m}_{91}Pa \rightarrow ^{234}_{92}U + e^- + \bar{\nu}_e$$

The electron emission spectrum of β-emitters can be specified by a particular distribution (see equation 4.2)[15].

$$I(E) = A\sqrt{E}\,(E_{max} - E)^2 \tag{4.2}$$

Here $I(E)$ is the emission intensity of an electron with energy E emitted by an β-decay, E_{max} as the maximum kinetic energy of the electron and A as a constant. By normalizing equation 4.2 with the appropriation that each disintegration of Pa-234m in the UF_6 cylinder produces one electron and one anti-neutrino, the constant gets a value of $A = 0.163616$. The electron emission spectrum gets following shape by using these assumptions (see figure 4.4).

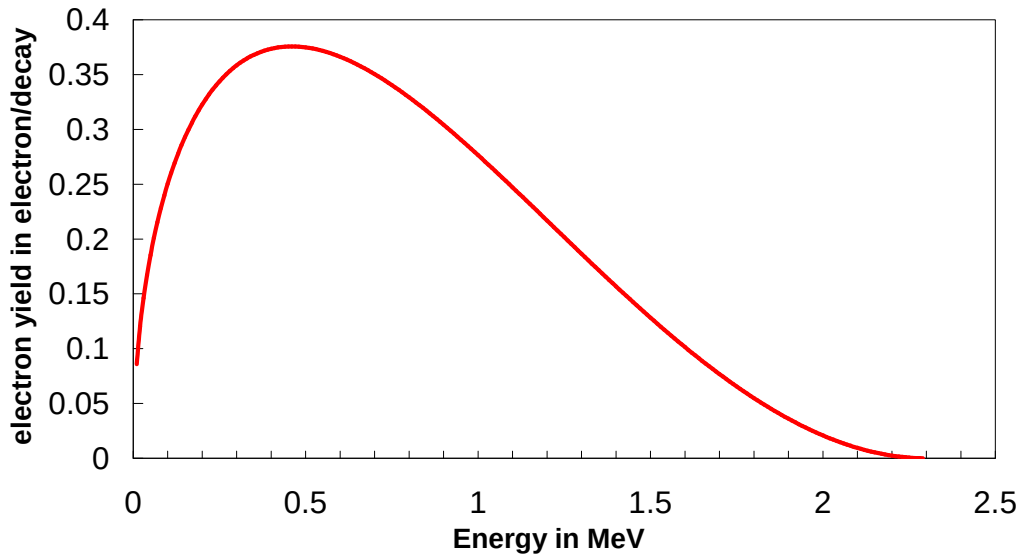

Figure 4.4: Illustration of the electron emission spectra of Pa-234m. The electron yield $I(E)$ is plotted against the kinetic energy E of the electron which occurs by the β-decay of Pa-234.

The electron emission spectrum mentioned above would generate bremsstrahlung photons through interaction with the surrounding matter and deliver a contribution to the total effective dose rate. The photon yield of the bremsstrahlung photons

which are produced by electrons depends on the material with which the electrons interact. Thus, for example, the interaction of electrons with pure iron of the UF_6 cylinder wall generates less bremsstrahlung photons than the interaction with pure UF_6. To calculate the effective dose rate with MCNP by simulating a electron-photon transport (e p-run) under usage of the electron emission spectrum, long calculation times (about several hours) are required to obtain a satisfactory result [27]. Therefore a equivalent bremsstrahlung spectrum is defined to reduce the calculation runtime, but getting the same results.

As known from section 3.3.2, each electron energy produced its own bremsstrahlung spectrum, where the photon intensity declines linear with increasing photon energy of the bremsstrahlung due to energy loss by ionization and deflection. With the aid of these information, a bremsstrahlung spectrum for each electron energy can be determined now. It should be noted, that the sum of the intensities of the bremsstrahlung photons is equal to the electron emission intensity at a given electron energy (see equation 4.3).

$$\sum_k M_k = I(E) \tag{4.3}$$

with $I(E)$ as the electron emission intensity at energy E and M_k as the discret bremsstrahlung emission intensities of the photon energies from $E = 0$ to E.
When the continuous electron energy is divided into N discrete linear electron energies and the bremsstrahlung photon energy, too, the intensities M_k of the bremsstrahlung photons for each electron energy can be determined by the following equation:

$$M_k = I(E)_n \cdot \frac{1}{n^2}(2k-1) \tag{4.4}$$

with $I(E)_n$ as the electron emission intensity at the discret energy value $n = 1, 2, 3, ..., N$ and M_k as the bremsstrahlung photon intensity of the bremsstrahlung photon energy at the position $k = 1, 2, 3, ..., N$. This equation 4.4 ensures that the bremsstrahlung photon intensities decreases linearly with increasing photon energy at a given discret electron energy at the position n. From the theory of the bremsstrahlung 3.3, the bremsstrahlung photon energy can not exceed the maximal kinetic energy of the electron (see equation 3.12). The above mentioned complex relationship is illustrated by an example in the appendix 7.

When the bremsstrahlung spectrum is created for each discrete electron energy and the intensity of the bremsstrahlung photons is summed up for each bremsstrahlung

energy, the result is the dependence of the bremsstrahlung emission intensity and the bremsstrahlung energy. By multiplication of the total bremsstrahlung photon intensity with the relative quanta intensity, the bremsstrahlung photon yield is defined and by this the equivalent continous bremsstrahlung spectrum is created (see figure 4.5).

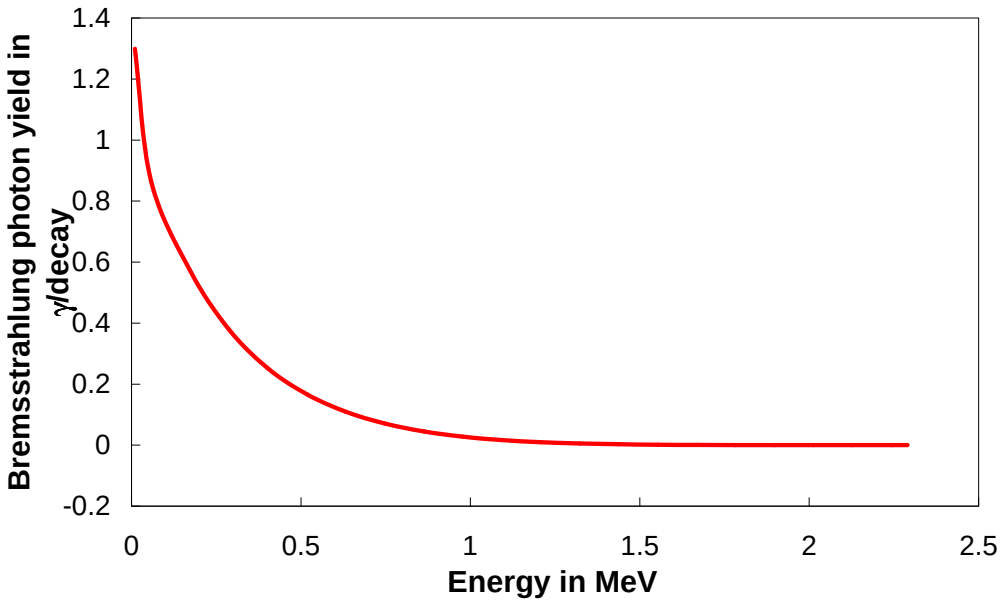

Figure 4.5: Illustration of the equivalent continous bremsstrahlung spectrum. The bremsstrahlung photon yield is plotted against the bremsstrahlung photon energy. This spectrum will be used in the following MCNP-calculations because it reduce the runtime of the calculation. The points are connected together to illustrate the continuity of the spectrum.

It is clearly seen that most of bremsstrahlung photons are in an energy range up to 0.5 MeV. The photon yield of bremsstrahlung which is produced by electrons of a β-emitter and the surrounding matter, is strongly shifted to lower energies. This support the argument, that every electron energy produces its own bremsstrahlung spectrum and the sum of these spectra gives a bremsstrahlungs spectrum which is shifted to lower bremsstrahlung energies.
The equivalent continous bremsstrahlung spectrum is used for the later MCNP calculations because it represents the emitted bremsstrahlung from an UF_6 cylinder in every aspect and reducues the runtime of the calculation by multiple orders of magnitude.

4.3 γ-photons by decay of U-235 radioactive series

Another source of γ-radiation in UF_6 are the γ-lines from U-235 and its daughter nuclides. Due to the fact, that the U-235 concentration increases in enriched uranium, the γ-photons of U-235 and its daughters gives a non-negligible amount to the effective dose rate for enriched uranium. But in later investigations it is shown, that these γ-photons does not play an important role for depleted uranium and natural feed because the amount of U-235 is in these cases much smaller than for enriched uranium. To determine γ-photons of the radionuclides which contribute to the effective dose rate, it is essential to take a look at the activity of U-235 and the ingrowth of the daughter nuclides. The radioactive series of U-235 and the half-life of the radionuclides are presented in figure 4.6.

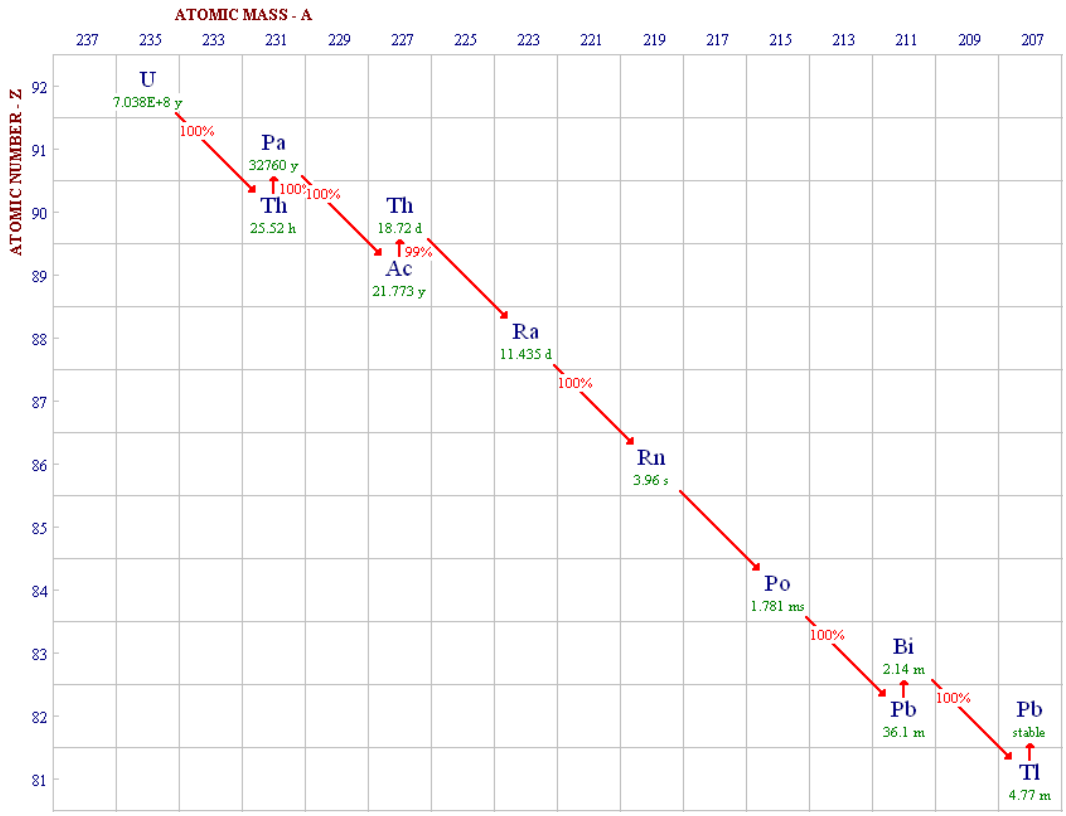

Figure 4.6: Radioactive series of U-235. The atomic number Z is plotted against the atomic mass A, so that the different types of decays can be illustrated. The radioactive half-life is given for each nuclides (green) (adopted from [25])

U-235 has a half-life of $7.038 \cdot 10^8$ years and decays by an α-decay to Th-231 which has a half-life of 25.52 hours. From the point of view of material storage applications the decay of Th-231 happens promptly after the decay of U-235. The daughter nuclide of Th-231 is Pa-231 with a half-life of 32760 years which developes by a β-decay of

Th-231. In this radioactive series there are further α- and β-decays until the stable nuclid Tl-207 is obtained.
With the aid of an simplified decay scheme (see figure 4.7b) of U-235 the important nuclides can be determined by the activity of the radionuclides. Since Th-231 has a very short half-life and the disintegration constant $\lambda_{Th-231} \gg \lambda_{U-235}$, the activity of Th-231 is in radioactive equilibrium with U-235. Due to the long half-life of U-235, the activity of U-235 is equal over several hundred years. The ratio of the activity of Pa-231 and U-235 has a linear expression due to equation 4.5 because the observed time $t \approx 100\ a$ in material storage application is much smaller than $\frac{1}{\lambda_{U-235}}$ and $\frac{1}{\lambda_{Pa-231}}$. Hence the ratio of the activity of U-235 and Pa-231 has the form

$$\frac{\lambda_{Pa-231} N_{Pa-231}(t)}{\lambda_{U-235} N_{U-235}(0)} = \lambda_{Pa-231} \cdot t \tag{4.5}$$

In figure 4.7a are the ratios of the activity of the nuclides logarithmical plotted against the time t in years. It is clear, that the activity of Pa-231 is still weaker by a factor of $1 \cdot 10^{-3}$ than the activity of U-235 even after 100 years of ingrowth time. This means that in comparison to U-235 and Th-231, Pa-231 and its daughter nuclides have a weak activity and must not be considered further more in MCNP-calculations of effective dose rate.

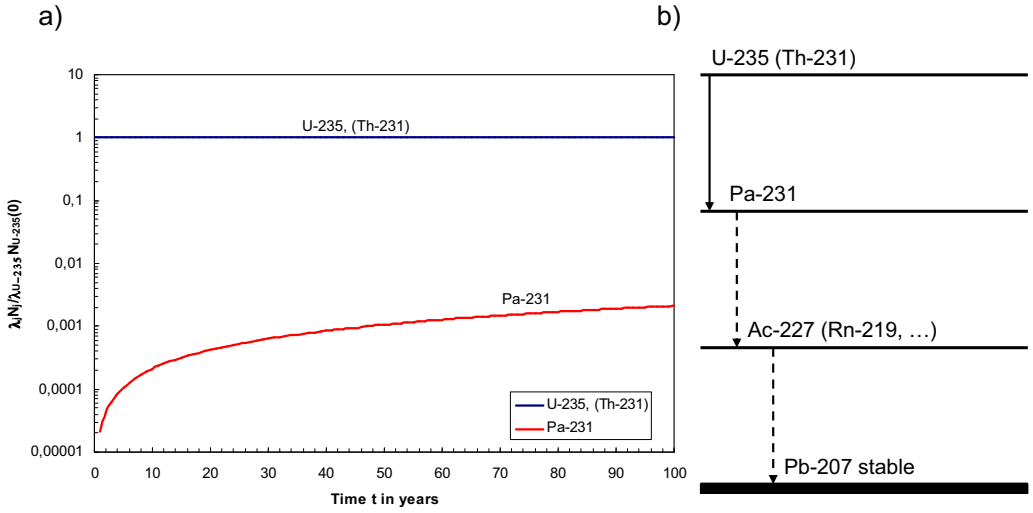

Figure 4.7: a) The ratios of the activities of U-235 and its daughter nuclides is plotted against the time t in years. b) Simplified 4-level decay scheme of the U-235 radioactive series.

Due to these factors, the γ-photons from the radionuclides U-235 and Th-231 are the important lines for the MCNP-calculations. The γ-lines from the U-235 and Th-231 are also taken from the *Evaluated Nuclear Structure Data File*[26] like the

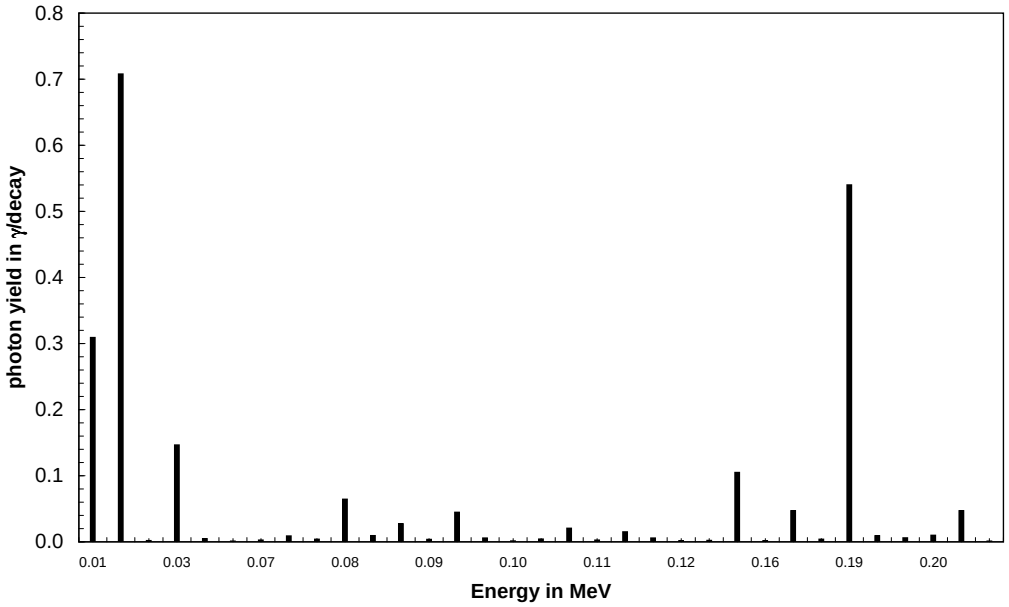

Figure 4.8: Discrete γ-energy spectrum of the radionuclides U-235 and Th-231. The photon yield which is a measure for the number of γ-photons per decay is plotted against the energy of the γ-photons.

γ-lines of the radionuclides of the U-238 radioactive series (see section 4.1) and are presented in figure 4.8. The γ-lines have an energy range between 0.013 MeV and 0.221 MeV. The 185.72 keV γ-line from the decay of U-235 has the most influence on the effective dose rate because it has high energy and high photon yield.

4.4 γ-photons by decay of U-232 radioactive series

Uranium 232 in UF_6-cylinder is contained when the uranium from used fuel rods of nuclear power plants is reprocessed and mixed with natural uranium which is then filled in UF_6-cylinders. The amount of U-232 is very low and may not exceed a certain limit. U-232 has a high specific activity of $8.11 \cdot 10^{11}$ Bq/gU^{232} and the daughter nuclides produce hard γ-rays, so that the γ-photons of U-232 and their daughters deliver a non-negligible contribution to the total effective dose rate.

To determine the γ-photons which will be produced by the decay of U-232 and their daughter nuclides, the radioactive series of U-232 is examined (see figure 4.9).

U-232 has a half-life of 68.9 years and decays by an α-decay to Th-228 which has a half-life of 1.9116 years. The subsequent daughter nuclides of Th-228 possess compared to material storage applications very short half-lifes between 0.299 μs and

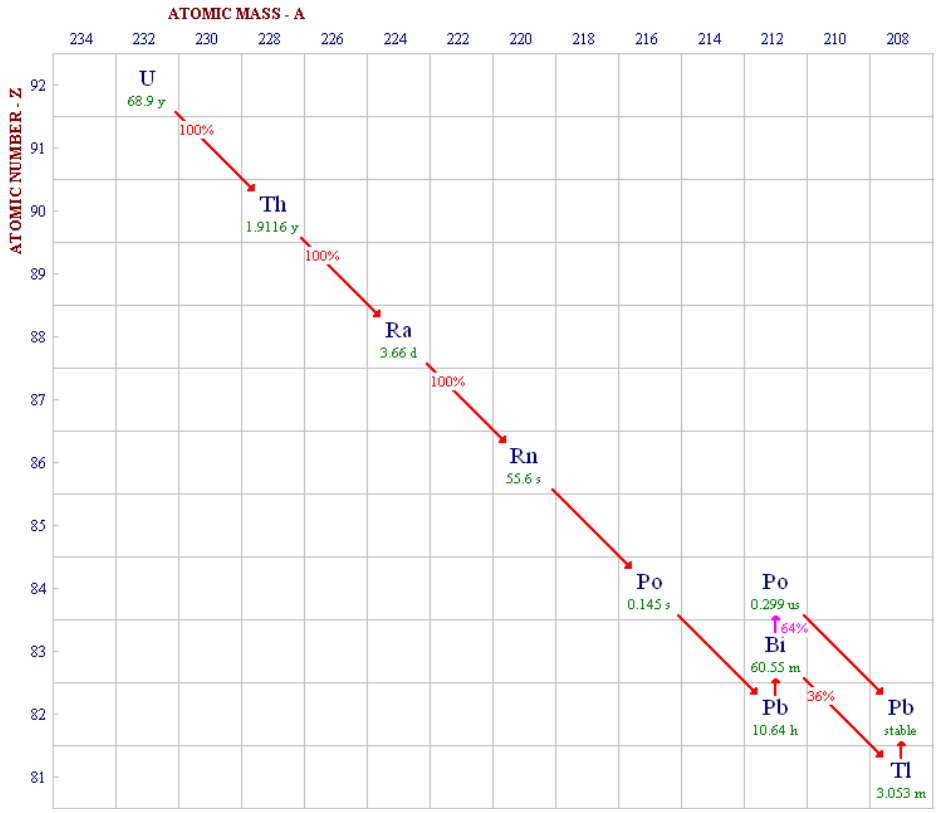

Figure 4.9: Radioactive series of U-232. The atomic number Z is plotted against the atomic mass A, so that the different types of decays can be illustrated. The radioactive half-life is given for each nuclides (green) (adopted from [25])

3.66 days. On the one hand Bi-212 (bismuth-212) goes with a probability of 64% to Po-212 (polonium-212) by a β-decay and on the other hand with a probability of 36% to Tl-208 (thallium-208) by an α-decay. Both branches lead directly to the stable nuclide Pb-208 (lead-208).

The U-232 radioactive serie can be simplified by a 2-level decay scheme (see figure 4.10b) because Th-228 and its daughters have very short half-lifes and are nearly promptly after decay of Th-228. With respect to the short half-lifes of the nuclides and the hard γ-radiation, all γ-photons from the nuclides (Th-228, Ra-224, Rn-220, Po-216, Pb-212, Po-212, Bi-212 and Tl-208) of the radioactive decay series can be considered in the γ-energy spectrum. The representation of the γ-energy spectrum is shown in figure 4.11. The time behaviour of the activity of U-232 itself is defined by equation 4.6 because the half-life of U-232 is much smaller than that of the other uranium isotopes, so that it has a significant change in time:

$$\frac{\lambda_{U-232} N_{U-232}(t)}{\lambda_{U-232} N_{U-232}(0)} = e^{-\lambda_{U-232} \cdot t} \tag{4.6}$$

The activity of Th-228 and its daughter nuclides is defined by equation 4.7:

$$\frac{\lambda_{Th-228} N_{Th-228}(t)}{\lambda_{U-232} N_{U-232}(0)} = \frac{\lambda_{Th-228}}{\lambda_{Th-228} - \lambda_{U-232}} e^{-\lambda_{U-232} \cdot t} (1 - e^{-(\lambda_{Th-228} - \lambda_{U-232}) \cdot t}) \qquad (4.7)$$

In figure 4.10a is the graphical representation of the ratio of the activity of U-232, Th-228 and its daughter nuclides. Th-228 and its daughter nuclides reach a maximum in activity after 10.2 years and decreases exponential after this time and is then in a transient equilibrium with U-232.

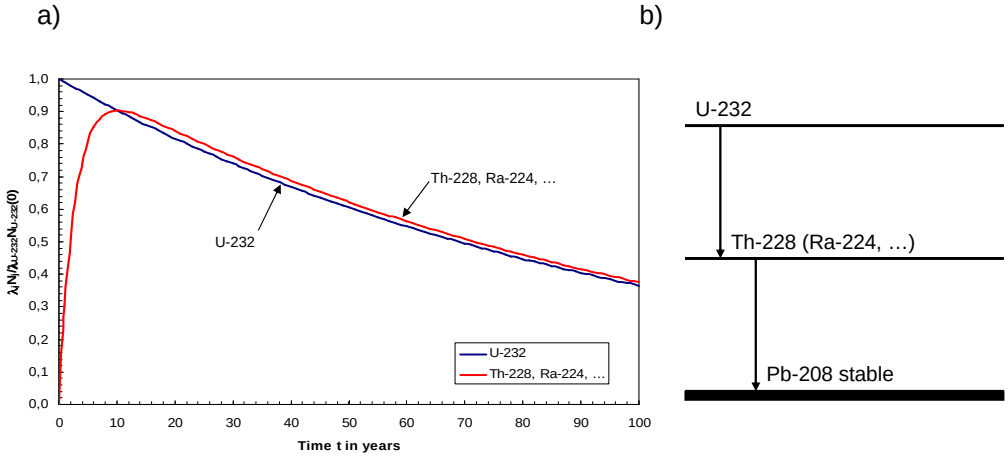

Figure 4.10: a) The ratios of the activities of U-232 and its daughter nuclides is plotted against the time t in years. b) Simplified 2-level decay scheme of the U-232 radioactive series.

The γ-lines from the radionuclides are also taken from the *Evaluated Nuclear Structure Data File*[26] like the γ-lines of the radionuclides of the U-238 radioactive series (see section 4.1). From the discrete γ-energy spectrum, it is shown, that some γ-photons deliver a higher contribution to the effective dose rate than other γ-photons. In particular, the 2.6147 MeV line from Tl-208 adds a large contribution to the effective dose rate because it has high energy and intensity.

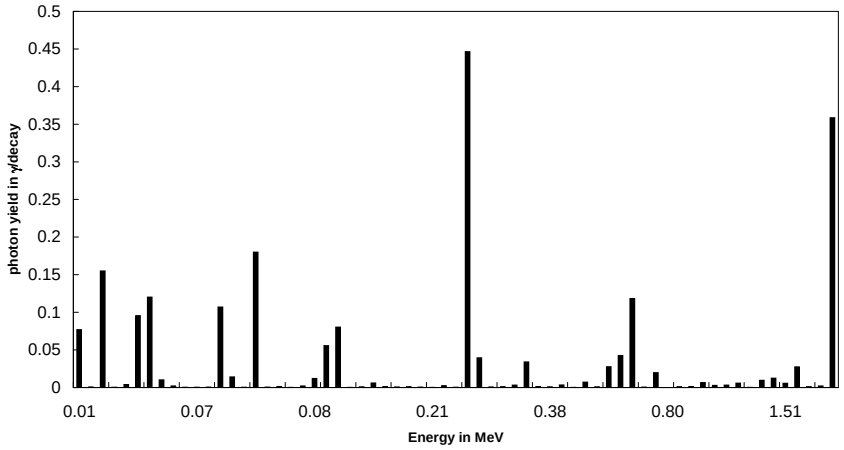

Figure 4.11: Discrete γ-energy spectrum of the radionuclides U-232, Th-228, Ra-224, Rn-220, Po-216, Pb-212, Bi-212 and Tl-208. The photon yield which is a measure for the number of γ-photons per decay is plotted against the energy of the γ-photons.

4.5 Neutron radiation

In the following section the neutron source energy spectrum of UF_6 is presented. As mentioned above, the neutron radiation occurs from spontaneous fission of U-238 and the (α,n)-reaction between the α-particles from uranium isotopes plus the daughters from U-232 and the fluorine cores. In the literature there resides no neutron energy spectrum of UF_6 because the neutron yield in the UF_6 is probably too low to measure a uncollided neutron energy spectrum for a small sample [28].
Since no direct information for the neutron energy spectrum of UF_6 are available, the determination of the energy spectrum which will be used in the MCNP-calculations must be identified indirectly on the basis of conservative assumptions. For this purpose the indirect informations are divided into three categories:
(1) fundamental knowledge on the $^{19}F(\alpha,n)^{22}Na$-reaction, (2) experimentally determined $^{19}F(\alpha,n)^{22}Na$ emission spectra with alternative α emitters instead of uranium and (3) information about fission spectra which are approximately similar to the fission spectra of U-238.
From the fundamental knowledge of the $^{19}F(\alpha,n)^{22}Na$-reaction, it is known, that the "Q-value" (see equation 3.19) is negative (Q = -1.9505 MeV [29]), so that the reaction is endothermal. This means that the maximum neutron energy from this reaction is the energy of the α-particle minus the Q-value. From [28] it arises that the maximum neutron energy of the (α,n)-reaction in UF_6 from natural uranium occurs from the U-234 nuclide and has a value of 4.76 MeV - 1.95 MeV = 2.81 MeV. In other literature

the maximum neutron energy of the (α,n)-reaction is different than 2.81 MeV. So, in [30] the maximum neutron energy has a value at 2.1 MeV and in [31] at 2.35 MeV for uranium. In summary, the neutron energy of the (α,n)-reaction in UF_6 can be expected between 0 and approximately 2.5 ± 0.31 MeV.

The shape and also the probabilities of the various neutron energies in an UF_6 system can be evaluated with the aid of category (2). Here Am-241 is used as an α-emitter instead of natural uranium and the hexafluorine environment of UF_6 has been replaced by a CaF_2 environment [32, 33]. The experimental determination of the neutron energy spectrum of this experimental setup has shown, that there is a maximum between 1 and 2 MeV neutron energy and has a width of about 1 MeV. Since Am-241 has an α-energy of 5.48 MeV which is 0.7 MeV higher than that of U-234, the results of the neutron energy spectrum of the Am/CaF-system can not be directly translated to the UF_6 system. But it can be assumed as an approximation and a good overview about a neutron energy spectrum of the (α,n)-reaction.

After the $^{19}F(\alpha,n)^{22}Na$-reaction for similar UF_6 systems was discussed, the fission spectra are described which could be similar to those of U-238. The best known and most powerful fission spectrum is that of Cf-252 (californium) [31, 32, 33] (see figure 4.12). Comparing this fission spectrum with other well-known fission spectra, differences in the shape or intensity of the spectra can be hardly shown. They are minimally shifted to lower or higher energies. Therefore the fission spectrum of Cf-252 is a very good approximation for the U-238 fission spectrum.

With the aid of these considerations an appropriate neutron energy spectrum must be now determined for the contribution of neutron radiation. The spectrum shall have neutrons with the maximum energy of about 2.5 ± 0.31 MeV from the (α,n)-reaction and must be have a maximum between 1 to 2 MeV. Furthermore the fission spectrum of Cf-252 must be considered. From these considerations two assumptions are popular for the overall neutron energy spectrum:

1. the overall spectrum is monoenergetic with a neutron energy of 1 meV
2. the overall spectrum is a Watt fission spectrum of Cf-252.

The first assumption simplify the whole problem with the neutron energy spectrum because all neutrons have the same energy of 1 MeV and can be therefore only used as an contestable approximation. Differently the second assumption which allows all kinds of neutron energies up to a maximal neutron energy and with different

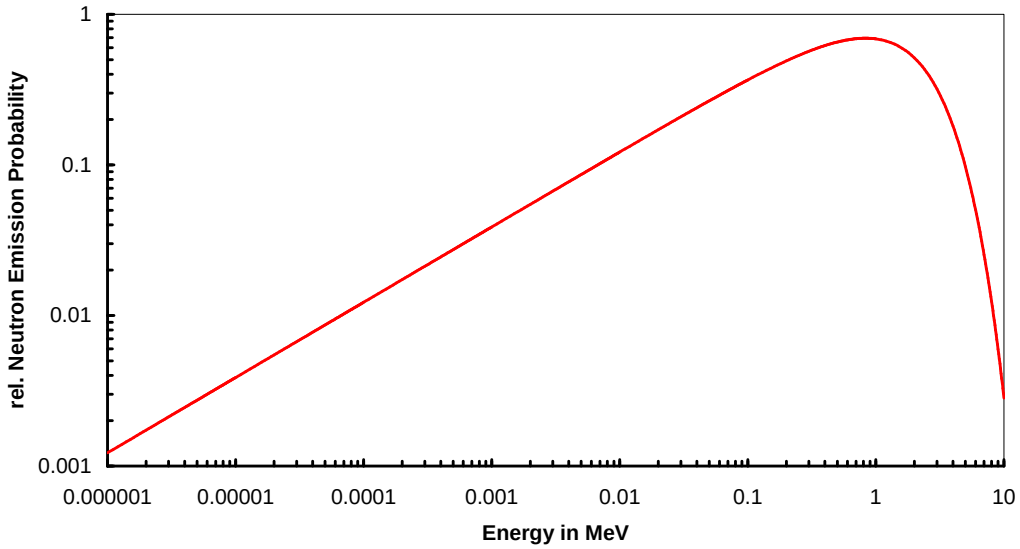

Figure 4.12: Plot of the Watt fission spectrum of ^{252}Cf. The emission probability of the neutrons is plotted double logarithmical dependency on the neutron energy in MeV.

intensity distributions. Based on the previously established considerations, it seems more appropriate to use the Watt fission spectrum of Cf-252 for the overall neutron energy spectrum. This is confirmed by comparative calculations by Freek Keijzer [28]. The Watt fission spectrum of Cf-252 delivers more conservative assumptions than the spectrum with monoenergetic neutrons.
For these reasons, the whole neutron radiation which is emitted from the UF_6 cylinders can be explained with the aid of a Watt fission spectrum of Cf-252. The Watt fission spectrum is notionally defined by

$$p(E) = C \cdot exp\,(-a \cdot E) \cdot sinh\left[\sqrt{(b \cdot E)}\right] \tag{4.8}$$

with $p(E)$ as the emission probability of neutrons with the energy E, C as a normalization constant and a and b as for the Watt fission spectrum of Cf-252 necessary values (a=1.025 and b=2.926 [34]).

Chapter 5

Monte Carlo N-Particle studies

In the following chapter the numerical calculations of the effective rate in different distances of 48Y and 30B UF_6 cylinders will be investigated with the simulation program: *Monte Carlo N-particle* (MCNP). Furthermore, the dose equivalent rate of the so called Product-Store (PL-2) is investigated at different receiving points. The Product-Store stores the individual Product cylinders, so that it is interesting in radiation protection to calculate the effective dose rate in and around the building.

5.1 Monte Carlo N-particle (MCNP)

MCNP is a general-purpose Monte Carlo radiation transport code to modeling the interaction of photons, electrons and neutrons or coupled neutron/photon/electron with any matter [34]. In MCNP all important physical processes are included, which are significant for the transport of radiation in matter. In the following calculations, only the neutron- and photon-transport are used, since the bremsstrahlung which is usually caused by the interaction of electrons with matter has been replaced by an alternative bremsstrahlung spectrum (see section 4.2). So, only the physical interactions of neutrons and photons is explained.

The different types of neutron interactions with the surrounding matter are:

- inelastic scattering
- elastic scattering
- neutron capture
- (n,x)-reaction

- photon production
- fission

and the interaction of photons with the sourronding matter:

- incoheret (Compton) scattering
- coherent (Thomson) scattering
- photoelectric effect
- pair production
- photonuclear physics (giant dipole resonance, quasi-deuteron)

The interaction of photons and neutrons are described by physical rules and transport data to determine the occurrence of an interaction with the material. By defining these interactions of photons and neutrons, the energy, position and direction of flight for the particle can be assigned at any time. The required cross sections of materials for these interactions exist in continuous-energy nuclear and atomic data libraries in MCNP. Most of these data libraries (*Evaluated Nuclear Data File* (ENDF) *system*[26], *Advanced Computational Technology Initiative* (ACTI)[35], the *Evaluated Nuclear Data Library* (ENDL)[36], *Evaluated Photon Data Library* (EPDL)[37], the *Activation Library* (ACTL)[38], the *Lawrence Livermore National Laboratory* (LLNL)[39] and the *Los Alamos National Laboratory* (LANL)[40]) are publicly available.

MCNP is based on Monte-Carlo simulations, which was first drawn into contemplative by Enrico Fermi in 1930. 1946 this method was then used by Stanislaw Ulam and John von Neumann to support the secret "Manhattan Project" at the Los Alamos Scientific Laboratory. The Monte-Carlo simulation is a stochastic method. With the aid of many individual probabilistic events which are simulated sequently, non-analytical solvable problems like physical and mathematical systems with many coupled degrees of freedom can be solved numerically. The probability distributions which describe these individual probabilistic events are statistically sampled, so that the total phenomenon of this events are described exactly. Statistical sampling processes are based on the selection of random numbers. In one event log (history) all necessary information of a particle and its secondary particles from source throughout its life to its death are available due to the transport data and physical rules. To

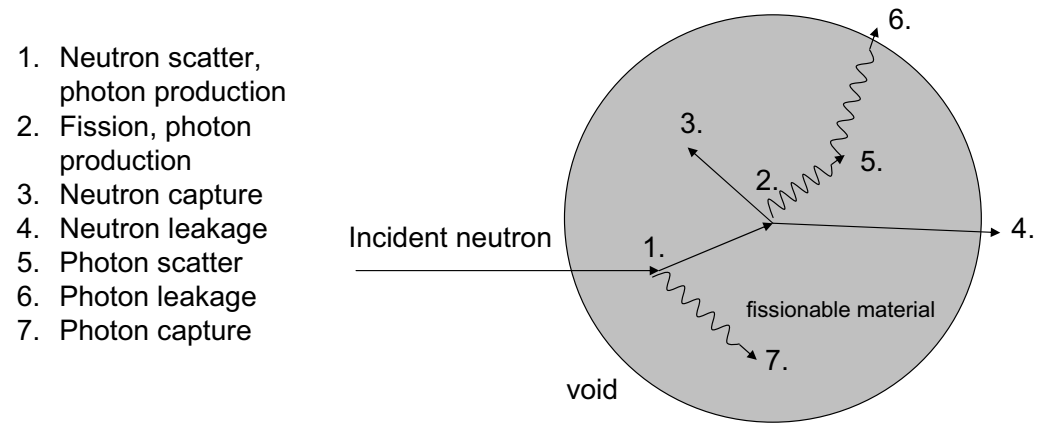

Figure 5.1: Example of an individual probabilistic event log in MCNP. A source neutron comes from a void area into an area with fissionable material. All possible physical interactions can occur in this area and the information of each step of its life is determined by transport data and physical rules.

get an accurate result for the underlying problem, many histories are needed. For example, the interactions of a neutron in a history is described in figure 5.1.

An incident neutron comes from a void area into a fissionable area and scatter at interaction point (event) 1 in the shown direction. A photon is produced too at this point and is banked in MCNP for later analysis. At event 2, the incoming neutron is terminated and two outgoing neutrons and one photon are produced due to fission at this point. One neutron and the photon are banked. The remaining neutron from the fission is destroyed now at event 3. Now the banked second neutron from the fission is considered again. This leaves the fissionable material at event 4. The banked photon, which was produced at event 2 scatters at event 5 and leaves the fissionable material at event 6. The photon generated at event 1 is considered now by MCNP. It makes no further interaction, but is terminated at event 7. The history from the incident neutron is now complete. Note, that MCNP retrieves banked particles, so that no information gets lost. The more incoming particles or histories are considered of a problem, the merrier the statements can be analysed about the particle distribution and the results.

In order to solve a complex problem with MCNP, it requires the entire 3D-geometry of the problem, information about the materials and details of the radiation source particles. All these information are written in the so-called *main input cards* of the Input-file. There are three different main input cards to describe a problem accurately.

1. Cell Card

2. Surface Card

3. Data Card

In the surface card, all surfaces are described which are necessary for the problem. With the aid of analytical surface equations, the surfaces for different geometries can be determined. In order to describe not always the complete analytic surface equation in MCNP, the equations are abbreviated with a mnemonic and following parameters for the surface. Table 5.1 gives a brief overview of some selected surfaces.

Mnemonic	Type	Description	Equation	Parameter
P	Plane	general	$Ax + By + Cz - D = 0$	$A\ B\ C\ D$
S	Sphere	centered on y axis	$x^2 + (y - \bar{y})^2 + z^2 - R^2 = 0$	R
C/X	cylinder	parallel to x-axis	$(y - \bar{y})^2 + (z - \bar{z})^2 - R^2 = 0$	$\bar{y}\ \bar{y}\ R$
CX	cylinder	on x-axis	$y^2 + z^2 - R^2 = 0$	R

Table 5.1: Overview of some surfaces which can be used in MCNP by including the mnemonic and the parameters in the surface card.

After the surfaces are defined in the surface card, the cells can be determined by the surfaces at the cell card. Each cell receives a cell number, a material and a density, so that the interactions of the radiation particles are defined by the cross section of the material in the allocated cell.
The complete geometry is now defined by the surface and cell card. The data card specify the source definition and type of radiation particles for a MCNP problem. Thus, a given energy spectrum for the radiation particles can be determined. Variance reduction techniques can further be defined in the data card which improve the statistical results.
When all necessary information are specified in the three main input cards, the simulation can be started. After running the entire simulation, all results and information can be extracted from the Output-file. For further reading of the creation of an Input-file see the MCNP manual [34].

5.2 Dose conversion coefficients

To calculate the effective dose rate of a person in a given problem, one or several detectors (tallies) must be placed on the observed position in the MCNP Input-file. Therefore, MCNP provides different types of tallies, for example a tally over the averaged flux over a surface or a cell or a tally over a flux at a point or ring detector. All these tallis can specify the flux in two different measurement units: 1. $particles/cm^2$

and 2. MeV/cm^2. There are further tally types in MCNP like tallies for the energy deposition or for fission energy deposition averaged over a cell [34]. These tallis are not important in the following problems yet.
Since the measurement unit of the effective dose rate is Sv/h (see 3.1.3), the tallies in MCNP must be modified by *dose conversion coefficients* to get the right measurement unit for the tally in the output after MCNP run. The dose conversion coefficients are different for photon, neutron and electron radiation because every radiation has different radiation and tissues weighting factors which must be considered for the effective dose rate. The dose conversion coefficients have the measurement unit of $Sv \cdot cm^2/particles$ and are therefore perfect to modify the tally by multiplication of the tally with the dose conversion coefficients. By a further multiplication of the tally with a time-normalization factor of $3600 s/h$ and the activity of the considered problem in MCNP (for example the activity of a full UF_6 cylinder), the effective dose rate is received (see equation 5.1).

$$\frac{particles}{cm^2} \cdot \frac{Sv \cdot cm^2}{particles} \cdot 3600 \frac{s}{h} \cdot \frac{1}{s} = \frac{Sv}{h} \tag{5.1}$$

The dose conversion coefficients were listed in 1996 by the publication ICRP 74 [41], by evaluating the scientific works on this topic [42, 43, 44]. To determine the dose conversion coefficients for photon and neutron radiation, a analytically defined phantom of a human body is needed that contains all organs and tissues of a human body. Since it is very difficult to produce either a mathematically or physically precisely human body, it must be approximated. The *Medical International Radiation Dose (MIRD) Comittee* phantom (see figure 5.2) is a heterogeneous mathematical representation of the human body [45, 46] which incorporates different densities for the various body tissues. Therefore, the MIRD-phantom is a good approximation of a human body and can be used to determine the dose conversion coefficients.

Due to the fact that the organs and tissues are located in different depths in the phantom, depending on the view of the phantom, different dose conversion coefficients are availabled for each incoming beaming direction. Therefore, the dose conversion coefficients were determined as a function of the radiation energy for various incoming beaming directions and are presented in figure 5.3 and 5.4 for photons and neutrons. The dose conversion coefficients are modified in such a way, that only the results from the tallies in MCNP and the activity of the radiation component must be multiplied to obtain the effective dose rate.

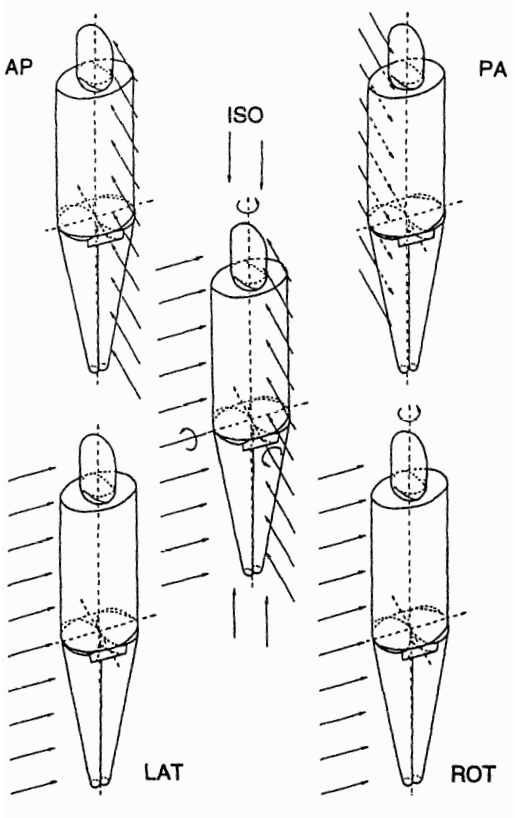

Figure 5.2: Some irradiation geometries of an anthropomorphic phantom [41]. The shortcut next to the phantoms are: antero-posterior (AP), isotropic (ISO), postero-anterior (PA), lateral (LAT) and rotational (ROT). The arrows indicate the incoming beam direction.

The energy dependence of the dose conversion coefficients of photons for the effective dose rate is determined to take several parameters into account, such as the total photon cross sections in the different tissues and organs, the location and tissue weighting factors of the individual organs in the body and the irradiation geometry. Figure 5.3 shows clearly, that the shape of the different irradiation geometries disagree strongly in the energy range between 10 keV and 100 keV. After 100 keV the dose conversion factors of all irradiation geometries increase nearly linear in the

double logarithmic plot because the pair-production cross section increase slowly with photon energy for low atomic numbers which are typical for tissue and organs. The discrepancies between the irradiation geometries in the energy range of 10 keV and 100 keV are due to the fact, that the Compton scattering have different cross sections for the different organs and tissues in body, the variuos location of the organs in the body with respect to the incoming photon beam and the different tissue weighting factors for the organs.

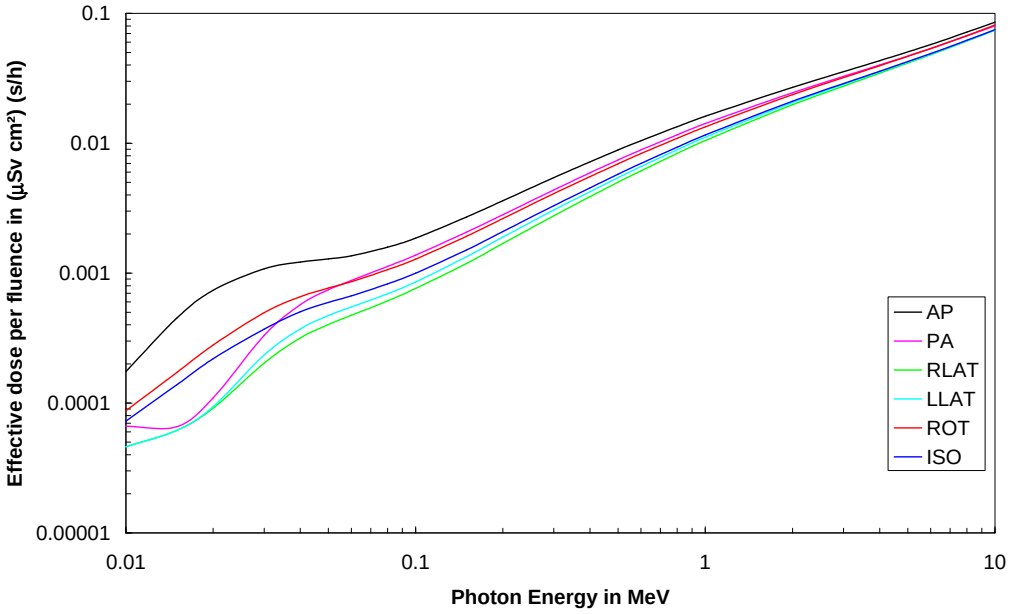

Figure 5.3: Dose conversion coefficients for effective dose as a function of energy for photons in various irradiation geometries on an adult anthropomorphic computational models [41]. LLAT stands for left lateral and RLAT for right lateral.

The dependence of the dose conversion coefficients of neutron energy is also determined by the depth of the organ in the body, the tissue weighting factors and the total cross section for the neutron energies. The shape of the different irradiation geometries are similarly the same (see figure 5.4). In the energy range from thermal neutron energies and 1 eV is a slight increase of the dose conversion coefficients. From 1 eV to 10 keV the dose conversion coefficients are nearly independent of the neutron energy. In the energy range of 10 keV and about 1 MeV the dose conversion coefficients sharply increase with neutron energy due to proton recoil and other charged secondary particles interactions from neutrons [41].

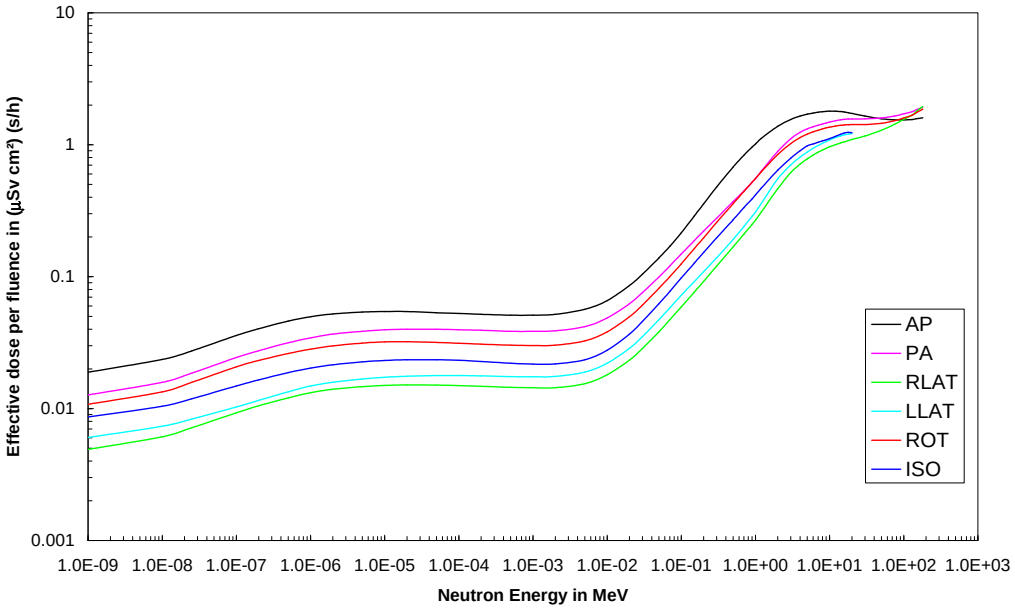

Figure 5.4: Dose conversion coefficients for effective dose as a function of energy for neutronsin various irradiation geometries on adult anthropomorphic computational models [41]. LLAT stands for left lateral and RLAT for right lateral.

By considering the dose conversion coefficients of photon and neutron radiation at different irradiation geometries, it is clearly seen, that the dose conversion coefficients are significantly higher for several irradiation geometries, as in other ones. So for example, the dose conversion coefficients for the AP irradiation geometry is always much higher than the dose conversion coefficients for RLAT. This is because these organs with a large weighting factor are anteriorly located and are more at the surface of the body than the location of the organs from the RLAT view which appears more or less "deep-lying" from this aspect. Based on these observations, the dose conversion coefficients from AP irradiation geometry are taken for further MCNP-calculations, since these provide the highest values and by work with radioactive materials it is common that the person is rather turning towards the radiation source.

5.3 Verification of calculations by measurements

In this section, the theoretical MCNP-calculations of a feed-cylinder are verified with real measurements. The verifictaion of the numerical MCNP-calcultaions with real measurements are very important to prove the accuracy of the simulation. It is of a high relevance to make the simulation in MCNP as realistic as possible. Often it is difficult to simulate the reality par for par. Therefore, these differences must be considered in the subsequent discussion of the results.
First, the measuring equipment are presented which are used for the determination of γ- and neutron-ambient dose rate. After that, the results of measurements and calculations are presented and discussed.

5.3.1 Measuring equipments

Measuring equipment for γ-radiation

For the following measurements of γ-ambient dose rate, the radiameter "*FH 40 G-10L*" of the company "*Thermo Fisher Scientific*" is used (see figure 5.5).

Figure 5.5: Figure of the radiameter FH 40 G-10L, which measures the γ-ambient dose rate (adopted from [47]).

To measure the incoming radiation, the *FH 40 G-10L* has a proportional counter in the head of the box. A propotional counter is a gas-detector and the buildup exist in the simpled form of a both sides sealed cylindrical metal tube (cathode) and a thin conductor (anode) in the middle and is led through one surface of the metal tube by an isolator (normally glass). This detector is dedicated for γ-radiation because it can penetrate the thin layer of the metal tube. If a γ-photon penetrates

the metal layer, the atoms of the gas will be ionizied due to the photo-effect and compton scattering and free electrons and cations are accelerated to the anode or cathode by connected voltage. An electrical charge is induced at the contacts of the electrodes and a voltage pulse is converted by a changing blocking capacitor and a charge-sensitive preamplifier. The voltage pulse can either be counted or analyzed by its pulse height. From the voltage pulses, the dose rate is calculated by a complete computing system. The *FH 40 G-10L* measures the *ambient dose rate* $\dot{H}^*(10)$ in a measuring area from the natural background radiation of about 100 nSv/h to a high flyer of 1 Sv/h, but the official calibration area goes only from 0.5 μSv/h to 100 mSv/h, so that the measurements below or over this area must be paid with sufficient care and the standard deviation of the measurement result must be specified. The energy area for the γ-photons which can be detected by the *FH 40 G-10L* is between 30 keV and 4.4 MeV [48]. By comparing the energy area of the *FH 40 G-10L* with the energy area of the γ-photons which are produced by the decay of the different uranium isotopes and the subsequent daughter nuclides (see figures 4.3, 4.5, 4.8 and 4.11), there are also some γ-lines which are below 30 keV. γ-photons which are in the area between 10 keV and 30 keV can not be detected by the *FH 40 G-10L*. In aspect to the ambient dose rate it is not such a big problem because the γ-photons in the area between 10 keV and 30 keV are mostly absorbed by the UF_6 themself or the steel wall of the cylinder and do not have a big influence to the ambient dose rate outside the cylinder. The highest γ-line from UF_6 is the 2.615 MeV line of Tl-208. So, there is no problem for the *FH 40 G-10L* to detect the highest γ-lines of UF_6.
To determine the ambient dose rate exactly, it is important, that the detector has a good responsivity over a wight angle to the main incident angle. The responsivity in an angle area of $\pm 75°$ is more than 80%, so that good results can be measured in this angle area. The *FH 40 G-10L* is callibrated with the 662 keV γ-line of the radionuclide Cs-137 (caesium).
The relative standard deviation of the *FH 40 G-10L*, which is a measure for the statistical error is defined by the general equation:

$$\sigma_{rel} = \frac{1}{\sqrt{\text{number of pulses}}} \tag{5.2}$$

and the operational error limit of the *FH 40 G-10L* is $\pm 24\%$.

Measuring equipment for neutron-radiation

To determine the neutron dose rate, which is independent on the energetic composition of the neutron field, the *intelligent neutron detector FHT 751 (Biorem)* (see

figure 5.6) of the company *Thermo Fisher Scientific* is used. It also measures the ambient dose rate $\dot{H}^*(10)$.

Figure 5.6: Figure of the intelligent neutron detector FHT (Biorem), which measures the neutron-ambient dose rate.

The *Biorem FHT 751* is organized as follows. It consists of a cylindrical iron case with a diameter of 208 mm and a height of 395 mm. Within the iron case is a cylindrical moderator, which consists of polyethylene-discs and -cylinders. An axial bore in the middle of the *Biorem FHT 751* includes the cylindrical proportional counter tube with a diameter of 26 mm and a height of 224 mm. The proportional counter tube is filled with BF_3-gas [49].
Due to the existing of the light atoms hydrogen and carbon in polyethylene, incident neutrons are moderated by elastic scattering with them, so that they have a low kinetic energy of less than 0.1 eV after scattering. To detect this thermal neutrons the gas BF_3 in the proportinal counter tube is suited because it undergoes with the thermal neutrons the exothermic nuclear reaction $^{10}B(n,\alpha)^7Li$. The resulting ions (α-particle and lithium nuclide) lead to ionization and thus to a measureing of a voltage pulse. From the voltage pulses, the dose rate is calculated by a complete computing system, like it was the case by the *FH 40 G-10L*, too. With *Biorem FHT 751*, the complete spectrum of neutrons can be detected because they are moderated in such a way, that they enter the proportional counter tube as thermal neutrons. Moreover, it is calibrated to the nuclide Cf-252, which is used in subsequent calculations as the neutron source of the UF_6 cylinders and the energy dependence is based on ICRP

21, which is similar to the energy dependence of ICRP 74. The angular acceptance range of *Biorem FHT 751* is shown in figure 5.7. It clearly shows, that it has a good angular acceptance range of $-45° \leq \Phi \leq +45°$, so that neutrons can be detected with various incident angles. The relative standard deviation is defined by equation 5.2, too and the operational error limit for the *Biorem FHT 751* is $\pm 20\%$.

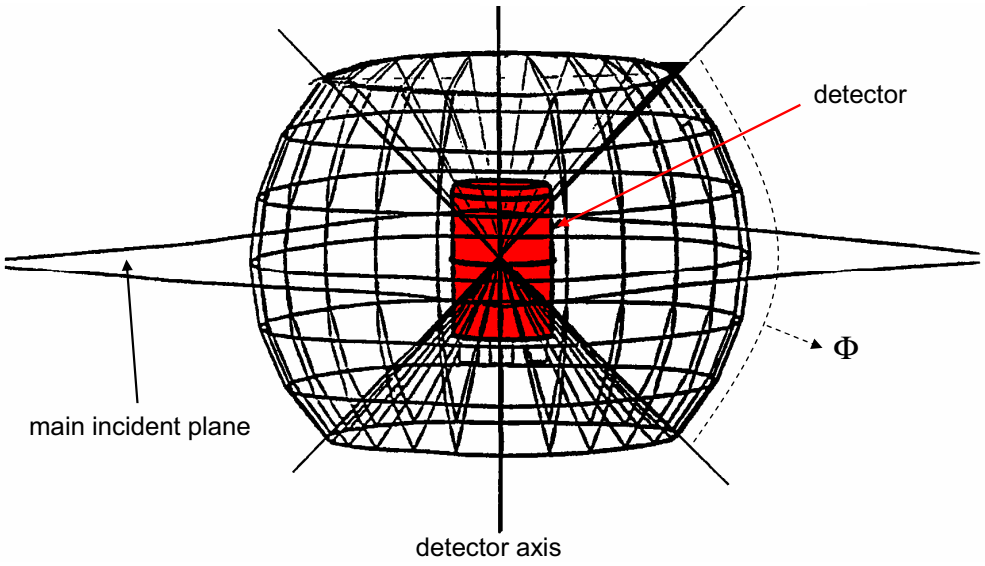

Figure 5.7: Scheme of the angular acceptance range of the *Biorem FHT 751*. The main acceptance range is in the angular area of $-45° \leq \Phi \leq +45°$, so it is beneficial to place the detector perpendicular to the incident direction of the neutrons (adopted from [49]).

5.3.2 Experimental setup

In this section the experimental setup is explained in order to determine a measured ambient dose rate of a 48Y Clean Feed UF_6 cylinder. The experimental setup is shown in figure 5.8.

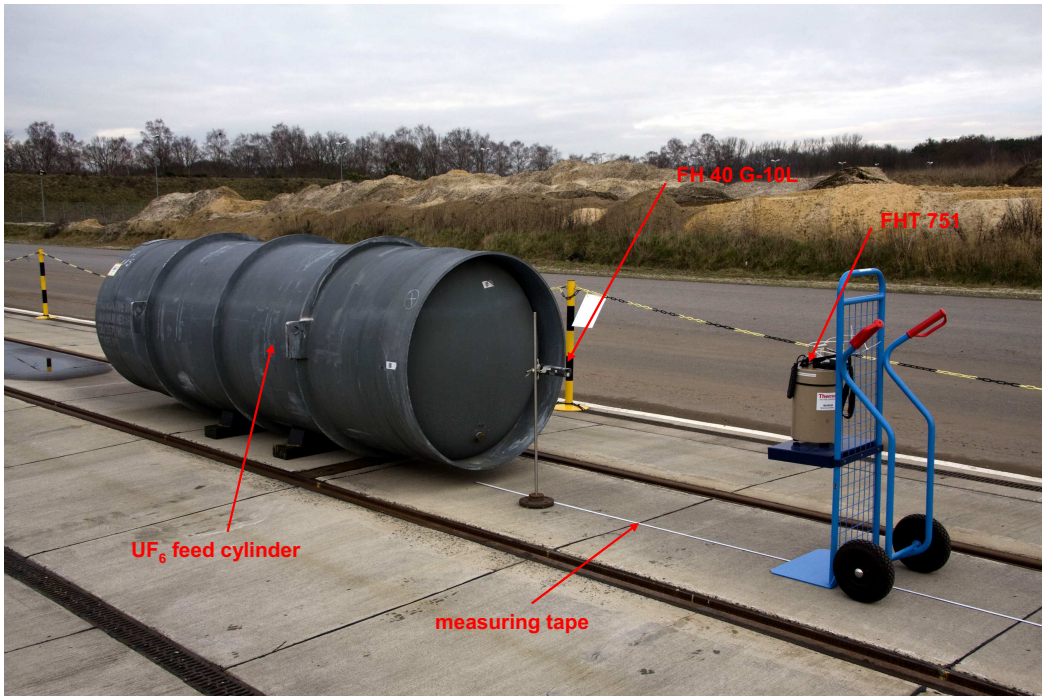

Figure 5.8: Experimental setup to determine the ambient dose rate of a 48Y Clean Feed cylinder.

A 48Y-UF_6 cylinder is used, which is filled with 12.500 kg Clean-feed. It is placed on two hard-gum sockets to ensure safe storage of the cylinder. The deepest point of the cylinder is positioned in a height of 10 cm to the concrete floor. Since the ambient dose rate is both measured from the side of the cylinder and from the head end, a measuring tape is placed on the concrete floor, where the start of the measuring tape is consistent with the outermost point of the cylinder. This could not be done exactly because the outermost point of the cylinder is in a height of about 70 cm and the measuring tape is placed on the concrete floor. In addition to this, there is a blanket on the head end of the cylinder, so that it is hard to place the measuring tape exactly to the outermost point of the cylinder. Therefore an error with a value of ± 3 cm in the distance must be accepted.
The *FH 40 G-10L* is fixed with a clamp on a rack (see figure 5.8) at a height of 70.96 cm because the outer diameter of the 48Y-UF_6 cylinder is 121.92 cm. This

corresponds exactly to the outermost point and the middle height of the cylinder, when it is on the hard-gum sockets. Using this measurement rack, the exact height of the *FH 40 G-10L* to the cylinder can be achieved. By a prior adjustment of *FH 40 G-10L* with the socket of the rack the distance to the cylinder could be determined, when the end of the socket is placed at the desired position on the measuring tape because this correspond with the distance of the *FH 40 G-10L* to the cylinder wall. However, a measuring error of ±1 cm must be accepted due to the unevenness of the concrete floor.

Neutron ambient dose rate is measured with the *Biorem FHT 751*. Due to the fact, that the *Biorem FHT 751* has large dimensions, it is essential to place the detector on a correct rack to get right values in ambient dose rate. Hence the detector is placed at the end of a table which is fixed at a hand truck (see figure 5.8). The table at the hand truck has the same dimensions than the depositing rack of the hand truck. Thus the distance of the detector to the cylinder can be determined by placing the end of the depositing rack at the desired place, where to measure. It must be taken into account, that the counter tube of the *Biorem FHT 751* is not at the end of the detector and thus not at the end of the table, but in the center of the detector. Therefore, the position of the detector is corrected by 10 cm at each new distance in direction to cylinder. Nevertheless a measurement error of ±2 cm must be accepted due to the uncertainty of the large dimensions of the *Biorem FHT 751*.

Overall, the measuring error in distance for the measuring values of the γ-ambient dose rate are specified by ±4 cm and for the neutron-ambient dose rate a measurement error in distance of ±5 cm. By γ-measurement 400 pulses per measurement are recorded, so that it gives a relative standard deviation of 5% (according to equation 5.2). Unlike the γ-measurement, the neutron-measurement could not achieved 400 pulses in an acceptable time frame because there are only a few pulses in a given time interval. Hence, a measurement time of 10 minutes is attached per distance point and the relative standrad deviation at a given ambient dose rate is read out from a diagram of the manual of the *Biorem FHT 751*.

Previous to the main measurements, the ambient dose rate of neutron- and γ-radiation is measured. The whole experimental setup is arranged in a separated temporary control area.

5.3.3 Results of measurement

The results of the ambinet dose measurement of a 48Y Feed UF_6 cylinder are presented in figure 5.9 for the γ-ambient dose rate and in figure 5.10 for the neutron-ambient dose rate. The ambient dose rate which occurs from background radiation is already detached from the measuremnt values in the plots. For γ-background radiation, there is an ambient dose rate of about 0.123 $\mu Sv/h$ and for neutron-background radiation an ambient dose rate of about 0.0247 $\mu Sv/h$. The cylinder has a storage period of about 12 months after refilling. This must be considered in the subsequent MCNP-calculations, since the activity of the daughter nuclides from U-238 are already fully developed and in U-232 the activity has ca. 30% of the activity of U-232, according to equations 4.1 and 4.6.

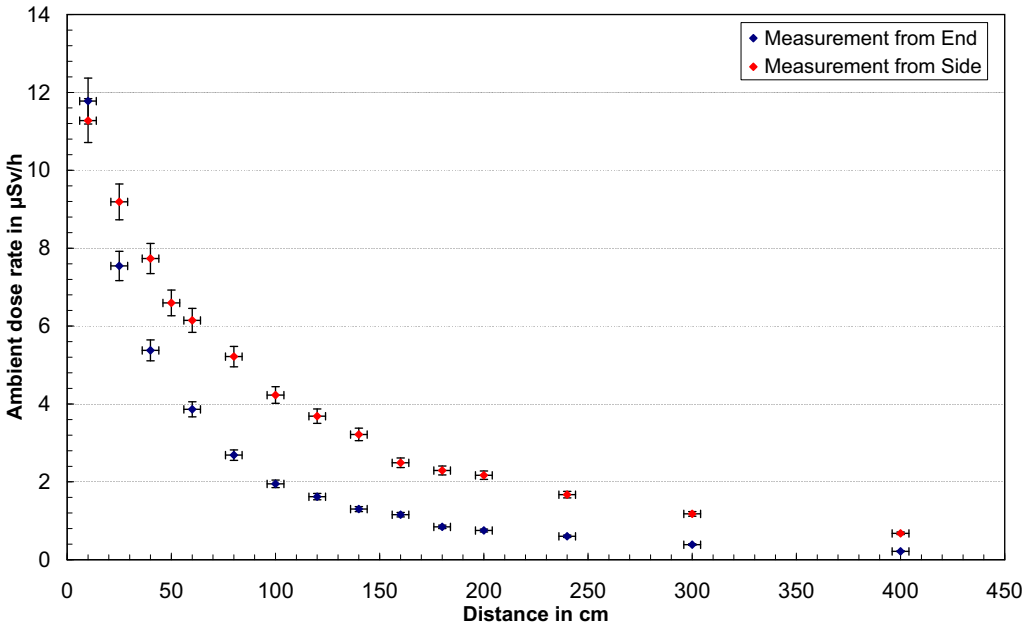

Figure 5.9: Measuring results of the γ-ambient dose rate of a full 48Y Clean Feed UF_6 cylinder. The ambinet dose rate is plotted against the distance to the outermost point of the cylinder wall at end and side. Blue markers are the measuring values from the head end and red markers from the side of the cylinder. The error bars are given by the relative standard deviation of the individual measurement points, which are below 5%. In face of the standard deviation the measuring values of the calibrated *FH 40 G-10L* have an operational error limit of 24% [48].

The measured values of γ-ambinet dose rate are plotted against the distance of the cylinder. Both the measurement values from the side and from the end have a significant decreasing trend with increasing distance to the cylinder. This is also expected before the measurements are done because the radiation is attenuated due

to the interaction with the surrounding material and the more material between the radiation source and the detector is, the greater is the attenuation and this leads consequently to a reduction of the γ-ambient dose rate.
It is also clearly seen, that the γ-ambient dose rate is higher at the side than at the end of the cylinder. This is assumedly the case because from the perspective of the detector a large area of individual radioactive sources is appreciated from the side than from the end due to the diferent geometry and dimensions of the cylinder at side and end. Hence, more photons are registered at the side of the cylinder which automatically increase the ambient dose rate. A distinction of this description could be detected at a distance of 10 cm. Here, the ambient dose rate at the end of the cylinder is slightly higher than those on the side. The following reason could possible explain this difference. If the detector is close to cylinder wall, whether on the side or end, the cylinder wall looks like an infinitely curved high wall. This is partly because the response of the detector is $\pm 75°$. But the radius of the surface of the UF_6 cylinder is at the end greater than the radius at side. This means that at the end of the cylinder, the radioactive sources are closer to the detector than at the side and consequently a higher ambient dose rate is measured. This effect is maybe an error of the measurement equipment due to the angle dependenced response.

For neutron measurement only selected distances are measured to determine the shape of the ambient dose rate with increasing distance because only a spot of neutrons are registered by the detector due to the small neutron-activity. As already described above, 400 pulses per measurement value could not be proven, so that the relative standard deviation is specified as the maximum deviation of 15% after the specification of the *physical technical federal agency* (PTB). Overall, 10 min measuring time are appointed for every measrement point. The measurement values are presented in figure 5.10.

Similar to the measurement of γ-ambient dose rate, the neutron-ambient dose rate is at the side of the cylinder higher than at end. This can be also explained by the above described statement. The measurement values of the neutron-ambient dose rate is decreasing with increasing distance, too.
In context of this master thesis, a not sufficient number of measurements of the neutron-ambient dose rate are performed, so that precise statements about the effect of the geometry and dimensions of the cylinder on the neutron-ambient dose rate must be relinguished. Therefore, it is necessary to refer these statements to the following theoretical calculations.

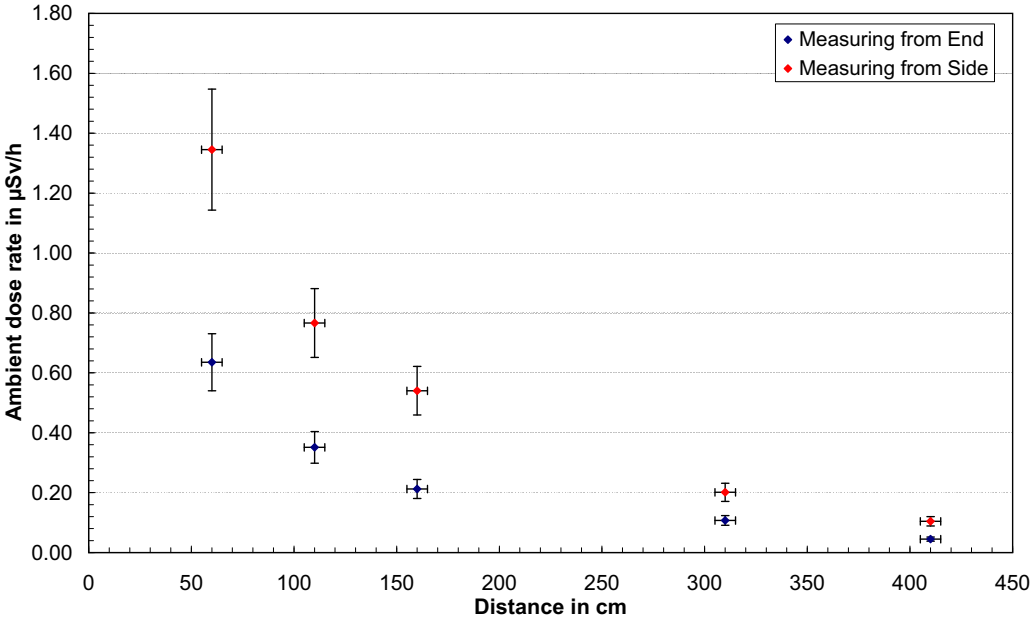

Figure 5.10: Measuring results of the neutron-ambient dose rate of a full 48Y Clean Feed UF_6 cylinder. The ambinet dose rate is plotted against the distance to the outermost point of the cylinderwall at end and side. Blue markers are the measuring values from the head end and red markers from the side of the cylinder. For the relative standrad deviation, the maximal value of 15% is taken after PTB for a calibrated detector [49].

5.3.4 Comparison between measurements and calculations

In the following subsection, the measured values are compared with theoretical calculations by using MCNP. Therefore, four different cylinder geometries are presented, which are used in MCNP (see figure 5.11). This representation of the different geometries shows the effect of the ambient dose rate in later results of the theoretical MCNP-calculations.

1. cylinder with flat ends, homogeneous filled with UF_6
2. cylinder with round ends, homogeneous filled with UF_6
3. cylinder with round ends, UF_6 ring-shaped on the side of cylinder wall
4. cylinder with round ends, UF_6 ring-shaped on cylinder wall

In the first geometry, a mathematical cylinder with flat top parts at each end is modeled. In addition, the UF_6 and its daughter nuclides are homogeneous distributed in the entire cylinder. The density ($\rho = 3.0925\ g/cm^3$) is adjusted to achieve a total mass of 12.500 kg.

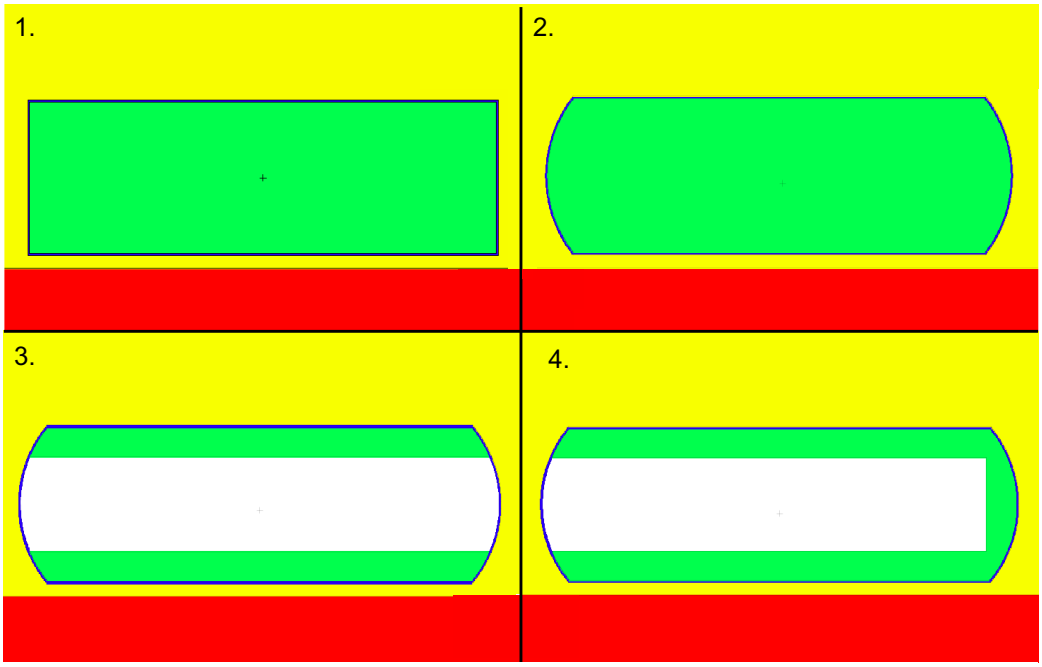

Figure 5.11: MCNP illustration of the two cylinder geometries in the x-z-plane. They are 10 cm above the concrete floor (red area) and in an environment of dry air (yellow area). The iron wall is blue illustrated. 1. Simplified geometry of an UF_6 cylinder with flat ends. The UF_6 (green) is homogeneous distributed and the density is minimised to $\rho = 3.0925\ g/cm^3$, so that 12.500 kg UF_6 are into the cylinder. 2. Cylinder with round ends. UF_6 is homogeneous distributed in the whole cylinder and has a density of $\rho = 3.23124\ g/cm^3$. 3. Cylinder with round ends and UF_6 distributed axial on the inner wall of the cylinder. 4. Complex geometry, which is near the reallity. The density of UF_6 is $\rho = 5.2\ g/cm^3$ and the area of UF_6 is so defined, that 12.500 kg UF_6 are in the cylinder.

The second geometry is different to the first geometry in regard that the ends are not flat but round and thus the geometry of the cylinder exactly correspond to the ANSI of a 48Y-UF_6 cylinder, but without the blankets at the end. The UF_6 is also distributed homogeneously in the cylinder.
In the next geometry (3.), the form of the cylinder is the same as from the second geometry, but the UF_6 has a different distribution as in the second geometry. Here, the 12.500 t of UF_6 are not homogeneously distributed in the cylinder, but ring-shaped around the cylinder wall, due to cooling the cylinder at feeding. Furthermore, the ends are not provided with UF_6. Due to the fact, that the UF_6 is ring-shaped distributed around the cylinder wall, the correct density ($\rho = 5.2\ g/cm^3$) of UF_6 at a temperature of 0°C is assumed, which was the temperature at day of measurements. The fourth cylinder geometry is simulated as realistic as possible and has round ends

like the second and third geometry. Since the cylinder is cooled of about -25°C during the feeding of UF_6, the UF_6 is ranged ring-shaped on the cylinder wall, so that a cavity in the center of the cylinder is located after full feeding of 12.500kg UF_6. At one end of the cylinder is the valve, which is heated during feeding so that the UF_6 is not solidified at the valve opening and the UF_6 will not blocked the passage. Therefore, no UF_6 is simulated in the geometry on the side on which the valve is. Of course, the simulated configuration of the UF_6 in the cylinder corresponds not exactly with the configuration in a real cylinder due to external characteristics, mechnaische voltages and temperature differences. This approximation in the simulation to the reallity must be considered in the discussion of the results of the ambient dose rate. The cavity in the center of the cylinder exist of pure vacuum in the simulation. In reality there is a vapour pressure of UF_6, so that small amounts of UF_6 are in this area. The density of UF_6 near the cylinder wall is the same as the density in the third geometry.
All cylinder geometries are modelled in a distance of 10 cm to the concrete floor and in an environment of dry air with a atomic weight per cent of 76.8% nitrogen and 23.2% oxygen. The atomic weight per cent of the concrete is 15.43% hydrogen, 61% oxygen and 23.56% silicium. The cylinder wall consist of pure iron and the UF_6 in the cylinder have the typical weight per cent to ASTM specifications of natural Feed.

Since the measurement devices only measure the ambient dose rate $\dot{H}^*(10)$ and not the effective dose rate, the dose conversion coefficients of $H^*(10)$ from ICRP 74 [41] must be used in the MCNP Input-files to evaluate the energies of the γ- and neutron-radiation exactly and to get correct results in the MCNP-calculations.
The γ-ambient dose rate results of the MCNP-calculations are presented in figure 5.12 for photons at side and figure 5.14 for photons at end. Here, the ambient dose rates of the individual radiation components (see chapter 4) are already summed up to get the whole ambient dose rate. All in all 15.000.000 source particles for every radiation component are used in the simulation to get a relative standard deviation below 5%. In most cases the relative standard deviaton is still below 1%.
The γ-ambient dose rates of the calculations arise from the MCNP-tally multiplied with the γ-activity of the cylinder. As already described in section 5.2, the MCNP-tally has a unit of $(\mu Sv \cdot s)/(\gamma \cdot h)$. Multiplying the MCNP-tally with the total activity (unit: γ/s) of source photons, the γ-ambient dose rate at the observation point is obtained. Since the cylinder has a storage time of approximately 12 months after feeding, the activity of the daughter nuclides of U-232 is 30.25 % of the total

activity of U-232 itself, according to equation 4.7 and therefore it is necessary to multiply a correction factor of 0.3025 to the activity. The daughter nuclides of U-238 are able to build up fully in this storage time, so that they are in radioactive equilibrium with U-238 and the full activity can be multiplied to the MCNP-tally. U-235 and its daughters are almost in equilibrium. With the aid of these important considerations the γ-ambient dose rate can be determined.

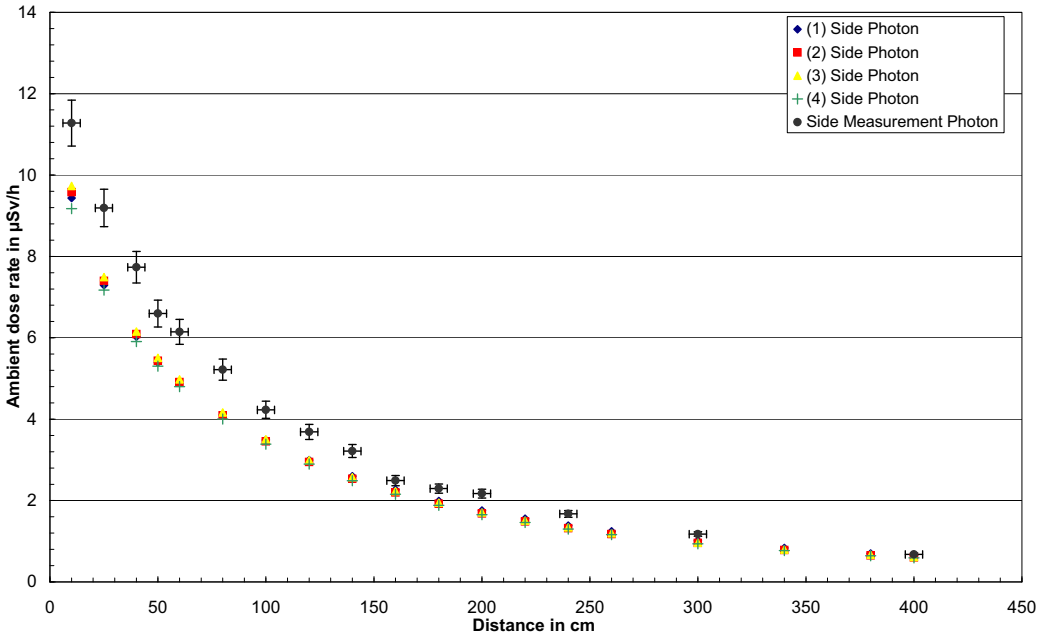

Figure 5.12: Calculated γ-ambient dose rate of the individual cylinder geometries and the measurement from the side of the cylinder in comparsion with the measurement values.

It is clearly shown, that the shape of the calculated values at side of cylinder are consistent with the shape of the measured values. With increasing distance the dose rate is steadily decreasing. This suggests, that the interaction of γ-photons with the surrounding matter are described correctly in MCNP. Otherwise it would also have to come to strong deviations in the shape of the curves. Since the γ-ambinet dose rate of the calculations of the individual cylinder geometries hardly differ, the distribution and the corresponding density of UF_6 from the side has not such a great influence on the γ-ambinet dose rate. Therefore, it would not care, which distribution of UF_6 in MCNP would be used. However, this will applies only for the case where the γ-ambient dose rate is calculated from the center of the cylinder side. It is very likely that the geometry of the cylinder and the distribution of UF_6 would lead to different results for other observation points.
Furthermore, it can be seen that the measured values are always higher than the

calculated values. After plotting the ratio between the calculated and the measured values against the distance (see figure 5.13), a mean deviation of about 20% can be observed.

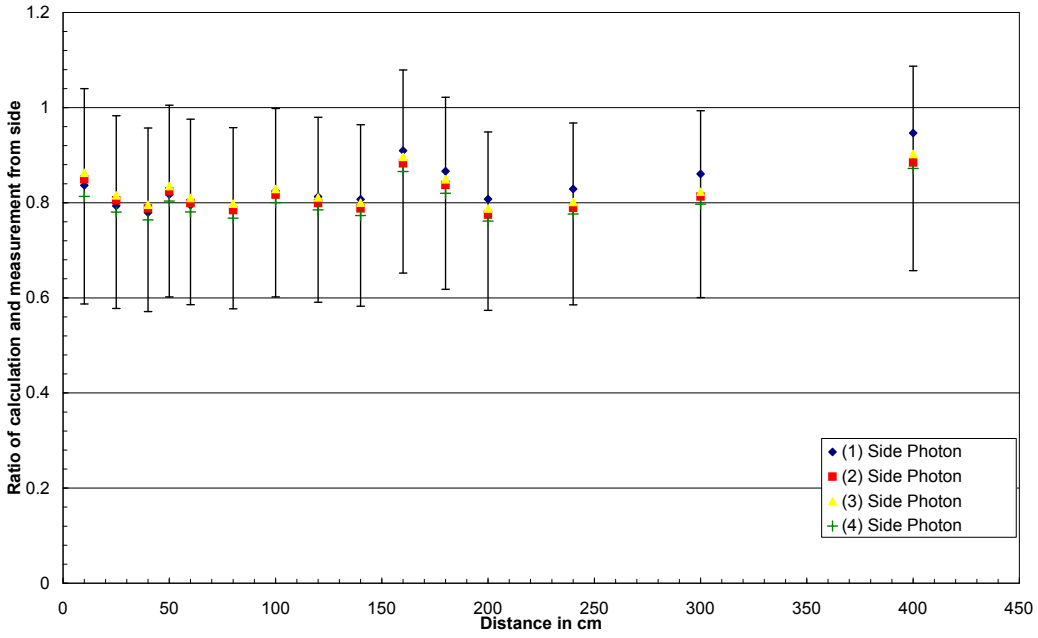

Figure 5.13: Ratio of the calculated values from side and the measured values from side plotted against the distance. Only the absolute uncertainties for geometry (4) are applied to do not overflow the graphic with error bars. The error bars of the other values of the different geometries are nearly in the same order. The ratios are within the absolute uncertainties.

The mean deviations of each geometry to the measurement can be extracted from table 5.2.

Geometry type	Mean deviation
(1)	-17%
(2)	-18%
(3)	-17%
(4)	-20%

Table 5.2: Mean deviation of the different cylinder geometries at the side of the cylinder.

Since the operational error limit of the *FH 40 G-10L* is ±24%, all types of geometries are in the operational error limit of the measurement device.

In the next step, the MCNP-calculations of the γ-ambient dose rate are compared with the measurement at the end of the cylinder (see figure 5.14).

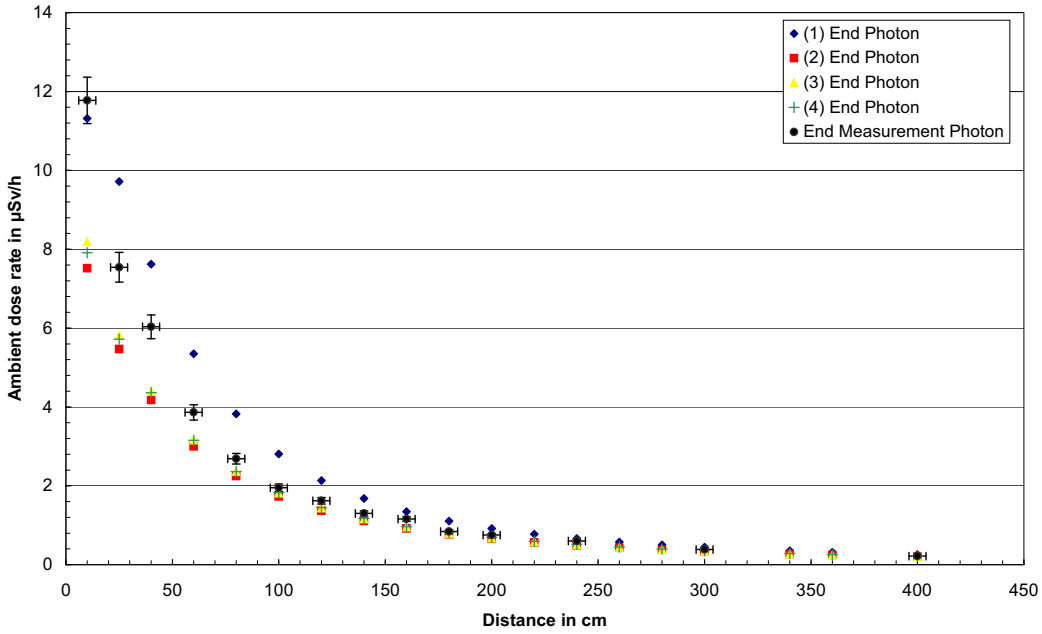

Figure 5.14: Calculated γ-ambient dose rate of the individual cylinder geometries and the measurement from the end of the cylinder in comparsion with the measurement values.

The MCNP-tallies are placed in such a way in the MCNP-simulation, that they are centrally located in various distances at the end of the cylinder. This corresponds exactly to the positions in which it is measured. In the calculations, the γ-ambient dose rate decreases, as expected, with increasing distances. Also, the shape of the calculated values is consistent with the shape of the measured values. However, there are strong differences in the γ-ambient dose rate in the vicinity of the cylinder. The calculation with the geometry with flat ends (1) overestimates the measured values and the other three geometries underestimate the values of the measurement.
Since the calculations on side underestimate the measurements, the geometries with underestimated values at the end of the cylinder are better suited for the evaluation of the results. In addition, these cylinder geometries correspond rather to the reality than the geometry of the cylinder with flat ends. But why does the geometry with flat ends overestimates the measured values so strong? This can be possible explained by the fact, that at flat ends the distance of UF_6 and thus the radiation source to the tally increases only in one direction as further one get away from the center of the ends. With round ends this behaivour is equal, but with the curvature the distance to the tally is greater than if the ends are flat. By this small, but essential difference in the distance of the UF_6 to the tally, the γ-ambient dose rate is strongly influenced near the cylinder. At greater distances, this effect do not influence the γ-ambient dose rate anymore since the ends of the cylinder can be viewed as a single point

source. This can be seen very clearly from figure 5.14, that the ambient dose rate of the geometry with the flat ends approaches the ambient dose rate of the cylinder geometries with round ends.
After plotting the ratio of the calculated values and the measured values against the distance, following results (figure 5.15) are presented.

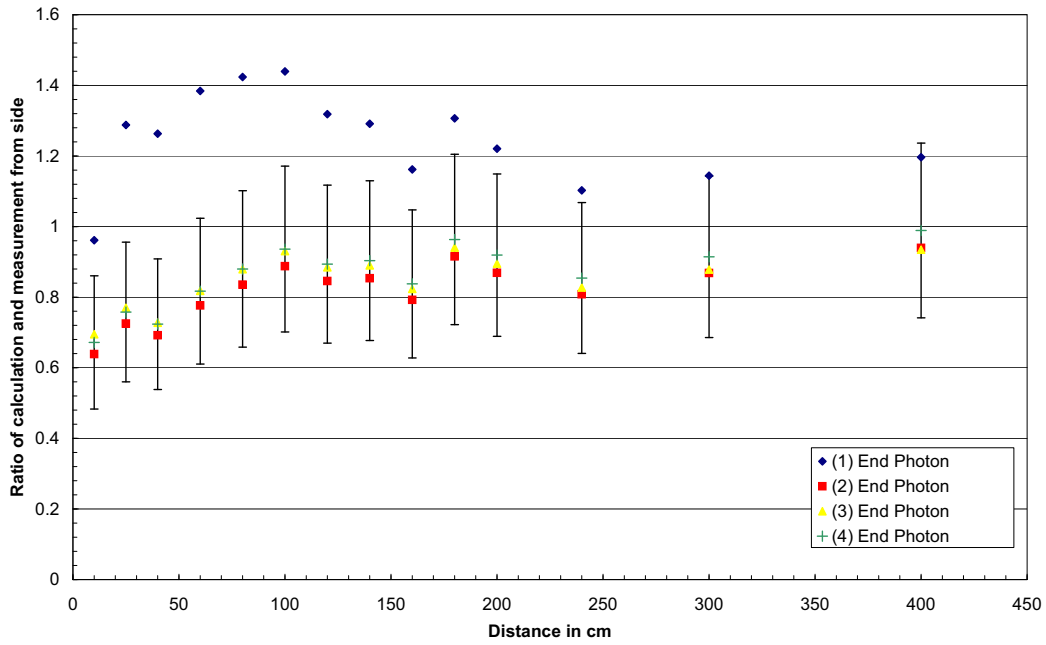

Figure 5.15: Ratio of the calculated values from end and the measured values from end plotted against the distance. Only the absolute uncertainties for geometry (4) are applied to do not overflow the graphic with error bars. The error bars of the other values of the different geometries are nearly in the same order. The ratios are within the absolute uncertainties.

On the basis of the deviations, it can be again clearly seen, that the calculated values of cylinder geometry (1) strongly overestimate the measured values and the calculated values of the γ-ambient dose rate of the other cylinder geometries underestimate the measured values. Clearly visible is also, that the deviations of the calculated values to the measured values 50 cm apart of the cylinder end is much stronger than the mean deviation at a distance from 50 cm. This could be the case because at the end of the cylinder, the geometry of the cylinder and the distribution of UF_6 in the cylinder take a greater influence on the γ-ambient dose rate. This assumption is supported, that the geometry of the cylinder at a far distance does not influence the γ-ambient dose rate because it can be viewed as a point source.
In table 5.3 the mean deviation of the calculated to the measured values is presented. The smallest mean deviation has the realistic geometry (4) with -13% and the largest

the simplified geometry (1) with +25%. All claculations with round ends at end of the cylinder are in the operational error limit of 24% of the measurement device.

Geometry type	Mean deviation
(1)	+25%
(2)	-18%
(3)	-15%
(4)	-14%

Table 5.3: Mean deviation of the different cylinder geometries at the end of the cylinder. The "+" or "-" indicate whether the calculated values overestimate or underestimate the measured values.

After the theoretical MCNP-calculations of γ-ambient dose rate at the side and end of different cylinder geometries with the measured values are compared, the theoretical MCNP-calculations of neutron-ambient dose rate are compared with the measured values (see figure 5.16 and 5.17). 1.500.000 source particles are started in MCNP to get a relative error below 1%. To get the neutron-ambient dose rate, the MCNP-tally for neutron radiation is multiplied with the neutron activity of the uranium isotopes in the UF_6 cylinder.
Both the MCNP-calculations of the neutron-ambient dose rate at the end and side of the different cylinder geometries are coincident with the measured values. The neutron-ambient dose rate of geometry (1) and (3) are in the vicinity of the cylinder outside the measurement results. This is the case because in geometry (1), as well as the γ-ambient dose rate, is overestimated and geometry (3), no longer self-shielding for the neutron by UF_6 occurs, so that the neutrons reach the tally without much interaction with the surrounding matter. Even though, only a few measuring points are taken at various distances, so that it can be argued that MCNP correctly reflects the neutron-dose rate within the operational error limit of the *Biorem FHT 751* with $\pm$20%.

5.3.5 Discussion of verification

In this section the results of the verification are briefly presented and discussed. The calculated values of the γ-ambient dose rate are below the measurement values by a factor between 13% and 20%. At the end of cylinder geometry (1), the calculated values are higher than the measurement results. This effect has been already explained above. But, why are the calculated values for the other geometries below the measured values? This can have several reasons. First, the calculations are within the operational error limits of $\pm$24%, so that the deviation can be explained

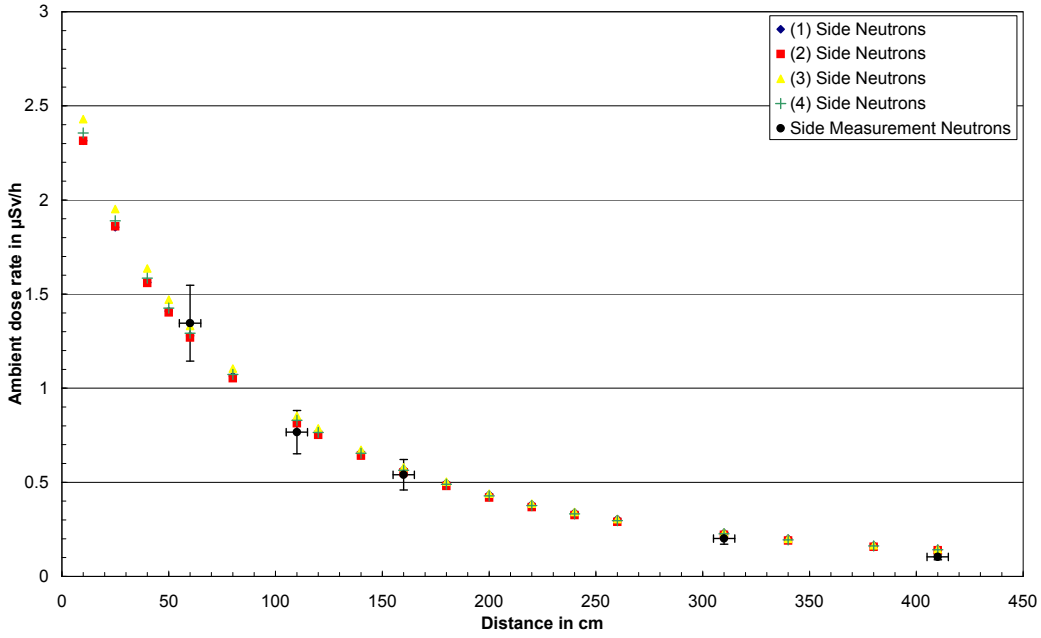

Figure 5.16: Neutron-ambient dose rate of the individual cylinder geometries and the measurement from the side of the cylinder.

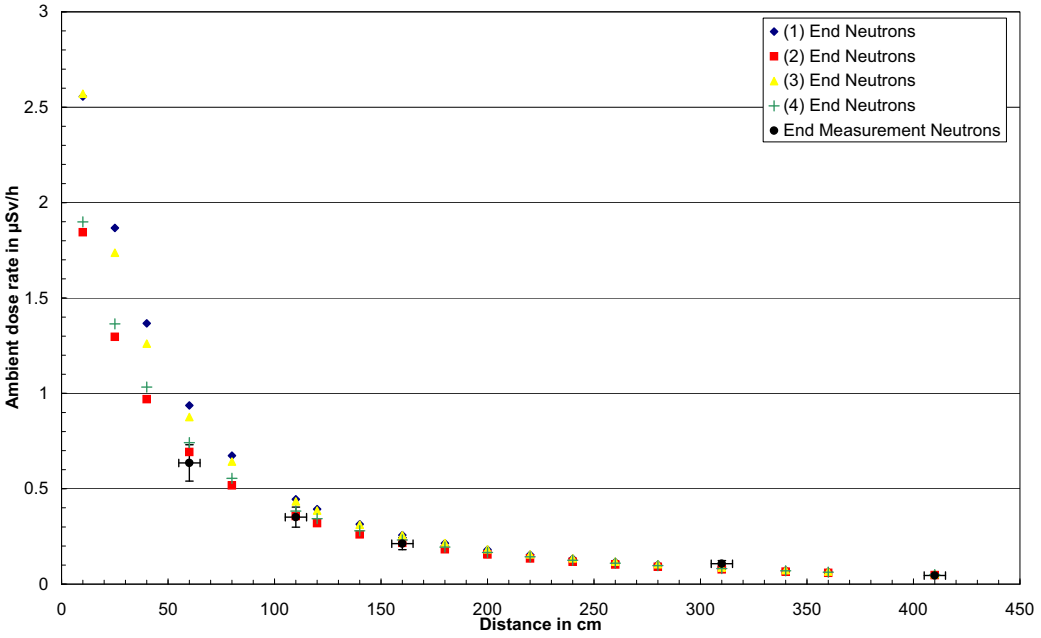

Figure 5.17: Neutron-ambient dose rate of the individual cylinder geometries and the measurement from the end of the cylinder.

by the measurement inaccuracy of the measurement device. Furthermore, the *FH 40 G-10L* is calibrated with the 662 keV line of Cs-137. But the γ-spectrum of the incoming photons from the UF_6 cylinder have γ-lines with the energy in a range of approximately 0.01 MeV and 2.6147 MeV, so that a calibration factor must be set for the measurement device in order to interpret the γ-spectrum from the UF_6 cylinder correctly. In addition, the geometry of a UF_6 cylinder and the distribution of the UF_6 can not be simmulated in MCNP to 100% reality, so that there can be also deviations between the measured values and the calculated values.
Another, but not yet extensively investigated effect, is the so-called thermal cycling effect, which can increase the γ-ambient dose rate and thus could explain the higher measurement values. As the name implies, the thermal cycling effect involves the rearrangement of the UF_6 within the cylinder during rapid temperature variations. Intuitively, this can be explained by an example. If the cylinder is outside over an extended period of time, it will constantly exposed to temperature changes by daytime and nighttime. In daytime, the temperature of the cylinder rises by the sunlight and the UF_6 near the cylinder wall goes into the gaseous state and diffuses through the cracks of the solid UF_6, which results by production process. In nighttime the temperature drops and the previously gaseous UF_6 freezes in the cracks. This process can be compared on the basis of the phase diagram 2.2. After diffusion, the density of UF_6 is now lower near the cylinder wall and the shielding effect is smaller, so that the γ-ambient dose rate increase. At neutron-radiation, this effect has only a very small influence since the density differences between normal distribution and after thermal cycling process is too slow.
For neutron-ambient dose rate, the calculated values agree very well with the measured values, so that the calculated values for neutron-ambient dose rate are verified. The reason for the good agreement is, that the neutron spectrum of UF_6 is pretty identical with the fission spectrum of Cf-252 (see section 4.5) and the *Biorem FHT 751* is also calibrated with Cf-252. A distinguished agreement is given for the measured results and the theoretical calculations of neutron-ambient dose rate. However, caution is necessary, since only selected receiving points are compared and no precise shape of the measured values in various distances could be created.

5.4 MCNP calculations of effective dose rate from UF6 cylinders

In this section, the theoretical MCNP-calculations of the effective dose rate of different types of cylinders will be presented. With the different types of cylinders it is supposed the various degrees of enrichment and depletion of U-235. Since an enrichment of U-235 up to 6% and thereby a degree of depletion of about 0.43% is achieved here at URENCO Germany, these types of cylinders are also examined.
As mentioned above, the effective dose rate reflects the individual dose of a people within a specific period. Due to the fact, that some employees work more or less directly with the UF_6 cylinders (e.g. transport, storage, filling or emptying), the MCNP-calculations stated very good results of the effective dose rate, since for each individual production step the exact distance and the approximate working time is known. These investigations have particular importance in terms of radiation protection because radiation-exposed people should not exceed a certain value of effective dose. Radiation-exposed people of category A do not exceed an effective dose of 20 mSv and people of category B not over 6 mSv in a year.
In section 5.3, the verification between real measurements and theoretical MCNP-calculations are completed successfully. For this section, the realistic geometry (4) is used because it reflects most closely the reality of an UF_6 cylinder and the distribution of UF_6 in the cylinder and both the results of γ-dose rate and neutron-dose rate are conformed. In the following calculations, the daughter nuclides of the uranium isotopes have an ingrowth time of 12 months. This is conservative because the daughter nuclides of U-235 and U-238 are in equilibrium with the individual uranium isotopes. The daughter nuclides of U-232 have then an activity of 30.25% of the activity of U-232 itself. In addition to that, the nuclide vectors for the uranium isotopes in the MCNP-calculations are choosen in such a way, that they agree with the enrichment and depletion degree.

5.4.1 Effective dose rate from a 48Y-Product cylinder with 6% enrichment

The effective dose rate from an enriched 48Y-Product cylinder with 6% U-235 is higher than the effective dose rate from depleted Tails or Feed with natural composition of Uranium because next to U-235, U-234 and U-232 are enriched at the same time and by this the activity of these uranium isotopes increases due to the higher amount of these uranium isotopes after enrichment. Since U-234 and U-232

provide a significant contribution to the effective neutron-dose rate and U-232 also to effective γ-dose rate, it is evident that for enriched UF_6 the highest effective dose rate is expected. Hence, the effective dose rate of a 48Y-Product cylinder with 6% enriched UF_6 will be investigated very well and for the other cylinder types only the results of the total effective dose rate is presented.
The total effective dose rate of the 48Y-Product cylinder with 6% enrichment from end and side of the cylinder in a distance area from 10 - 400 cm is presented in figure 5.18.

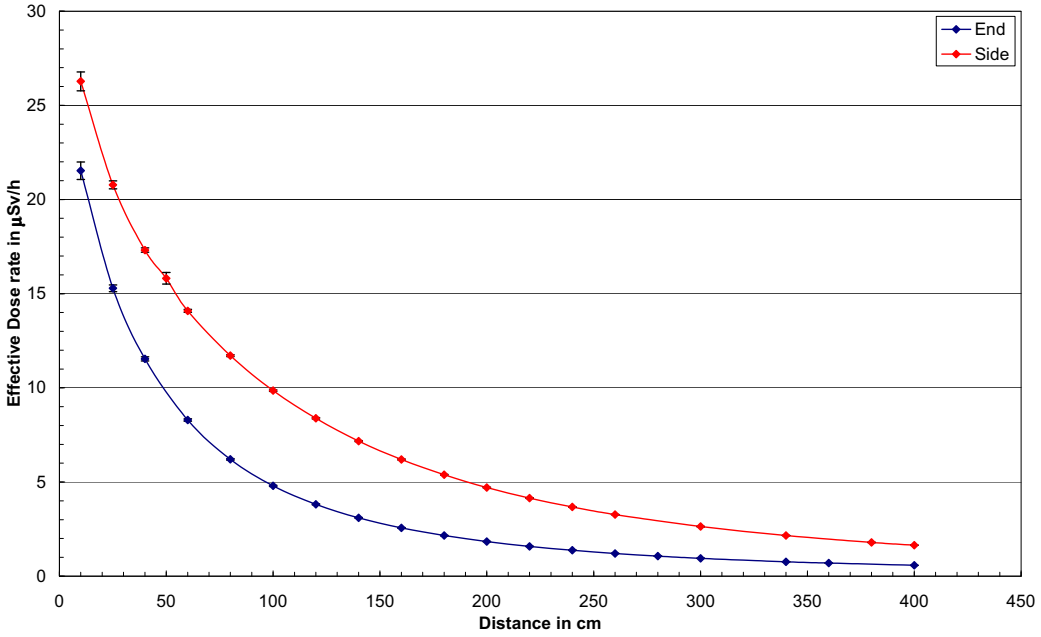

Figure 5.18: Total effective dose rate of a 48Y-Product cylinder with 6% enrichment and an ingrowth time of 1 year for the daughter nuclides of the uranium isotopes from the end and the side of the UF_6 cylinder. The effective dose rate is plotted linear against the distance to the outermost cylinder point from side and end. The points are connected together for a better illustration.

As expected, the highest effective dose rate is near the cylinder wall and decreases with increasing distance. Here, the effective dose rate from side is higher than from end of the cylinder. This can be explained in the above mentioned description, that the cylinder has from the side view more individual radioactive sources and therefore more photons reach the tally, which automatically leads to a higher effective dose rate from side than from end of the cylinder. If the effective dose rate is plotted double logarithmic against the distance (see figure 5.19), the effective dose rate will have a linear shape in the double logarithmic plot at distances which are further away from the cylinder. Due to the double logarithmic plot, the *inverse square-law* of a

radioactive point source can be written as follows:

$$Log(\dot{E}) = Log\left(\frac{C}{r^2}\right) = -2 \cdot Log(r) + Log(C) \tag{5.3}$$

with $\dot{E}$ as the effective dose rate, r as the distance and C as a constant which includes the activity and a radiation constant.

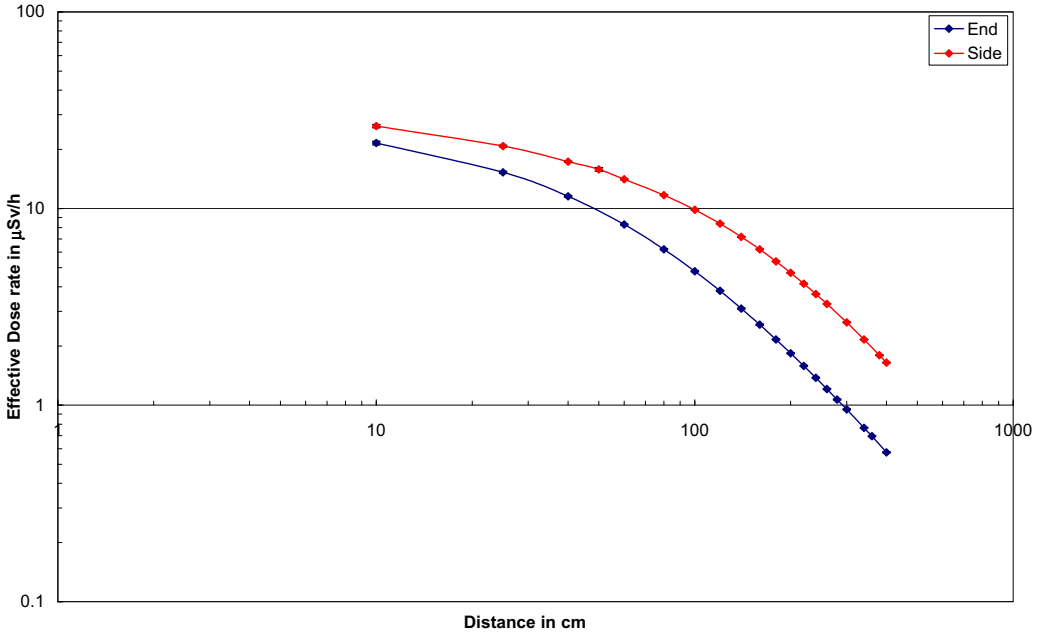

Figure 5.19: Double logarithmic plot of the total effective dose rate of a 48Y-Product cylinder with 6% enrichment. The points are connected together for a better illustration.

This linearity can be clearly seen in figure 5.19. At side, the linear transition begins at about 2 m, wherein at the end a transition in the linearity is achieved at about 1 m. This delayed transition to the linearity on the side makes sense because the dimensions from the perspective of the side of the cylinder are much larger than from end and therefore the approximation to a point source from the side is in a further distance.
Since the cylinder approximately corresponds to a point source at large distances and due to the fact, that the cylinder has then still a certain dimension in the geometry, the linear equation far away from side and end of the UF_6 cylinder differs from equation 5.3. The line equations in the double logarithmic plot are fitted with the points from 1 m to 4 m from end and from 2 m to 4 m from side and have the following forms:

$$Log(\dot{E}) \approx -1.58\ Log(r) + Log\,(7676)\,\frac{\mu Sv \cdot cm^2}{h} \qquad \text{(from End)}$$

$$Log(\dot{E}) \approx -1.53\ Log(r) + Log\,(15524)\,\frac{\mu Sv \cdot cm^2}{h} \qquad \text{(from Side)}$$

In the following, the previously learned knowing about the distribution of the effective dose rate of a 6% enriched UF_6 cylinder at various distances can be applied to a simple example on radiation protection. Since, as already mentioned, a Product-cylinder radiates more than a Feed- or Tails-cylinder, a radiation-exposed employee works in the worst case 2000 h in a year with a 6%-Product-cylinder from side. This scenario is very conservative because a worker never worked such a long time with a Product-cylinder. Nevertheless, a feeling for the effective dose rate of a Product-cylinder can be obtained by this example. Table 5.4 itemise the effective dose of a radiation-exposed employee, who works 2000 h in a year in a certain distance with a 6%-Product cylinder from side.

Distance r in cm	$\dot{E}$ in $\mu Sv/h$	Effective dose E in mSv
10	26.27 ± 0.50	52.54 ± 1.00
50	15.82 ± 0.31	31.64 ± 0.62
100	9.86 ± 0.04	19.72 ± 0.08
200	4.71 ± 0.02	9.42 ± 0.04
300	2.63 ± 0.01	5.26 ± 0.02
400	1.64 ± 0.01	3.28 ± 0.02

Table 5.4: Table of the effective dose of a radiation exposed person, who works 200 h with a 48Y-Product cylinder with an ingrowth time of one year and an enrichment of 6% in various distances. The values of the effective dose rate $\dot{E}$ are MCNP-calculations with the absolute uncertainty of MCNP.

A radiation-exposed person who operates consistently below 1 m to a Product-cylinder reaches a maximum effective dose of about 53 mSv and exceed the limits of the categories A and B for a radiation-exposed person. Only at a distance of about 1 m to the cylinder, the maximum dose of an exposed person is below the limits of category A and from about 3 m below the limits of category B. This example shows again, that in respect on radiation safety and radiation protection always a healthy distance from the radioactive source must be complied and the retention time must be reduced to minimize the effective dose.

In the following lines, the single contributions are presented that contribute to the total effective dose rate because the sum of the single contributions gives the total effective dose rate. In chapter 4, the single radiation contributions are presented which are produced in the UF_6 cylinder by physical processes. Hence, these single contributions are illustrated in figure 5.20 from end and figure 5.21 from side of the cylinder.
It is clearly seen, that the shape of the individual contributions from side and end differs only in the amount of the effective dose rate. The greatest contribution of a 6% Product cylinder to the total effective dose rate is the neutron-radiation, since due to the enrichment the activities per gram uranium of U-232, U-234 and U-235 are increasing in contrast to Feed and Tails, where the amount of these uranium isotopes is much smaller (see table A3). The second highest contribution to the total effective dose rate derives from the uranium isotope U-238 and especially of their daughter nuclides. Followed by the bremsstrahlung which is produced by the decay of Pa-234m. Finally, the contributions of U-232 plus daughter nuclides and U-235 plus daughter nuclides have a very small contribution to the total effective dose rate. The activities for the single radiation contributions are presented in table 5.5. The total mass of uranium in a 6% enriched 48Y-Product cylinder is 8445894.37 $g_{Uranium}$.

Isotopes	Activity in $\gamma(n)/s/g_{Uranium}$	Activity in γ(n)/s
U-238 + daughters	3606.81	30462733597.76
U-232 + daughters	219.56	$1854399258.77 \cdot 0.3025$
U-235 + daughters	10394.13	87787740534.16
All uranium	(0.421)	(3553984.6)

Table 5.5: Activity of the individual radiation components of a 48Y-Product cylinder with 6% enrichment. The numbers in brackets are the neutron activities. Multiplying the activity with the respective MCNP-tally, the effective dose rate in μSv/h is obtained.

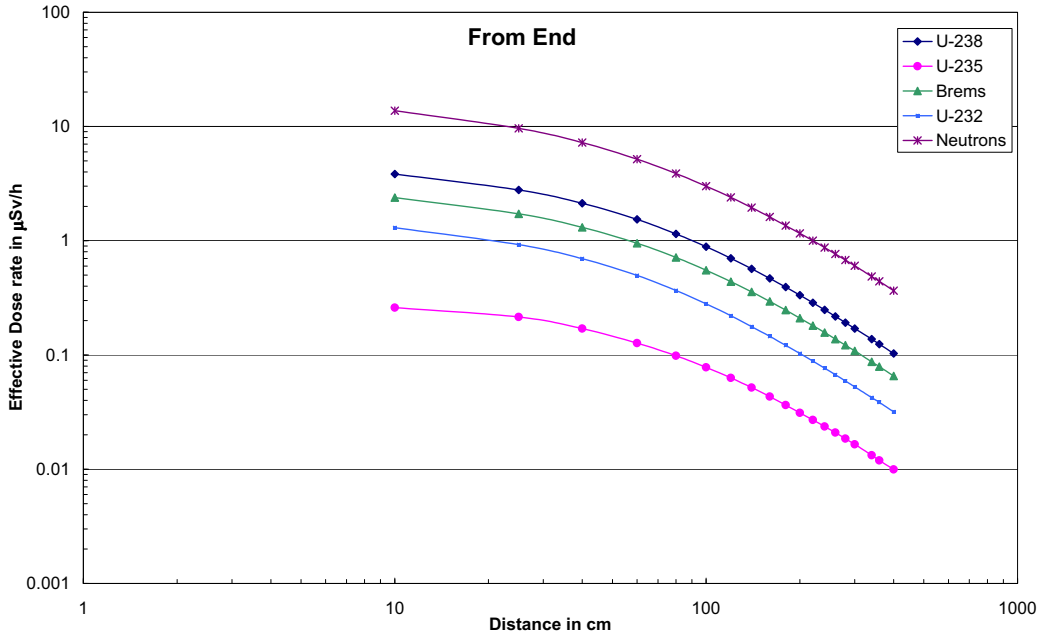

Figure 5.20: Effective dose rate from end of a 6%-Product cylinder with the single radiation contributions, which are produced by physical processes in an UF_6 cylinder. The points are connected together for a better illustration.

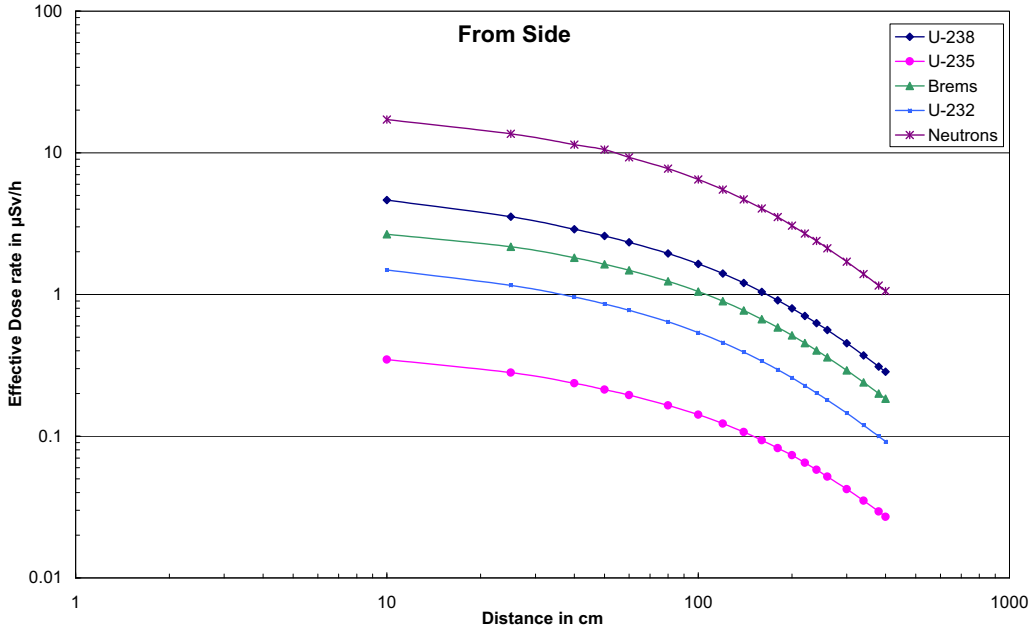

Figure 5.21: Effective dose rate from side of a 6%-Product cylinder with the single radiation contributions, which are produced by physical processes in an UF_6 cylinder. The points are connected together for a better illustration.

5.4.2 Effective dose rate from a 48Y-Feed cylinder with natural composition of uranium isotopes

In this section the total effective dose rate of a 48Y Feed UF_6 cylinder with a natural composition of uranium isotopes is presented. In figure 5.22 the total effective dose rate from side and end of the UF_6 cylinder is plotted against the distance. The total effective dose rate has a decreasing shape with increasing distance and the effective dose rate is from side higher than from end. All these effects are the same as described above for the Product cylinder. Unlike to the 6%-Product cylinder, the effective dose rate of the Feed cylinder is smaller by a factor of skimpy over 2. This is due to the low neutron-effective dose rate, which no longer provide the largest contribution in Feed. Logically, the activity of neutrons per gram uranium decreases because the uranium isotope U-232, U-234 and U-235 have a smaller contribution to the total uranium mass. The reduction of these isotopes of uranium to the total mass simultaneously reduces the activity and thus the effective dose rate.

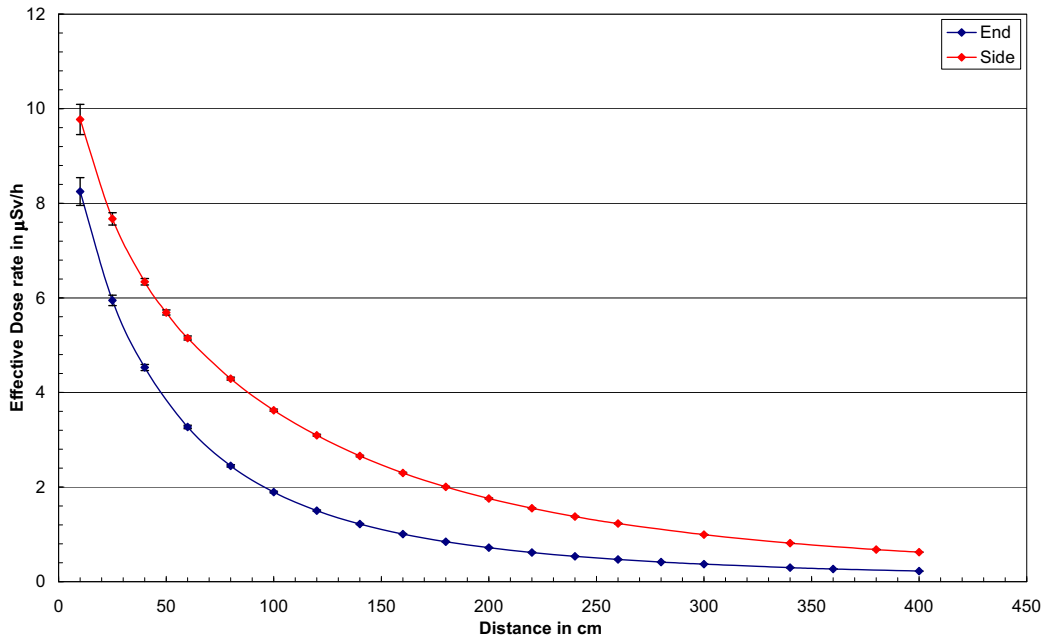

Figure 5.22: Total effective dose rate of a 48Y-Feed cylinder with an ingrowth time of 1 year for the daughter nuclides of the uranium isotopes from the end and the side of the UF_6 cylinder. The effective dose rate is plotted linear against the distance to the outermost cylinder point from side and end. The points are connected together for a better illustration.

In contrast to the reduction of the effective dose rate by neutrons, the contribution of γ-effective dose rate from U-238 plus daughters and bremsstrahlung increase beacuse through the small amount of U-235 and U-232 more U-238 is present in the

total mass of uranium. Since this contribution has not such a large effect on the effective dose rate as the contribution of the reduction of the neutron-radiation, the effective dose rate in Feed is approximately half of the effective dose rate of 6%-Product, so that a employee who works with a 48Y-Feed cylinder only gets half of the effective dose than someone who works with a full 48Y-Product cylinder with 6% enriched uranium. The single radiation contribution for the effective dose of a Feed cylinder are presented in the appendix in figure A2 from end and A3 from side.
The activities of each radiation contribution in a Feed cylinder is presented in table 5.6. The total mass of uranium in a 48Y-Feed cylinder is 8451598.3 $g_{Uranium}$.

Isotopes	Activity in $\gamma(n)/s/g_{Uranium}$	Activity in γ(n)/s
U-238 + daughters	3812.21	32219285043.45
U-232 + daughters	15.5	$130964579.5 \cdot 0.3025$
U-235 + daughters	1231.7	10409872810.32
All uranium	(0.062)	(523968.06)

Table 5.6: Activity of the individual radiation components of a 48Y-Feed cylinder. The numbers in brackets are the neutron activities. Multiplying the activity with the respective MCNP-tally, the effective dose rate in μSv/h is obtained.

5.4.3 Effective dose rate from a 48Y-Tails cylinder with 0.43% depletion

The values of the effective dose rate (see figure 5.23) of a full 48Y-Tails cylinder is approximately equal to the effective dose rate of a 48Y-Feed cylinder because the nuclide vectors of the individual isotopes of uranium hardly differs. Thus, Feed has 0.711% U-235 and tails 0.43% U-235. U-234 also hardly differs between these two types, so that these minimal differences in the mass of each uranium isotope only differs the activity slightly and thus the effective dose rate between Feed and Tails differ no more than 10%. These difference in the effective dose rate lies only in the amount of the different activities because the material distribution of the uranium isotopes are nearly the same in Feed and Tails. The single radiation contribution for the effective dose of a Tails cylinder are presented in the appendix in figure A4 from end and A5 from side. The activities for the single radiation contributions are presented in table 5.7. The total mass of uranium in a 0.43% depleted 48Y-Product cylinder is 8451924.57 $g_{Uranium}$.

Isotopes	Activity in $\gamma(n)/s/g_{Uranium}$	Activity in γ(n)/s
U-238 + daughters	3823.32	32314405900.61
U-232 + daughters	2.83	$23876972.65 \cdot 0.3025$
U-235 + daughters	736.25	5608662423.09
All uranium	(0.043)	(362201.79)

Table 5.7: Activity of the individual radiation components of a 48Y-Tails cylinder with 0.43% depletion. The numbers in brackets are the neutron activities. Multiplying the activity with the respective MCNP-tally, the effective dose rate in μSv/h is obtained.

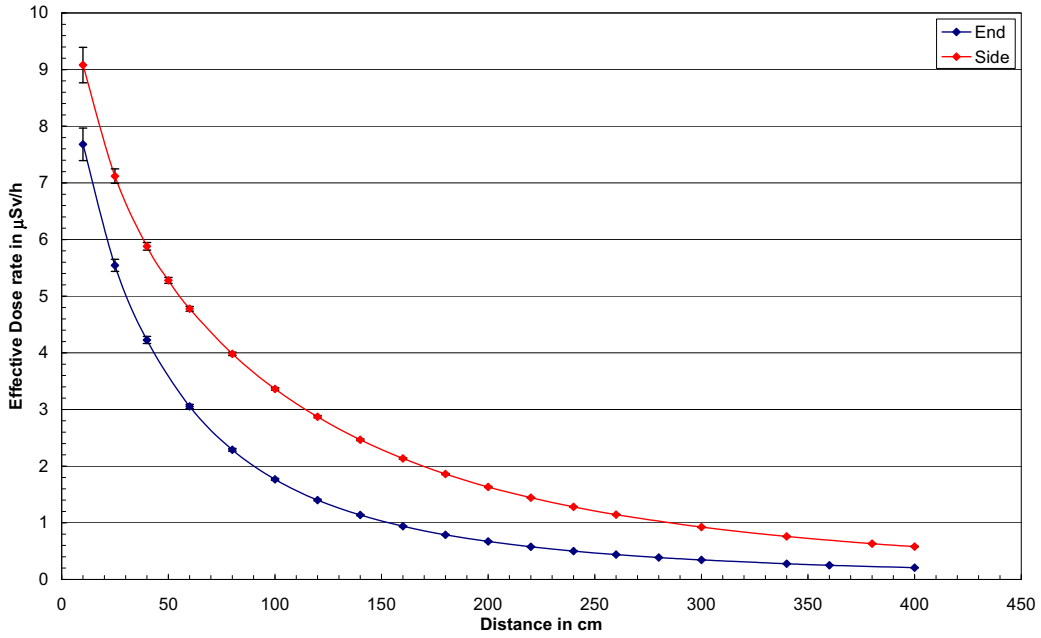

Figure 5.23: Total effective dose rate of a 48Y-Tails cylinder with 0.43% depletion and an ingrowth time of 1 year for the daughter nuclides of the uranium isotopes from the end and the side of the UF_6 cylinder. The effective dose rate is plotted linear against the distance to the outermost cylinder point from side and end. The points are connected together for a better illustration.

5.4.4 Effective dose rate from a 30B-Product cylinder with 5% enrichment

In this section the effective dose rate from side and end of a 30B-Product cylinder with 5% enriched UF_6 is presented. According to the ANSI specifications for a 30B UF_6 cylinder, it may be only filled with a maximal degree of 5% enriched UF_6, so that a fed with 6% enriched UF_6 is omitted and only 5% enriched UF_6 is chosen. Analogue to the 48Y cylinder, the UF_6 in the 30B-cylinder is distributed at the cylinder wall. Since the geometric dimensions of the 30B cylinder are much smaller than that of a 48Y cylinder (see section 2.4), this must accordingly adjusted for the geometry in MCNP. Moreover, only a total mass of 2277 kg UF_6 are permitted to fed into a 30B cylinder which must be also considered in the MCNP-calculations. The nuclide vectors of the individual uranium isotopes are adjusted by the typical degree of 5% enrichment, so that the total activity is thereby defined. The activities for the single radiation contributions are presented in table 5.8. The total mass of uranium in a 5% enriched 30B-Product cylinder is 1538381.05 $g_{Uranium}$.

Isotopes	Activity in $\gamma(n)/s/g_{Uranium}$	Activity in γ(n)/s
U-238 + daughters	3645.82	5608662423.09
U-232 + daughters	146.37	$225180231.87 \cdot 0.3025$
U-235 + daughters	8661.78	13325113021.76
All uranium	(0.33)	(501168.81)

Table 5.8: Activity of the individual radiation components of a 30B-Product cylinder with 5% enrichment. The numbers in brackets are the neutron activities. Multiplying the activity with the respective MCNP-tally, the effective dose rate in μSv/h is obtained.

In figure 5.24 the total effective dose rate from side and end of a 30B-Product cylinder with 5% enriched UF_6 is presented. If the shape of the effective dose rate of a 30B-Product cylinder is compared with the shape of the effective dose rate of a 48Y-Product cylinder, it can be clearly seen, that the effective dose rate of a 30B-Product cylinder drops more in the vicinity of the cylinder than the effective dose rate close to a 48Y-Product cylinder. This property makes it clear again, that the lower activity and lower dimensions of the geometry of the 30B-product cylinder reduces the effective dose rate very strong in distance. In a distance of around 1.5 m, the effective dose rate is already less than $2\mu Sv/h$ from side and end. Since 30B-Product cylinders are shiped from the uranium enrichment facility Gronau to atomic power plants, only a minimal danger on the basis of radioactiv radiation consits for the population. Moreover, the 30B-Product cylinder will be shiped in a transport box of steel, so that the radiation of the 30B-Product cylinder is also dramatically reduced

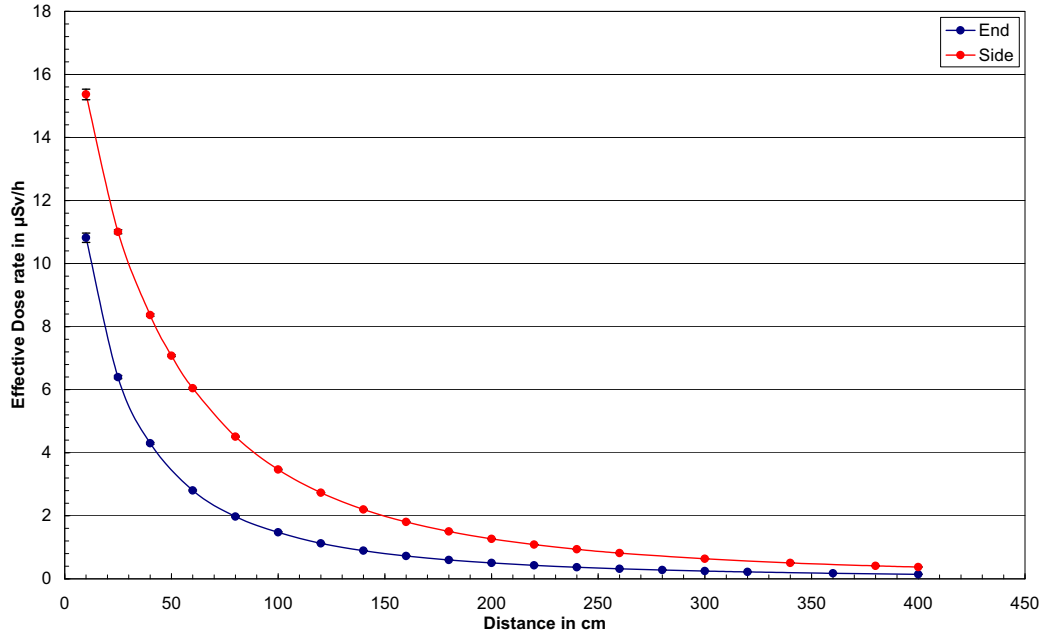

Figure 5.24: Total effective dose rate of a 30B-Product cylinder with 5% enrichment and an ingrowth time of 1 year for the daughter nuclides of the uranium isotopes from the end and the side of the UF_6 cylinder. The effective dose rate is plotted linear against the distance to the outermost cylinder point from side and end. The points are connected together for a better illustration.

again. From the point of view of radiation protection, there is no danger for the population, if a 30B-Product cylinder is shiped. The single radiation contributions for the effective dose of the 30B-product cylinder with 5% enrichment are presented in the appendix in figure A6 from end and A7 from side.

5.4.5 Effective dose rate from a fresh emptied 48Y-Product cylinder with 5% enrichment

As the last cylinder type, a fresh emptied 48Y-Product cylinder is investigated which included previously 6% enriched UF_6. After emptying only the daughter nuclides of uranium isotopes remain in the cylinder because they have a higher sublimation point and do not go into the gaseous state after heating of the cylinder. The daughter nuclides are distributed uniformly on the cylinder wall. The amount of the daughter nuclides is defined depending on the prior storage time of the cylinder. With a storage time of about 1 year, about 2 kg of daughter nuclides are produced.
In MCNP, the cylinder is modeled in such a way, that the steel cylinder has the same form as in geometry (4). However, no UF_6 or the remain of daughter nuclides are

inserted as an additional material because the 2 kg layer of daughter nuclides, which is distributed uniformly around the cylinder wall has only a layer ofunder 0.1 mm. A vacuum is modeled in the cylinder itself, so that no interaction between the γ-photons and surrounding matter may take place. Since only the daughter nuclides are present in the cylinder and thus contribute to the radiation, the photons produced by the uranium isotopes are eliminated in MCNP. This also results to a reduction of the total activity. The total activity of the individual daughter nuclides is presented in table 5.9.

Isotopes	Activity in $\gamma/s/g_{Uranium}$	Activity in γ/s
Daughters of U-238	2563.81	21653669059
Daughters of U-232	204.5	$1727218713 \cdot 0.3025$
Daughters of U-235	4677.57	39506233446

Table 5.9: Activity of the individual radiation components of a fresh emptied 48Y-Product cylinder with 6% enrichment. Multiplying the activity with the respective MCNP-tally, the effective dose rate in μSv/h is obtained.

The contribution of neutron radiation to the effective dose rate is produced exclusively by the spontaneous fission of uranium isotopes or the (α,n)-reaction between the α-particles and the fluorine cores. Since only daughter nuclides are still in the cylinder, no neutron radiation is generated, which could have a contribution to the effective dose rate. Therefore, the effective dose rate of the neutron radiation is neglected in MCNP. The bremsstrahlung is normally generated by the interaction with UF_6 and the steel of the cylinder wall. Since the interaction with UF_6 is no longer present, but only the interaction with the steel of the cylinder wall, the bremsstrahlung photon yield is lower by about the half in comparsion to the bremsstrahlung photon yield with interaction of UF_6 and steel. The exact bremsstrahlungphoton yield has been calculated with comparative calculations in MCNP.
The results of the effective dose rate calculations of a fresh emptied 48Y-Product cylinder from side and end is presented in figure 5.25 and the single radiation contributions for the effective dose of the fresh emptied 48Y cylinder with 6% enrichment are presented in the appendix in figure A8 from end and A9 from side.

As it can be clearly seen, the effective dose rate of a fresh emptied 48Y-Product cylinder, which was prior filled with 6% enriched UF_6, is by a factor of about 4 greater than a filled 48Y-Product cylinder, although the activity is even slightly smaller. This is the case because no longer a shielding effect of the UF_6 is available. Due to the high effective dose rate, it is necessary to work with great caution with freshly emptied cylinders. Therefore, the cylinder is placed after emptying as quick

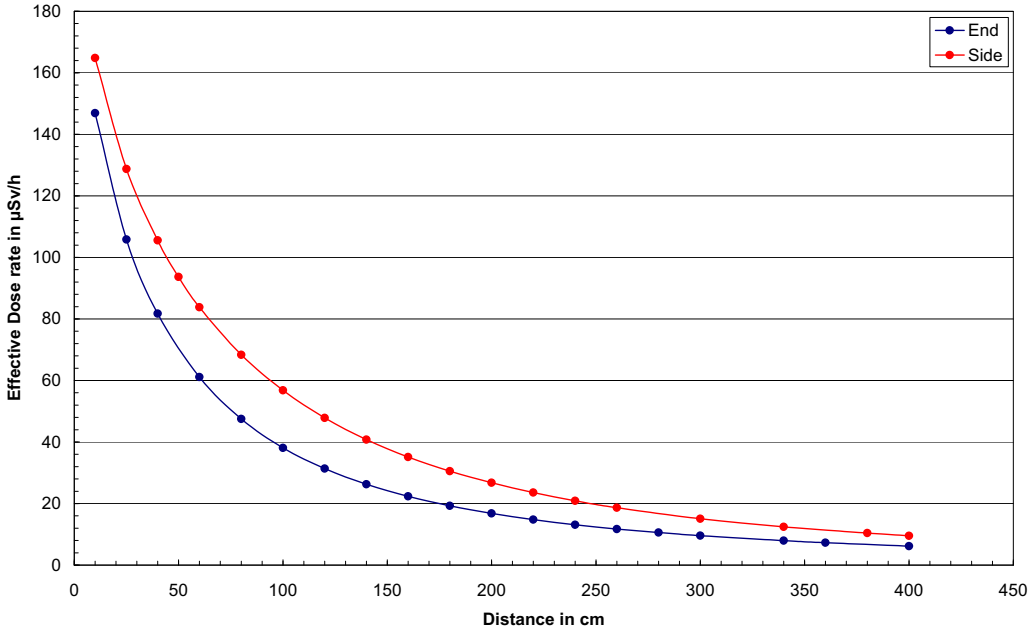

Figure 5.25: Total effective dose rate of a fresh emptied 48Y-Product cylinder with prior 6% enriched UF_6 and an ingrowth time of 1 year for the daughter nuclides of the uranium isotopes from the end and the side of the UF_6 cylinder. The effective dose rate is plotted linear against the distance to the outermost cylinder point from side and end. The points are connected together for a better illustration.

as possible between full 48Y-Product cylinders over an extended period of about 3 months, so that the daughter nuclides of the uranium isotope decay in this period and thus reduce the effective dose rate. After 3 months of storage period, the activity of the daughter nuclides of U-238 will have an activity of only 7.5% to the initial activity. The daughters from U-235 will decay almost completely in this period due to the short half-life of 25.52 h of Th-231 and the daughter nuclides of U-232, which half-life is directed to Th-228, will still have an activity of about 91% to the initial activity. After a storage period of about 3 months, the freshly emptied cylinder has approximately the effective dose rate of a full 6% 48Y-Product cylinder. The shape of the effective dose rate of a fresh emptied 48Y-UF_6 cylinder with increasing distance is consistent with the previously observed 48Y-cylinders.

5.4.6 Discussion of the results of effective dose rate calculations

In the previous sections, some types of cylinders with different enrichment and depletion degrees have been presented. Of course, there are more different types of cylinders with a wide variety of enrichment and depletion degrees. However, as a general rule, the degrees of depletion and enrichment are lower than the recently presented cylinder types and thus the effective dose rate is lower due to the resulting lower activity. For every enrichment and depletion degree, independent MCNP-calculations must be carried out, since the nuclide vectors of the uranium isotopes change for every enrichment and depletion. Therefore, a table of many different types of cylinders with the corresponding effective dose rates would be recommended. This could not be created in this master thesis due to the high effort of the MCNP-calculations.
From the investigations the conclusion can be drawn, that the effective dose rate decreases with increasing distance from the UF_6 cylinder and the cylinder assume the form of a point source by increasing distance. This effect is visible in the double logarithmic plot of the effective dose rate to the distance (see figure 5.19). Furthermore, the effective dose rate of full UF6 cylinders increase with increasing enrichment because not only U-235 is enriched, but also U-234 and U-232 which deliver also a significant contribution to the effective neutron-dose rate or to the effective γ-dose rate. Therefore, in respect of radiation protection, a full 6%-Product cylinder can be used to estimate the effective dose rate in a highly conservative way like it is done in table 5.4. Freshly emptied cylinders can have a very high effective dose rate, which is larger by a factor of 4 as full cylinders. This is the case because the activity of the daughter nuclides is nearly just the same like a full cylinder after emptying and due to the missing shielding effect of UF_6 many γ-photons can leave the cylinder and contribute to the effective dose rate. However, the dose rate will decreases by approximately 300%, if the cylinder has a storage time of ca. 3 months and nearly all daughter nuclides are decayed.
In figures 5.26 from side and 5.27 from end are all previously studied cylinder types presented again in a double logarithmic plot. It clearly shows, that the effective dose rate for all 48Y-cylinders has the same shape and differ only by a factor. For 30B-cylinder, the effective dose rate falls off more sharply. This explains, that the geometry of the UF_6 cylinder has a decisive influence on the strongness of the effective dose rate.

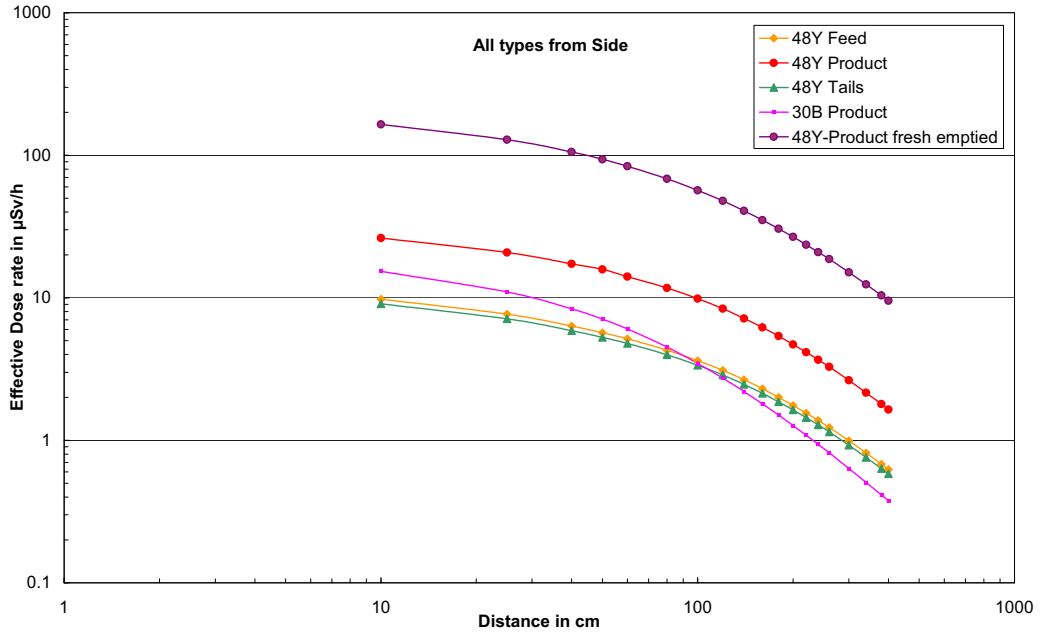

Figure 5.26: Effective dose rate from side of all investigated cylinder types in the double logarithmic plot. The points are connected together for a better illustration.

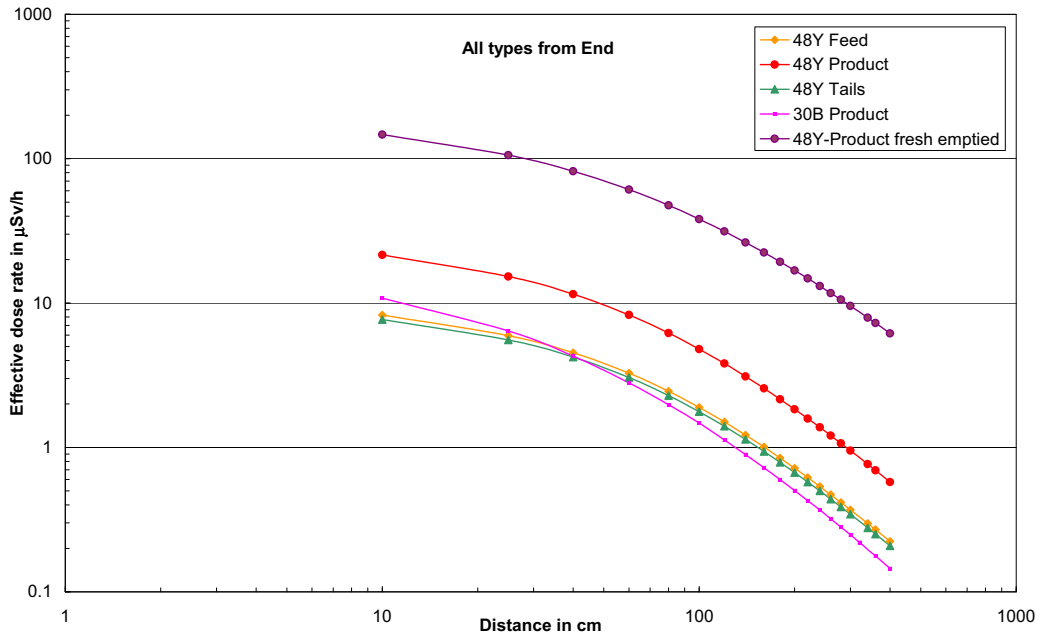

Figure 5.27: Effective dose rate from end of all investigated cylinder types in the double logarithmic plot. The points are connected together for a better illustration.

5.5 MCNP calculations of the Product-Store (PL-2)

As a further investigation using MCNP in terms of radiation protection, a complete building that is filled with a certain numbers of emptied and full Product cylinders is now simulated. In this case, the Product-Store (PL-2) is considered which is located on the permises of URENCO Deutschland. By government regulations, certain conditions must be guaranteed in respect of radiation safety and radiation protection for the PL-2. So the ambient dose rate, which is generated by the cylinders inside of PL-2, may not exceed the limit of 0.5 $\mu Sv/h$ outside of PL-2. This value of less than 0.5 $\mu Sv/h$ is chosen in that way, that for a retention time of 2000 hours in a year, the resulting individual dose is still below 1 mSv. Furthermore, a employee in the PL-2 does not reach an individual dose of maximal 6 mSv per year and in the loading area the maximal limit of the ambient dose rate of 1 $\mu Sv/h$ from background radiation must be abided. To determine the ambient dose rates of the PL-2 in respect of radiation protection and radiation safety for the employees, all relevant information about the admeasurement of the PL-2, the allocation of the cylinders and their activity and the measuring points in the PL-2 must be required. This will be shown systematicaly in the following.

5.5.1 Admeasurement of PL-2 and cylinder allocation

Since such a building is constructed of many individual components and it is impossible to include all these components into the simulation, only the physically necessary parts of the building are included in the simulation. This means, the exterior building wall which has a large influence on the shielding of radiation, doors and windows and of course supporting inner walls and radiation protection walls. In the MCNP-simulation, the PL-2 has the following simplified geometry. The whole PL-2 is located on a 10 cm thick concrete floor, and below the concrete floor is dry earth. The outer wall consists of 49 cm thick concrete up to a height of 2 m and from 2 m of 23 cm thick concrete. The windows and doors which are located in the outer wall are defined as block-outs. This corresponds to the situation that they are open. The interior walls in Pl-2 are 30 cm thick concrete walls and in the loading area the radiation protection walls are 40 cm thick concrete walls. The roof consists of 1.5 mm steel, a 2 cm thick bitumen ground and 5 cm gravel. Inside and outside the PL-2 is dry air. The PL-2 in the x-y-plane is presented in figure 5.28.

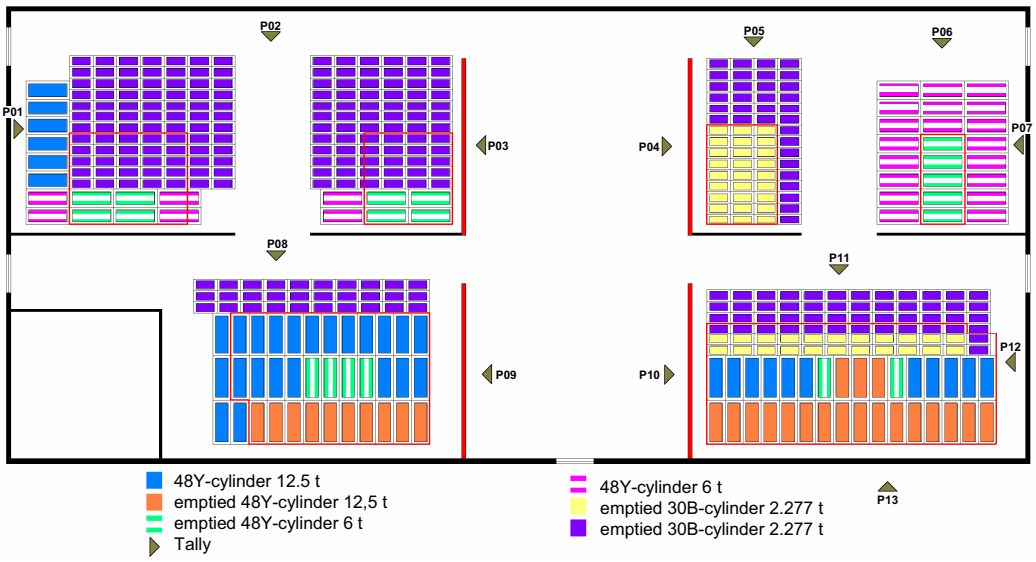

Figure 5.28: Admeasurement of PL-2 and allocation of the individual cylinder types. Black amplified walls are outer walls and simple walls inside the PL-2 and red amplified walls are radiation protection walls for the loading area. The doors are the white block-outs in the outer walls.

The allocation of the cylinder is also presented in figure 5.28. After the operation instructions of the PL-2 and the minimization rule §6 of the Radiation Protection Regulation, emptied cylinders may only be located within the red marked area because a shielding of the concrete walls and the surrounding full cylinders is ensured. In addition, the 30B-cylinder must stay 30 cm apart on the side and 50 cm at the end. 48Y-cylinder may stay 50 cm apart both on the side and at the end. The case is, that the cylinder do not stay too close to each other and still necessary steps can be performed on the cylinders.
The assumed number of cylinders results from the Product UF_6-fluxes, which are produced in the two separation plants (UTA-1 and UTA-2). UTA-2 fills the Product exclusively in 48Y-cyinder with 12.5 t UF_6, however, UTA-1 fills half of the UF_6-flux in 30B-cylinder with 2.277 t and half in 48Y-cylinders with 6 t UF_6. As a time factor, the full Product cylinder have a storage time of 8 months and a storage time of 6 months when they are empty due to the decay time of the daughter nuclides in the empty cylinders. Furthermore, 30B-cylinder for the delivery are stored 4.8 months. Due to the storage times and UF_6-fluxes, the number of cylinder can be determined

exactly and are given in table 5.10. Overall, the maximum allowable total mass of 1250 t UF_6 is stored in PL-2.

Cylinder types	Number UTA-1	Number UTA-2
30B full	65	0
30B emptied	49	0
30B delivery	78	126
48Y 6 t	25	0
48Y 12.5 t	0	39
48Y emptied	78	126

Table 5.10: Assumed number of the different cylinder types which can be calculated by the UF_6-fluxes from UTA-1 and UTA-2 and the storage time in PL-2.

As shown in figure 5.28, both for the 30B- and for the 48Y-cylinder, the simplified geometry (1) is used in MCNP. Here the ambient dose rate is higher from the end of the cylinder and the ambient dose rate from side is nearly equal to the realistic geometry (compare figure 5.12 and 5.14). For radiation protection this has the advantage, that the calculated ambient dose rates are always above the actual values, so that a conservative behavior of the ambient dose rate is available. The radiation components within the cylinder are not changed. These are still the same as in previous investigations of the cylinders.

5.5.2 Nuclide vector and total activity

In PL-2 is Product with an average enrichment degree of about 4.5%. Therefore, the nuclide vector for U-235 is adopted as 4.5% and the other nuclide vectors from the uranium isotopes are adjusted accordingly in MCNP.
For different storage times (some are fresh emptied and other have already a storage time of 6 months) of the individual cylinders, the activities of these are always different due to the ingrowth time of the full cylinders and the decay time of the emptied cylinders, so that the total activity of the individual radiation components must be scaled.
For the radiation component of U-238 plus daughter nuclides in full cylinders, the maximal activity is conservatively assumed. Due to the short half-life of Th-234 (24.1 d), the maximal activity can not be assumed in emptied cylinders because exemplified for the full storage period of 6 months, only a total activity of 0.5% of this radiation component is still present in the cylinder. Therefore, a mean activity of this radiation component for the emptied cylinders will be accepted. This mean

activity $\bar{A}(T)$ devided by the maximal activity A_0 is defined as follows and gives the ratio between the mean activity and the maximal activity:

$$\frac{\bar{A}(T)}{A_0} = \frac{1}{T}\int_0^T e^{-\lambda_{Th-234}\cdot t} = \frac{1}{\lambda_{Th-234}T}\left(1 - e^{-\lambda_{Th-234}\cdot T}\right) \tag{5.4}$$

with T as the maximal storage time of the emptied cylinders and λ_{Th-234} as the disintegration constant of Th-234. The maximal storage time of emptied cylinders is $T = 182.5\ d = 6$ months, so that the ratio of the mean activity and the maximal activity A_0 is $\bar{A}(182.5\ d)/A_0 = 18.9\%$. This mean activity must be also assumed for the bremsstrahlung because the bremsstrahlung is produced by the decay of Pa-234m, which is a daughter nuclide of U-238, and the interaction of the electron with the surrounding material.

For U-235 and Th-231 also the full activity is assumed, since the half-life of Th-231 is much smaller than the half-life of U-235 and therefore a radioactive equilibrium is already available after a few days (see section 4.3).

The precise activity of U-232 and its daughter nuclides can also only be scaled because the daughter nuclides of U-232 are built up by feeding of the cylinder over a period of 8 months and then disintegrate after emptying for 6 months. Since the emptied cylinder are only stored for 6 months, not all of the daughter nuclides decays due to the long half-life of Th-228 in the emptied cylinder and therefore a remaining activity of the daughter nuclides is still left after the second filling of the cylinder. Certainly, there is now the activity of the daughter nuclides from the first filling and the activity of the daughter nuclides which are produced by the ingrowth of the second filling. This increased activity will continue until the cylinder is washed completely after a minimum time of 5 years and no more radioactive material is left in the cylinder. To estimate conservatively the average total activity it can be assumed, that the full cylinders are in radioactive equilibrium for 8 months and have no activity for 6 months. This results, that both in the full and in the emptied cylinders an average activity of 8/14 (57.14%) of the maximum activity is present.

For neutron radiation only the full cylinder are observed and not the emptied cylinder because they do not have any neutron radiation (see section 5.4.5).

Since the activities of the individual radiation components are analyzed, the activities can now be determined concretely with the aid of the number of the individual cylinder types. These are shown in table 5.11.

Radiation components	Activity in γ(n)/s
U-238 + daughters	3370302019342.5
U-235 + daughters	6582933716298.24
U-232 + daughters	102536039017.36
Bremsstrahlung	855186108280.12
Neutrons	(248249153.6)

Table 5.11: Total activity of the individual radiation components in the cylinders of the whole PL-2. The activity in brackets is the activity from neutron-radiation and the others the activity of γ-radiation.

5.5.3 Results of MCNP-calculations for PL-2

After the activity of the individual radiation components is determined and the MCNP-calculations are performed, the ambient dose rate from the result of the Tallies in the MCNP-calculations and the activity can be determined by multiplication of these two factors.

Receiving points	U-238	U-235	Brems	U-232	Neutrons	Total
P01	2.50	0.19	1.62	1.03	9.49	14.83
P02	0.75	0.08	0.54	0.34	3.21	4.91
P03	0.16	0.01	0.11	0.14	0.81	1.23
P04	0.17	0.01	0.11	0.22	0.72	1.23
P05	1.16	0.09	0.79	0.56	3.27	5.87
P06	1.02	0.07	0.69	0.50	2.98	5.26
P07	3.25	0.16	2.23	1.50	8.60	15.75
P08	3.29	0.27	2.18	1.38	8.19	15.30
P09	0.16	0.01	0.12	0.17	0.69	1.14
P10	0.19	0.01	0.13	0.21	0.69	1.23
P11	2.28	0.15	1.51	1.54	5.14	10.62
P12	1.77	0.11	1.15	1.44	4.36	8.83
P13	0.05	0.00	0.01	0.15	0.10	0.31

Table 5.12: Ambient dose rate in $\mu Sv/h$ of the individual radiation contributions at the receiving points inside and outside of PL-2. The relative error of the calculated ambient dose rate of the individual radiation contributions at the receiving points are below 5%.

In PL-2, 13 different receiving points are considered for the ambient dose rate. These can be also found in figure 5.28. The receiving points of interest in radiation protection are P03, P04, P09 and P10 which observe the ambient dose rate within the loading area and P13 for the ambient dose rate outside of PL2. It should be noted, that receiving point P13 is defined on this spot and not elsewhere outside of PL-2 because there are most emptied cylinders which contribute due to the small shielding

effect a high contribution to the ambient dose rate and therefore the highest ambient dose rate is expected at this receiving point outside of PL-2.

From table 5.12, it is clear, that the receiving point P13 outside of PL-2 does not exceed the limit value of 0.5 $\mu Sv/h$ and and so is embraced the licensing requirements and orders. With a mean retention time of 2000 hours per year, a ambient dose of 0.6 mSv is achieved in addition to the natural dose. This shows that the shielding of the outside concrete wall of PL-2 minimizes the ambient dose rate significantly.
The receiving points P03, P04, P09 and P10 are maximal 23% over the allowed ambient dose rate of 1 $\mu Sv/h$ and thus the limit values of the licensing requirements and orders are not followed. However, many conservative assumptions are encountered in MCNP, so that the MCNP-calculations lie over the actual value in PL-2. Following conservative assumptions are used:

- Maximal amount of 1250 t UF_6 in PL-2
- Simplified cylinder geometry with ca. 25% higher dose rate at end of cylinder
- High activity for U-232 and daughter nuclides
- Average enrichment of 4.5% of U-235

Since the simulation of the PL-2 with MCNP is very complex and the reality can not simulated par to par due to the complexity, these conservative assumptions help to have an estimate for the ambient dose rate and to provide radiation protection precautions, if the reality nearly resembles this MCNP-simulation.
By recurrent measurements of ambient dose rate with the aid of dose rate devices at these receiving points in intervals of 3 months it is ensure, that these areas are always under constant observation and ensure that the maximal limit will not exceeded. Since the last measurements were generally lower by half than the MCNP-calculations, it shows, that the conservative assumptions in the MCNP-simulation increase the results of the ambient dose rate.

Chapter 6

Conclusion and Outlook

In context of this master thesis, the effective dose rate of UF_6 cylinders by Monte-Carlo simulations at various distances has been studied in respect of radiation protection. In addition to this, the ambient dose rate of a complete cylinder storage facility was calculated at single receiving points.
For the company Urenco Germany GmbH it is particular important to know the effective dose rate from various UF_6 cylinder types with different enrichment and depletion degrees of uranium 235 because the effective dose of an employee who operates with UF_6 cylinders durig his working time can be estimated. This has radiation protection cases, since radiation exposed persons in category A or B may not exceed a certain limit of effective dose in a year.
Monte Carlo N-Particle (short MCNP) is a computer simulation program, that tracks with the aid of randomly generated source particles and the cross sections of the surrounding matter, the history of a source particle from creation to detection or extinction. The more particles are thereby produced, the smaller the statistical error of the simulation is. Therefore, MCNP can simulate many applications in the array of radiation protection and thus the effective dose rate of UF_6 cylinders. However, to calculate the effective dose rate of UF_6 cylinders correctly, one need to know the geometry of the UF_6 cylinder and the exact radioactiv radiation of them. For the radioactive sources in the MCNP-calculations, the main types of radiation which are produced in a UF_6 cylinder were used. This includes the γ-photons from the decays of the radioactive series of U-238, U-235 and U232, bremsstrahlung which is produced by Pa-234m and the surrounding matter and the neutron radiation which is produced by spontaneous fission of U-238 and the $^{19}F(\alpha,n)^{22}Na$ reaction. After these and other necessary information has been entered into a MCNP-Input file, MCNP calculated the dose per source particle and by multiplying the source activity, the dose rate is

achieved.
To show, that MCNP really calculated the dose rate of UF_6 cylinders at various distances correctly, dose rate measurements were performed at a 48Y-Feed UF_6 cylinder which has already a storage time and thus an ingrowth time of approximately 12 months. Therefore, both from the side and at the end of the cylinder the γ-dose rate and neutron dose rate were measured and were compared with the theoretical MCNP-calculations. It has been shown, that the neutron-ambient dose rate after deduction of background radiation is consistent with the measured neutron-ambient dose rate and MCNP provides, by considering the realistic cylinder geometry and the error limits, very good results. For γ-ambient dose rate, the measured γ-ambient dose rates are in average 20% higher than the calculated γ-ambient dose rates. Since the γ-ambient dose rate device has an oparational error limit of $\pm$24%, the calculated γ-ambient dose rates are within the error limits and can therefore be viewed as correct. To view a wider and more precise verification, an energy-dependent device can be used where the γ-ambient dose rate can be calculated by the energy and intensity of the γ-photons. Furthermore, the "thermal cycling"-effect can play a role, that can increase the γ-ambient dose rate. To confirm this effect a Product-cylinder, which is not exposed the weather conditions can be examined with the devices used in this work. If the measured γ-ambient dose rate still have in average 20% higher values than the values of the calculated γ-ambient dose rate, the "thermal cycling"-effect will be refuted and a measurement error or calibration factor for the increased γ-ambient dose rate can be assumed. Additionally, a fresh delivered Feed cylinder can be examined in regular intervals over a long period of about one year. If the γ-dose rate rise continuously in this observation year, the "thermal cycling" effect will be verified. With the aid of ultrasonic devices simultaneously the density distribution of the UF_6 inside the cylinder can be recorded, which also may disprove or confirm the "thermal cycling"-effect.
In the next step, the MCNP calculations of the effective dose rate of various cylinder types with different enrichment and depletion degrees were presented and examined. It clearly showed, that the effective dose rate, as expected, decrease with increasing distance. Furthermore, the effective dose rate at the side of the cylinder is higher than at the end. This is the case because as seen from the side of the cylinder more radioactive sources are directed to the detector as at the end and thus a higher activity is registered. Since the activity has a relevant influence on the effective dose rate, the effective dose rate at the side of the cylinder is higher than at the end. If the effective dose rate is plotted double logarithmic against the distance, the effective dose rate will go into a linear shape by increasing distance to the cylinder. This indicates,

that the cylinder is perceived as a point source at a certain distance. Due to the different degrees of enrichment and depletion in the various cylinder types, the highest effective dose rate were detected at a 48Y-Product cylinder. By the enrichment of the U-235, the activity of the neutron radiation increases and thus the effective dose rate. 48Y-Tails and Feed cylinders have approximately the same effective dose rate due to the same composition of uranium nuclides. In a 30B-Product cylinder with 5% enrichment, the effective dose rate near the cylinder is in spite of the reduced mass of UF_6 higher than at a 48Y-Feed or Tails cylinder. Due to the small geometry of the 30B-cylinder relative to the 48Y-series, the effective dose rate decreases with increasing distance and fell even below the effective dose rate of the 48Y-Feed and Tails cylinders. In addition, a earlier behaivour of a point source through the small cylinder geometry was observed.

In respect of radiation protection and radiation safety, the effective dose for an employee can now be calculated for each working step, since for every working step the exact distance and retention time of the employee to the vessel is known.

Finally, a complete Product cylinder-storage (PL-2) was simulated with MCNP and the dose rate at specific receiving points was determined. Since only a ambient dose rate of 0.5 $\mu Sv/h$ outside of PL-2 is allowed, the supposedly worst receiving point has been determined. Furthermore, the ambient dose rate within the loading area should not exceed a limit of 1 $\mu Sv/h$ for licensing requirements and orders. After the determination of boundary conditions and conservative assumptions the calculated ambient dose rate outside of PL-2 was 0.31 $\mu Sv/h$, so that here the licensing requirements and orders are adhered. Within the loading area, the ambient dose rate was up to 23% higher than the limits. Since the MCNP-simulation of such a complex building with a large number of cylinders is difficult to simulate par for par, the conservative assumptions weigh very heavily, so that the calculated values lie above the actual value.

Chapter 7

Zusammenfassung und Ausblick

Im Rahmen dieser Masterarbeit wurde die effektive Dosisleistung von UF_6 Behältern mittels Monte-Carlo Simulationen in Hinsicht auf den Strahlenschutz in verschiedenen Abständen untersucht. Außerdem wurde die Ortsdosisleistung eines kompletten Behälterlagers an einzelnen Aufpunkten berechnet.
Für die Firma URENCO Deutschland GmbH ist es von besonderer Bedeutung die effektive Dosisleistung von verschiedenen UF_6-Behältern mit unterschiedlichen An- und Abreicherungsgraden von Uran 235 zu kennen, da so die effektive Dosis eines Mitarbeiters abgeschätzt werden kann, der während seiner Arbeitszeit mit UF_6-Behältern arbeitet. Dies hat strahlenschutztechnische Gründe, da strahlenexponierte Personen der Kategorie A bzw. B einen gewissen Grenzwert der effektiven Dosis im Jahr nicht überschreiten dürfen.
Monte Carlo N-Particle (kurz: MCNP) ist ein Computersimulationsprogramm, das mit Hilfe von zufällig generierten Quellteilchen und den Wirkungsquerschnitten der umliegenden Materie, die Geschichte eines Quellteilchens von der Entstehung bis zur Detektion oder Auslöschung verfolgt. Je mehr Teilchen dabei erzeugt werden, desto kleiner wird der statistische Fehler der Simulation. Hiermit können also viele verschiedene Anwendungen im Bereich des Strahlenschutzes simuliert werden und somit auch die effektive Dosisleistung von UF_6 Behältern. Um jedoch die effektive Dosisleistung eines UF_6 Behälters richtig berechnen zu können, muss die Geometrie des UF_6 Behälters und die genaue radioaktive Strahlung aus diesen bekannt sein. Für die radioaktive Quelle in den MCNP-Berechnungen wurden die Hauptstrahlungsarten der aus den in UF_6 Behältern stattfindenen physikalischen Prozesse verwendet. Dazu gehören die γ-Photonen die bei den Zerfällen der Zerfallsreihen von U-238, U-235 und U232 entstehen, Bremsstrahlung die durch Pa-234m und der umliegenden Materie erzeugt wird und die Neutronenstrahlung, die durch spontaner Spaltung von

U-238 und der $^{19}F(\alpha,n)^{22}Na$-Reaktion induziert wird. Nachdem diese und weitere nötigen Informationen in einer MCNP-Input-Datei eingetragen worden sind, errechnet MCNP eine Dosis pro Quellteilchen und durch Multiplikation der Quellaktivität kann die Dosisleistung errechnet werden.
Um zu zeigen, dass MCNP wirklich dafür geeignet ist die Dosisleistung von UF_6 Behältern in verschiedenen Abständen korrekt zu berechnen, wurden Ortsdosisleistungsmessungen an einem 48Y-Feed UF_6 Behälter durchgeführt der bereits eine Lagerzeit und somit eine Aufbauzeit von ca. 12 Monaten besaß. Dabei wurde sowohl von der Seite des Behälters als auch am Ende des Behälters die γ-Ortsdosisleistung und die Neutronen-Ortsdosisleistung gemessen und mit den theoretischen MCNP-Berechnungen verglichen. Es hat sich herausgestellt, dass die Neutonen-Ortsdosisleistung nach Abzug der Hintergrundstrahlung identisch mit der gemessenen Neutronen-Ortsdosisleistung ist und MCNP hierfür unter Berücksichtigung der Fehlergrenzen und der Verwendung der realitischsten Behältergeometrie korrekte Ergebnisse liefert. Bei der γ-Ortsdosisleistung lagen die gemessenen γ-Ortsdosisleistungen im Durchschnitt 20% höher, als die berechneten γ-Ortsdosisleistungen. Da das γ-Dosisleistungsmessgerät eine Verkehrsfehlergrenze von $\pm 24\%$ besitzt, liegen die berechneten Ortsdosisleistungen innerhalb der Fehlergrenzen und können somit also richtig angesehen werden. Für den Ausblick einer weiteren und noch exakteren Verifizierung kann ein energieabhängiges Messgerät verwendet werden, aus der anhand von Energie und Intensität der γ-Photonen die Ortsdosisleistung berechnet werden kann. Des Weiteren kann der "Thermal Cycling"-Effekt eine Rolle spielen, der die γ-Ortsdosisleistung ansteigen lassen kann. Um diesen noch nicht untersuchten Effekt zu bestätigen kann ein Product-Behälter, der keiner Witterung ausgesetzt ist, mit den in dieser Arbeit verwendeten Messgeräten untersucht werden. Sollte hierbei die gemessene γ-Ortsdosisleistung ebenfalls im Schnitt 20% höher sein, als die berechnete γ-Ortsdosisleistung, so kann der "Thermal Cycling"-Effekt widerlegt werden und ein Messfehler bzw. Kalibrierungsfaktor für die erhöhte gemessene γ-Ortsdosisleistung die Ursache sein. Zusätzlich könnte ein frisch angelieferter Feed Behälter über einen längeren Zeitraum von ungefähr einem Jahr in regelmäßigen Abständen untersucht werden. Sollte dabei die γ-Ortsdosisleistung kontinuierlich ansteigen, so kann der "Thermal Cycling"-Effekt nachgewiesen werden. Mit Hilfe von Ultraschallgeräten könnten zeitgleich Aufnahmen von der Dichteverteilung des UF_6 im Behälter aufgenommen werden, die ebenfalls den "Thermal Cycling"-Effekt widerlegen oder bestätigen können.
Im nächsten Schritt wurden die MCNP-Berechnungen der effektiven Dosisleistung von verschiedenen Behältern mit unterschiedlichen An- und Abreicherungsgraden vorgestellt und untersucht. Es zeigte deutlich, dass die effektive Dosisleistung wie

erwartet mit zunehmenden Abstand geringer wird. Des Weiteren ist die effektive Dosisleistung an der Seite des Behälters höher als am Ende. Dies liegt daran, dass aus Sicht von der Seite des Behälters mehr radioaktive Quellen zum Detektor gerichtet sind, als am Ende und somit eine höhere Aktivität registriert wird. Da die Aktivität einen relevanten Einfluss auf die effektive Dosisleistung hat, ist die effektive Dosisleistung an der Seite des Behälters höher als am Ende. Wird die effektive Dosisleistung doppellogarithmisch gegen den Abstand aufgetragen, so nimmt die effektive Dosisleistung bei weiten Enfernungen zum Behälter einen linearen Verlauf an. Dies deutet darauf hin, dass der Behälter ab einem gewissen Abstand als Punktquelle wahrgenommen wird. Durch die unterschiedlichen An- und Abreicherungsgrade in den einzelnen Behältertypen konnte die höchste effektive Dosisleistung bei 48Y-Product Behältern festgestellt werden. Durch die Anreicherung des U-235 steigt die Aktivität der Neutronenstrahlung und somit die effektive Dosisleistung. 48Y-Tails und Feed Behälter besitzen näherungsweise die Selbe effektive Dosisleistung. Bei einem 30B-Product Behälter war die effektive Dosisleistung in der nähe des Behälters trotz der geringeren Masse an UF_6 höher, als bei einem 48Y-Feed oder Tails Behälter. Durch die kleinere Geometrie des 30B-Behälters gegenüber der 48Y-Serie nahm die effektive Dosisleistung mit zunehmenden Abstand ab und sank auch unter die effektive Dosisleistung von den 48Y-Feed und Tails Behältern. Ebenfalls konnte ein erfrühter Eintritt des Verhaltens einer Punktquelle durch die kleiner Behältergeometrie beobachtet werden. In Hinsicht auf Strahlenschutz und Strahlensicherheit kann die effektive Dosis eines Mitarbeiters für jeden Arbeitsschritt berechnet werden, da bei jedem Arbeitsschritt die genaue Entfernung des Mitarbeiters zum Behälter und die Aufenthaltszeit genau bekannt ist.

Letztendlich wurde ein komplettes Product-Behälterlager (PL-2) mit MCNP nachsimuliert und die Ortsdosisleistung an bestimmten Aufpunkten bestimmt. Da außerhalb des PL-2 nur eine Ortsdosisleistung von 0.5 $\mu Sv/h$ vorhanden sein darf, wurde der vermeintlich schlimmste Aufpunkt außerhalb des PL-2 bestimmt. Des weiteren darf die Ortsdosisleistung innerhalb des Verladebereich einen Grenzwert von $1\mu Sv/h$ nach behördlichen Auflagen nicht überschreiten. Nach der Bestimmung von Randbedingungen und konservativen Annahmen, wurde außerhalb des Pl-2 eine Ortsdosisleistung von 0.31 $\mu Sv/h$ berechnet, so dass hier die behördlichen Auflagen eingehalten werden. Innerhalb des Verladebereichs war die Ortsdosisleistung um maximal 23% höher, als der Grenzwert. Da eine MCNP-Simulation eines solch komplexen Gebäudes mit einer großen Anzahl an Behältern nur schwer eins zu eins rekonstruiert werden kann, überwiegen die konservativen Annahmen sehr stark, so dass der berechnete Wert oberhalb des tatsächlichen Istwerts liegt.

List of Figures

List of Tables

Bibliography

[1] *Urananreicherungsanlage Gronau - Kurzbeschreibung des Endausbaus und der voraussichtlichen Auswirkungen auf die Umgebung, Stand: Dezember 2002.*

[2] *Technical informations - Urenco Gronau GmbH, 7. edition, April 2010.*

[3] ANSI N14.1: *American National Standard for Nuclear Materials - Uranium Hexafluoride - Packaging for Transport.* Technical report, 2001.

[4] Hanno Krieger: *Grundlagen der Strahlungsphysik und des Strahlenschutzes.* Vieweg + Teubner, 2009.

[5] Karl Heinrich Lieser: *Einführung in die Kernchemie.* Verlag Chemie, 1980.

[6] Martin Volkmer: *Kernenergie - Basiswissen.* Informationskreis KernEnergie, June 2007.

[7] ICRP Publication 60: *Recommendations of the International Commission on Radiological Protection.* The Annals of ICRP, 21:1–3, 1990.

[8] Leonard Eyges: *Physics of the Mössbauer Effect.* American Journal of Physics, 33:790–802, 1965.

[9] O. Hahn: *Über ein neues radioaktives Zerfallsprodukt im Uran.* Die Naturwissenschaften, 9(5):84, 1921.

[10] William Duane and Franklin L. Hunt: *On X-Ray Wave-Lengths.* Phys. Rev., 6:166–172, 1915.

[11] N. Bohr: *On the Constitution of Atoms and Molecules, Part I.* Philosophical Magazine, 26:1–25, 1913.

[12] N. Bohr: *On the Constitution of Atoms and Molecules, Part II Containing Only a Single Nucleus.* Philosophical Magazine, 26:476–502, 1913.

[13] N. Bohr: *On the Constitution of Atoms and Molecules, Part III Systems containing several nuclei.* Philosophical Magazine, 26:857–875, 1913.

[14] W. W. Nicholas: *Continous spectrum X rays from thin targets.* Bur. Standards J. Research, 2:837, 1929.

[15] R. D. Evans: *The Atomic Nucleus.* First published by McGraw-Hill, Inc., 1955.

[16] Bernard L. Cohen: *Concepts of Nuclear Physics.* McGraw-Hill, 1971.

[17] E.P. Steinberg and L.E. Glendenin. *Phys. Rev.*, 95:432, 1954.

[18] N. Bohr, A Wheeler: *The Mechanism of Nuclear Fission.* Phys. Rev., Bd. 56:426, 1939.

[19] Weizsäcker, C.F.: *Zur Theorie der Kernmassen.* Zeitschrift für Physik, 96:431–458, 1935.

[20] M. G. Mayer and J. H. Jensen: *Elementary Theory of Nuclear Shell Structure.* Wiley, New York, 1955.

[21] V.M. Strutinsky: *Shell Effects in Nuclear Masses and Deformation Energies.* Nucl. Phys. A, 95:420–442, 1967.

[22] N. A. Wlassow: *Neutronen.* N.J. Hoffmann Verlag Kln, 1959.

[23] K. H. Beckurts, K. Wirtz: *NEUTRON PHYSICS.* Springer-Verlag, Berlin, 1958.

[24] Everling et al.: *Relative nuclidic masses.* Nuclear Physics, 18:529–569, 1960.

[25] Charles Hacker: *Radiation Decay*, February 2007. Computer program.

[26] National Nuclear Data Center: *Evaluated Nuclear Structure Data File (ENSDF).* Brookhaven National Laboratory, updating.

[27] B. E. Miles: *Interaction of Electron with Heavy Nuclei - Monte Carlo calculations of Bremsstrahlung in a Thin Layer.* URENCO Nederland B.V., pages 1–11, 1999.

[28] Freek Keijzer: *Neutron yields and surface dose rates for UF_6 Containers.* SAF/96/127, pages 1–31, 1996.

[29] L. van der Zwan and K. W. Geiger: *Energy levels in ^{23}Na from the $^{19}F(\alpha,n)^{22}Na$ reaction.* Nucl. Phys. A, 284:189–198, 1977.

[30] M. Balakrishnan, S. Kailas and M. K. Mehta: *A study of the reaction $^{19}F(\alpha,n)^{22}Na$ in the bombarding energy range 2.6 to 5.1 MeV.* Pramana, 10:329–339, 1978.

[31] R. G. Jaeger (editor): *Engineering compendium on radiation shielding*, volume I: Shielding fundamentals and methods. Springer-Verlag, Berlin, 1968.

[32] E. A. Lorch: *Neutron spectra of $^{241}Am/B$, $^{241}Am/Be$, $^{241}Am/F$, $^{242}Cm/Be$, $^{238}Pu/^{13}C$ and ^{252}Cf isotopic neutron sources.* Int. J. Appl. Rad. Isot., 24:585–591, 1973.

[33] IAEA Technical Reports Series No. 138: *Compendium of neutron spectra and detector responses for radiation protection purposes*, 1990.

[34] X-5 Monte Carlo Team: *MCNP - A General Monte Carlo N-Particle Transport Code, Version 5*, April 24, 2003 (Revised 2/1/2008).

[35] S. C. Frankle, R. C. Reedy and P.G. Young: *ACTI An MCNP Data Library for Prompt Gamma-ray Spectroscopy.* 12th Biennial Radiation Protection and Shielding Topical Meeting, 2002.

[36] R. J. Howerton, D. E. Cullen, R. C. Haight, M. H. MacGregor, S. T. Perkins, and E. F. Plechaty: *The LLL Evaluated Nuclear Data Library (ENDL): Evaluation Techniques, Reaction Index, and Descriptions of Individual Reactions.* Lawrence Livermore National Laboratory, 15:Part A, 1975.

[37] D. E. Cullen, M. H. Chen, J. H. Hubbell, S. T. Perkins, E. F. Plechaty, J. A. Rathkopf, and J. H. Scofield: *Tables and Graphs of Photon Interaction Cross Sections from 10 eV to 100 GeV Derived from the LLNL Evaluated Photon Data Library (EPDL).* Lawrence Livermore National Laboratory report UCRL-50400, 6, 1989.

[38] M. A. Gardner and R. J. Howerton: *ACTL: Evaluated Neutron Activation Cross-Section Library-Evaluation Techniques and Reaction Index.* Lawrence Livermore National Laboratory report UCRL-50400, 18, 1978.

[39] Lawrence Livermore National Laboratory (LLNL): *Evaluated nuclear data libraries*. updating.

[40] Los Alamos National Laboratory: *Evaluations from the Nuclear Physics Group T-16*. updating.

[41] International Comission on Radiological Protection: *Conversion Coefficients for use in Radiological Protection against External Radiation: ICRP 74*, volume 26. Pergamon, 1996.

[42] Y. Yamaguchi: *DEEP code to calculate dose equivalents in human phantom for external photon exposure by Monte Carlo method.* Japan Atomic Energy Research Institute, Tokai-mura, Ibaraki-Ken, Japan, pages 90–235, 1991.

[43] Y. Yamaguchi: *Effective dose for external neutron exposure.* Radioisotopes, 42:35–36, 1993.

[44] Y. Yamaguchi: *Calculation of effective dose for external neutrons.* J. Nucl. Sci. Technology, 31:821–827, 1994.

[45] W.S. Snyder et al.: *Estimates of absorbed fractions for monoenergetic photon sources uniformly distributed in various organs of a heterogeneous phantom, MIRD Pamphlet No. 5.* Society of Nuclear Medicine, 1969.

[46] W.S. Snyder et al.: *Estimates of specific absorbed fractions for photon sources uniformly distributed in various organs of a heterogeneous phantom, MIRD Pamphlet No. 5.* Revised. Society of Nuclear Medicine, 1978.

[47] `http://www.gfd-katalog.com/master/media/Konvertierungen_Web/Zoom/290202_zoom.jpg?MediandoWEB_gfd_ludwig_feuerschutz=5bef16938d785923ab50937a7370b287`.

[48] *Betriebsanleitung DB-033-961017 vom FH 40 G-10L, Dosisleistungsmessgerät nach DIN 6818.*

[49] *Gebrauchsanweisung MB-036-010823 vom Intelligenter Neutronendetektor FHT 751 (Biorem) fr FHT 6020.*

[50] R. Vandenbosch and J. R. Huizenga: *Nuclear Fission.* Academix Press, 1973.

Appendix

Half-life of spontaneous fission

Nuclide	Half life 's.f.'	# of neutrons	Nucleus	Half life 's.f.'	# of neutrons
^{230}Th	$1.5 \cdot 10^{17}$ a		^{249}Cf	$6.5 \cdot 10^{10}$ a	
^{232}Th	10^{22} a		^{250}Cf	$1.7 \cdot 10^{4}$ a	3.53 ± 0.09
^{232}U	$8 \cdot 10^{13}$ a		^{252}Cf	85 a	3.764
^{233}U	$1.2 \cdot 10^{17}$ a		^{254}Cf	60 d	3.88 ± 0.14
^{234}U	$1.6 \cdot 10^{16}$ a		^{253}Es	$6.4 \cdot 10^{5}$ a	
^{235}U	$3.5 \cdot 10^{17}$ a		^{254}Es	$2.5 \cdot 10^{7}$ a	
^{236}U	$2 \cdot 10^{16}$ a		^{255}Es	2440 a	
^{238}U	$9 \cdot 10^{15}$ a	2.00 ± 0.08	^{244}Fm	3.3 ms	
^{237}Np	10^{18} a		^{246}Fm	20 s	
^{236}Pu	$3.5 \cdot 10^{9}$ a	2.22 ± 0.2	^{248}Fm	60 h	
^{238}Pu	$5 \cdot 10^{10}$ a	2.28 ± 0.08	^{250}Fm	10 a	
^{239}Pu	$5.5 \cdot 10^{15}$ a		^{252}Fm	115 a	
^{240}Pu	$1.4 \cdot 10^{11}$ a	2.16 ± 0.02	^{254}Fm	246 d	3.99 ± 0.20
^{242}Pu	$7 \cdot 10^{10}$ a	2.15 ± 0.02	^{255}Fm	$1.2 \cdot 10^{4}$ a	
^{244}Pu	$6.6 \cdot 10^{10}$ a	2.30 ± 0.19	^{256}Fm	2.63 h	3.83 ± 0.18
^{241}Am	$2.3 \cdot 10^{14}$ a		^{257}Fm	120 a	4.02 ± 0.13
^{242m}Am	$9.5 \cdot 10^{11}$ a		^{258}Fm	380 μs	
^{243}Am	$3.3 \cdot 10^{13}$ a		^{257}Md	30 h	
^{240}Cm	$1.9 \cdot 10^{6}$ a		^{252}No	7.5 s	
^{242}Cm	$6.5 \cdot 10^{6}$ a	2.59 ± 0.09	^{254}No	$9 \cdot 10^{4}$ s	
^{244}Cm	$1.3 \cdot 10^{7}$ a	2.76 ± 0.07	^{256}No	1500 s	
^{246}Cm	$1.8 \cdot 10^{7}$ a	3.00 ± 0.20	^{258}No	1.2 ms	
^{248}Cm	$4.2 \cdot 10^{6}$ a	3.15 ± 0.06	^{256}Lr	10^{5} s	
^{250}Cm	$1.4 \cdot 10^{4}$ a	3.31 ± 0.08	^{257}Lr	10^{5} s	
^{249}Bk	$1.7 \cdot 10^{9}$ a	3.64 ± 0.16	^{258}Lr	20 s	
^{246}Cf	$2.0 \cdot 10^{3}$ a	2.85 ± 0.19	^{261}104	650 s	
^{248}Cf	$3.2 \cdot 10^{4}$ a		^{261}105	8 s	

Table A1: Half life of the spontaneous fission of some nuclides. It is clearly seen that the half life decrease by increasing mass number A. In addition, the number of released neutrons is specified (adapted from [50]).

Example of bremsstrahlung photon spectrum calculation

A bremsstrahlung spectrum which is produced by an electron with a kinetic energy $E = 0.6325$ MeV is considered. The energy value of the electron lies at position $n = 7$ after discret classification of the continous electron energy. Accordingly, the bremsstrahlung spectrum of the electron with the energy of 0.6325 MeV owns 7 different bremsstrahlung energies with intensities which are falling linearly. According to equation 4.2, the electron has an intensity of 0.3618. When the single bremsstrahlung intensities are calculated according to equation 4.4, the sum of the single bremsstrahlung intensities is equal to the intensity of the electron which then confirms equation 4.3. Table A2 and figure A1 show the bremsstrahlungs spectrum which is porduced by an electron with a kinetic energy $E = 0.6325$ MeV.

Energy in MeV	Intensity of photons
0.01	0.08840
0.0575	0.08122
0.17525	0.066453
0.2875	0.051686
0.4025	0.036918
0.5175	0.022151
0.6325	0.007384

Table A2: Example of the bremsstrahlung spectrum which is porduced by an electron with the kinetic energy of $E = 0.6325$ MeV.

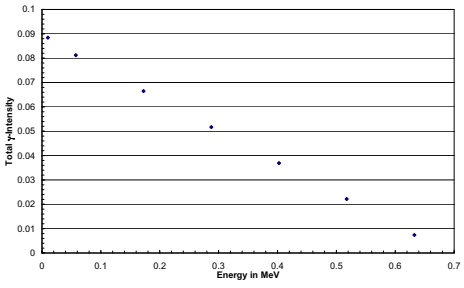

Figure A1: Illustration of the linear relation between the bremsstrahlung intensity and the energy of the bremstrahlung photons which are produced by an electron with a constant energy $E = 0.6325$ MeV.

Activity per gram uranium

Type	Uranium isotope	Activity in $n/s/g_{Uranium}$
Product 6%	U-232	0.004
	U-234	0.383
	U-235	0.007
	U-238	0.013
	U-238 s.f.	0.014
Feed 0.711%	U-232	0.00027
	U-234	0.0325
	U-235	0.00087
	U-238	0.0135
	U-238 s.f.	0.015
Tails 0.43%	U-232	0.000052
	U-234	0.0138
	U-235	0.0005
	U-238	0.0135
	U-238 s.f.	0.015

Table A3: Neutron activity per gram uranium of Product, Feed and Tails. s.f. is the short cut for spontaneous fission and describes the neutrons which are created by spontaneous fission. The activity per gram uranium can be calculated with the neutron yield of the single uranium isotopes, the nuclid vector for every enrichment and depletion degree and the specific activity of each uranium isotope.

Radiation contributions of a 48Y-Feed cylinder

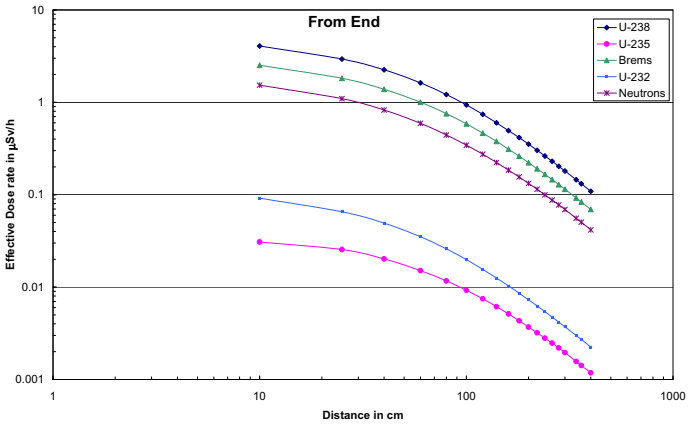

Figure A2: Effective dose rate from end of a Feed cylinder with the single radiation contributions, which are produced by physical processes in an UF_6-cylinder. The points are connected together for a better illustration.

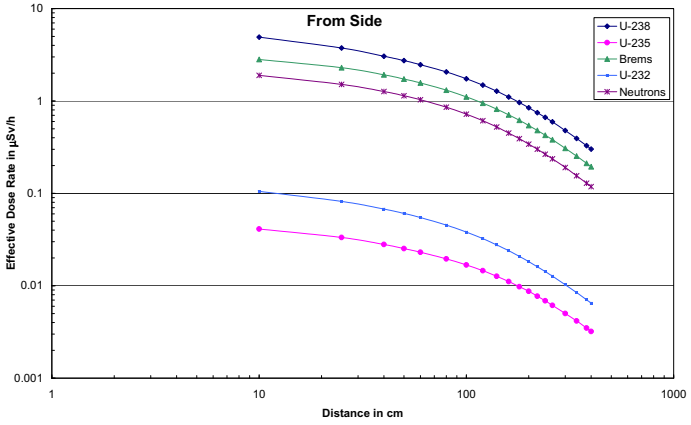

Figure A3: Effective dose rate from side of a Feed cylinder with the single radiation contributions, which are produced by physical processes in an UF_6-cylinder. The points are connected together for a better illustration.

Radiation contributions of a 48Y-Feed cylinder

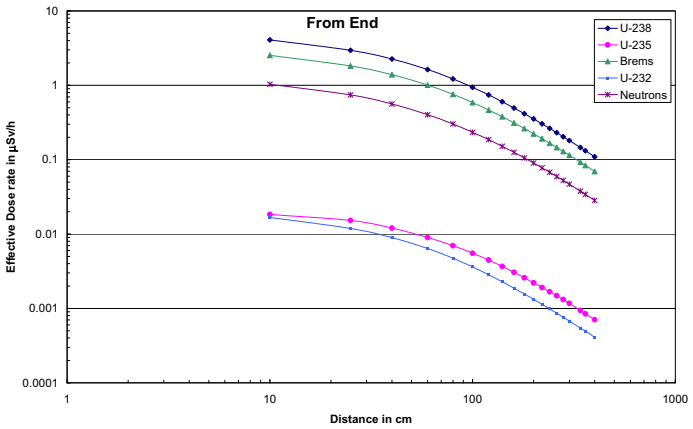

Figure A4: Effective dose rate from end of a Feed cylinder with the single radiation contributions, which are produced by physical processes in an UF_6-cylinder. The points are connected together for a better illustration.

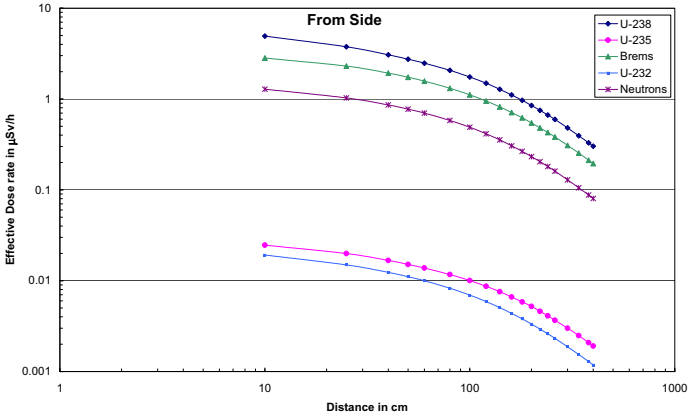

Figure A5: Effective dose rate from side of a Feed cylinder with the single radiation contributions, which are produced by physical processes in an UF_6-cylinder. The points are connected together for a better illustration.

Radiation contributions of a 30B-Product cylinder

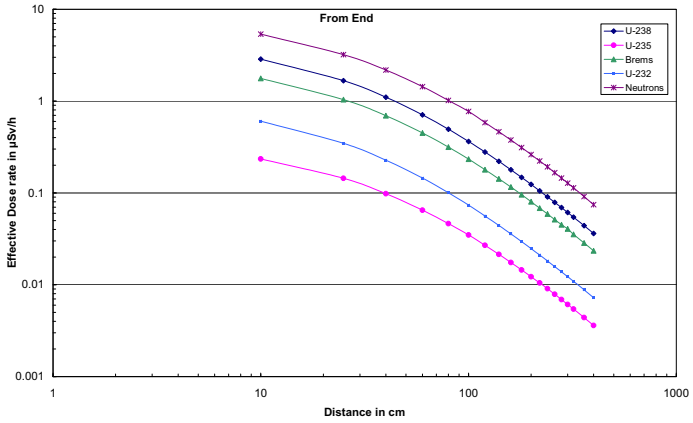

Figure A6: Effective dose rate from end of a 30B-Product cylinder with the single radiation contributions, which are produced by physical processes in an UF_6-cylinder. The points are connected together for a better illustration.

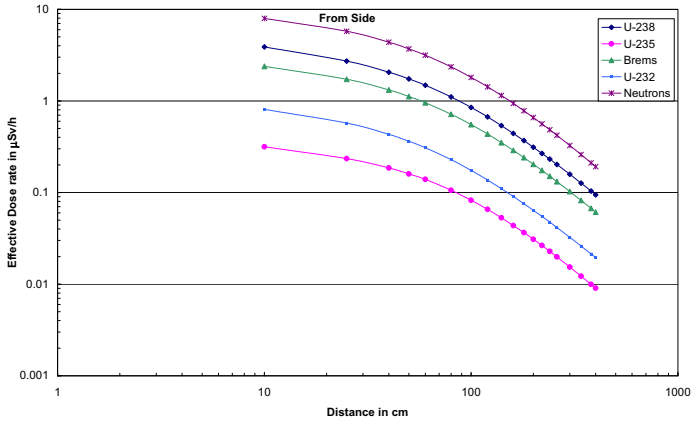

Figure A7: Effective dose rate from side of a 30B-Product cylinder with the single radiation contributions, which are produced by physical processes in an UF_6-cylinder. The points are connected together for a better illustration.

Radiation contributions of a fresh emptied 48Y-Product cylinder

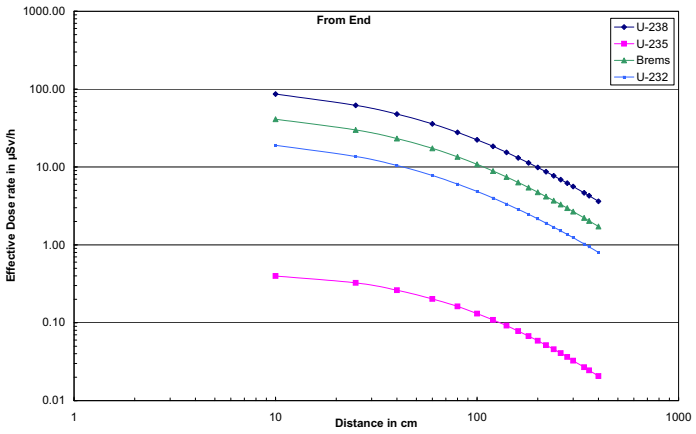

Figure A8: Effective dose rate from end of a fresh emptied 48Y-Product cylinder with the single radiation contributions, which are produced by physical processes in an UF_6-cylinder. The points are connected together for a better illustration.

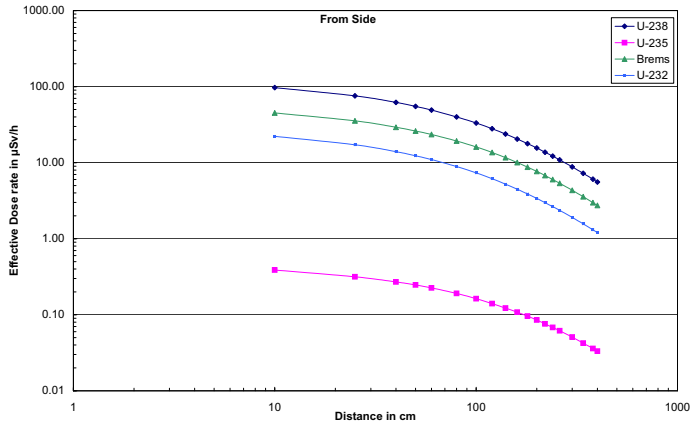

Figure A9: Effective dose rate from side of a fresh emptied 48Y-Product cylinder with the single radiation contributions, which are produced by physical processes in an UF_6-cylinder. The points are connected together for a better illustration.

Dose conversion coefficients $H^*(10)$

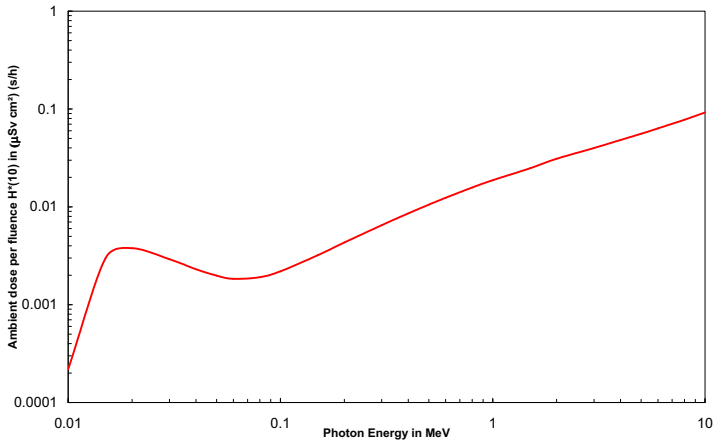

Figure A10: Dose conversion coefficients for ambient dose as a function of energy for photons (adopted from [41]).

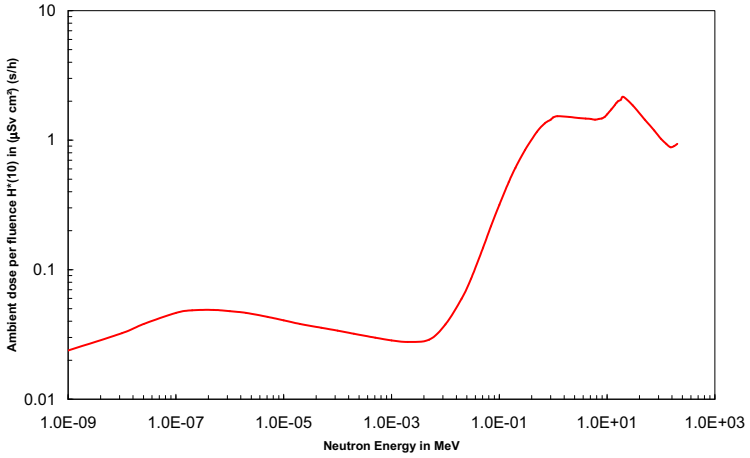

Figure A11: Dose conversion coefficients for ambient dose as a function of energy for neutrons (adopted from [41]).

Acknowledgement

At the end I would like to thank all, who have contributed to the success of this master thesis.

- First I would like to thank Prof. Dr. Alfons Khoukaz, that he kindly admit me in his working group and for the kindly mentoring and that he supported me in every way to write my master thesis at URENCO.
- I would like to thank the company URENCO Deutschland GmbH (UD) and especially Dr. Burkhard Kleibömer, that I could write my master thesis here with the very interesting issue.
- A thank to Prof. Dr. Dieter Frekers for take over the second advisor.
- A special thanks to my office colleague Dr. Michael Räkers for the very good working condition and the support for my many questions to UD and in physical problems.
- Thanks to Timco Visser from UNL, who gave me a good introduction in MCNP and for the many explanation of possible discrepancies.
- Then I would like to thank all my colleagues here at UD and Ann-Katrin Hergemöller, Kay Demmich and Fabian Wilangowski to admit me in your friendship when I came to the University of Münster.
- A very special thanks goes to my parents and my sisters, who supported me in every way of my years of study.
- Thanks to all my friends and my soccer team. You were always a good alternative to all the learning.
- Finally, I would especially like to thank my girl friend Julia Elbers, I got to know while writing this master thesis and she is the most wonderful woman I have ever met before. She gives me so much strength and support and had always been a understanding when I had to work longer. Thank you :-*